ALMA MATER STUDIORUM
–
UNIVERSITÀ DI BOLOGNA

Facoltà di Scienze Matematiche, Fisiche e Naturali

Dottorato di Ricerca in:

GEOFISICA

CICLO: XXII

Settore scientifico-disciplinare di afferenza: **GEO-10**

NUMERICAL AND ANALOGUE MODELS OF FLUID-FILLED FRACTURES PROPAGATION IN LAYERED MEDIA: APPLICATION TO DIKES AND HYDROFRACTURES

Tesi di dottorato di:
FRANCESCO MACCAFERRI

Relatore:
PROF. MAURIZIO BONAFEDE

Coordinatore:
PROF. MICHELE DRAGONI

Esame finale anno 2010

Contents

List of Figures

List of Tables

Acknowledgements

This work has been realised in collaboration with Maurizio Bonafede and Eleonora Rivalta.
What I've done would not have been possible without the continuous and precious scientific support of Maurizio Bonafede. I'm particularly grateful also to Eleonora Rivalta for the special enthusiasm she is able to give me in handling scientific problems.

Many thanks for helpful discussions and for the support are due to Maria Elina Belardinelli and Claudio Ferrari.

For a lot of constructive scientific discussions and at least as many refreshing dinner I am indebted to Luigi Passarelli.

I thank Phill Guise, Carlos Grattoni and Massimo Bacchetti for helping during the experiments. Thanks also to Michael S. Ramsey for providing the photo shown in Figure 5.1 and its geological setting.

Summary

During my Ph.D I developed, in collaboration with Maurizio Bonafede and Eleonora Rivalta, a mathematical model describing fluid-filled crack propagation in presence of elastic, density and fracture toughness discontinuity of the embedding medium. Fluid-filled cracks are modelled in plane strain configuration employing the boundary element method. Analytical solutions for the dislocation elements are employed, the solutions are built starting from the works of Bonafede & Rivalta (1999) and Rivalta et al. (2002) and are generalised for arbitrary tilted elementary closed dislocations.

The pressure gradient along the crack is assumed proportional to the difference between the densities of the host rock and the fluid. Mass conservation is imposed during propagation and fluid compressibility is taken into account. The path followed by the crack is found by maximising the total energy release, given by the sum of the elastic and gravitational contributions. An energy threshold for propagation, depending from the fracture toughness of the host rock, is considered. Gravitational energy plays a major role during propagation also in absence of density layering; in particular, in proximity of layer boundaries, this role is enhanced by the shift of the centre of mass due to shape changes.

The mathematical simulations, in presence of elastic discontinuities, provide a sort of “refraction phenomenon”, that is a sudden change in the direction of propagation when the crack crosses the boundary separating different rigidities: if the dike enters a softer medium, its path deviates toward the vertical, if the dike enters a harder medium its pats deviates away from the vertical and may even become arrested as a horizontal sill along the interface, if the rigidity contrast is large.

Density layering do not influence the direction of propagation of the dike. A density discontinuity of the host rock causes length and thickness variations and can

provides the arrest of the dike if the density of the host rock do not yields enough buoyancy to overcame the energy threshold for propagation (low density layer).
Fracture toughness discontinuities are considered in order to reproduce the condition of weakly welded layers. In this cases the energetic preferred path, when the dike encounters the interface, is the boundary between the layers. For these simulation is shown, in different rigidity and density layering configurations, the required fracture toughness drop on the interface, in order to obtain propagation along the interface.
For validating the mathematical findings laboratory experiments were performed injecting tilted air-filled cracks at the bottom of a transparent cylinder containing two elastic gelatin layers with different rigidities. Cracks are observed to deviate when they cross the rigidity transition surface. The experimental observations are compared with the numerical results. Analysis of the experimental data confirm qualitatively and quantitatively the main characteristics of the mathematical simulations. The laboratory work took place at the 'School of Earth and Environment', University of Leeds (UK), during a period of six months in which I started the collaboration with Eleonora Rivalta.

Chapter 1

Introduction

Recent studies on continental rift zones have evidenced a previously unsuspected role of magmatism in extensional tectonics. Large scale seismic experiments highlighted the presence of reflective high-velocity structures in the deep crust, interpreted as a series of stacked sill-shaped intrusives Thybo & Nielsen (2009); White et al. (2008). No melt seems to have accumulated in the uppermost mantle (40-60 km depth) as no area of low seismic velocity has been found there. Sills must have been generated by a series of dikes ascending and interacting with the tectonic stress, rheological transitions and previous intrusions. It is not yet ascertained what mechanism leads to the formation of stacked sills, what role is played by the Moho, and how the ascent trajectory of dikes is modified by abrupt changes in the (visco)elastic properties of rock caused by either previously emplaced sills or the Moho.

Early analytical investigations on the geometry of propagating dikes include Weertman (1971, 1973), Pollard & Johnson (1973), Secor & Pollard (1975), Pollard (1976). These works develop a simple but powerful framework based on buoyancy and rock resistance. A linear pressure gradient on the crack plane and significant fracture toughness result in an inverse tear-drop shape. More complicated shapes describe different confining stress or driving pressures. Applications include hydrofractures, water crevasses in glaciers, magma dikes.

Local and regional stresses undoubtedly control the direction of dike propagation. Detailed statistical analysis of dike orientation can be employed in order

to infer the local stress and paleostress history (see e.g. Marinoni & Gudmundsson, 2000), assuming that dikes orient themselves along the direction of maximum compressive stress and open up in the direction of minimum compressive stress. However, other factors may influence the energetics involved in the opening and propagation of dikes. The strain energy released during dike emplacement is proportional to the elastic parameters of the hosting medium. In this way, heterogeneities or other sources of anisotropy may cause a change in the energetically preferred opening direction and path.

Other authors, assuming vertical propagation, concentrate on solving the full system of equations describing the motion of viscous buoyant fluid within the crack and the elastic resistance of the hosting medium (e.g. Lister, 1990; Lister & Kerr, 1991; Spence et al., 1987). Meriaux & Jaupart (1998) find time-dependent numerical solution of the coupled problem for a buoyancy-driven magma-filled crack, growing and propagating in an elastic plate on top of a reservoir at constant pressure. Dahm (2000a) solves numerically the interaction problem of viscous flow within the crack, elastic response of the hosting rock and fracturing. He predicts a high pressure gradient at the tail of the fracture where a singularity would be present unless small quantity of fluid is left behind. Roper & Lister (2007) extend the results of Lister (1990) to model the case when the fracture toughness of the hosting rock is large. The shape of the head region of the dike varies significantly with the stress intensity factor and becomes very similar to the typical tear-drop “Weertman” shape. Viscous effects control the propagation rate. Viscous stress drop is significant only at the crack tip and within the tail region, while it is negligible in the head, where the pressure gradient is nearly hydrostatic. The fracture has a complicated shape (see Roper & Lister, 2007, Fig. 10), with a nose - head region followed by a neck-tail-knee structure very similar to the one depicted in Dahm (2000a), Fig. 6a.

Dahm (2000b) develops a boundary-element model for a fluid-filled buoyancy-driven crack, propagating in a homogeneous half-space, studying how stress and density heterogeneities govern the direction of dike propagation. In this model, the crack is filled with a non-viscous batch of fluid with constant mass and, while advancing, it closes at its bottom leaving a broken trail behind. Propagation is driven by the release of elastic strain energy. A similar model was used by Kühn

& Dahm (2004) to study the focusing of dikes ascending from a large melt zone to a narrow mid-oceanic ridge, and by Kühn & Dahm (2008) to investigate how stress affects dike interaction. Applications include sheeted dikes and magma chamber formation at mid-oceanic ridges.

All the mentioned papers model dikes as 2D fluid-filled cracks in a homogeneous medium. Attempts to extend the models to 3D or to layered media are limited to static cracks. Gudmundsson (2005) analyses the influence of local stress and layering on dike propagation in volcanic areas, assuming that dikes propagate in the direction of the maximum compressive stress. Stress heterogeneities due to abrupt changes in the elastic properties of different layers may cause the arrest of dikes at shallow crustal depths while homogeneous stress conditions favour dike propagation to the surface.

Rubin (1995) reviews the many physical processes influencing dike propagation and examines their assumptions critically. He concludes with an outline of major unresolved problems related to dikes. Among others, he highlights the relevance of crack growth, magma buoyancy and the ductile-elastic transition in the host rock.

From an experimental perspective, significant progress has been made in the understanding of dike propagation by using gelatin as a crust analogue and various fluids as magma. Gelatin approximates well an elastic medium: it is brittle at refrigerator temperature and its rigidity can be controlled by varying the concentration of dry gel powder dissolved in water. Among others, Takada (1990) describes observations of the shape and velocity of cracks filled with fluids of different density and viscosity. He finds that crack shape corresponds to the analytical formulation described in Pollard & Mueller (1976); Weertman (1971, 1973). Heimpel & Olson (1994) study dike propagation performing experiments on buoyancy-driven fluids injected into gelatin. They vary the buoyancy, volume and viscosity of the fluid over orders of magnitude and use several different gelatin concentrations. They focus mainly on propagation velocities, identifying two regimes of propagation: a “low velocity” regime, with subcritical stress intensity factor and a “fast velocity” regime with super-critical stress intensity factor. The propagation velocity is found to depend on the fluid buoyancy, the yield strength and fracture toughness of the solid medium, and on the size of the fluid-filled frac-

ture. Ito & Martel (2002) study dike-dike interaction concluding that the stress field induced by a previous dike stuck in a medium would attract following dikes causing magma accumulation. Watanabe et al. (2002) performs a series of analog experiments on crack propagation in presence of an external stress field. In particular they concentrate on the effect of the topographic load and study crack path for different ratio of the shear stress on the crack plane to the average fluid excess pressure. They also perform experiments of interaction between two parallel cracks studying the dependence of path deviation by the ratio of the shear stress generated by one crack to the average excess pressure of the second. They find more deflection for cracks with larger ratio and no deflection for ratios less than 0.2. Rivalta et al. (2005) investigate the role of layering on dike propagation. They observe approximate steady-state regimes when air-filled fractures propagate within one layer, while significant changes in shape and velocity occur while the fractures are crossing the layering interface. Careful analysis of the propagation path shows that even during the so called steady-state regimes, fractures accelerate if they approach a less rigid medium or the free surface and decelerate in the opposite case. Fractures are found to stop at the boundary when they contain a subcritical volume of fluid with respect to the upper medium. They also observe sill formation along the boundary if the rigidity contrast is large. (Rivalta & Dahm, 2006) concentrate on free-surface induced acceleration. Kavanagh et al. (2006) perform analogue experiments injecting water in layered gelatin. They focus on sill formation at the transition surface from a compliant to a stiffer medium. Complete conversion from dike to sill propagation is observed for large driving pressure and high rigidity ratio between layers, while dike arrest is observed in condition of lower driving pressure and low rigidity contrasts. Hybrid dike-sill forms are observed for intermediate values of driving pressures and rigidity ratios.

Different methodological approaches often lead to different conclusions about the dominating factors. This results in a contradictory image of magma propagation, and a coherent theory of dike dynamics is still missing. In-field evidences, theoretical and analogue approaches have rarely been combined to create a more heuristic picture of dike emplacement and propagation.

The aim of this thesis is to study the influence of layering on the propagation

of fluid-filled fractures in general and magma-filled dikes in particular.

The Chap. 2 will be devoted to present the mathematical background on inclined elastic dislocations in layered media. Then a detailed description of the numerical algorithm is given. The dike is modelled as a fluid-filled boundary element crack in plane strain configuration. This approach to the problem of crack propagation was partially inspired by the work of Dahm (2000b). A welded interface between different elastic media is taken into account using analytical solutions from Bonafede & Rivalta (1999) and Rivalta et al. (2002), so that the present model extends to heterogeneous media results obtained by Dahm (2000b) for a homogeneous medium. Moreover, in the present work, the pressure gradient along the crack is assumed to be proportional to the difference between the densities of the host rock and the fluid. A finite batch of magma is considered and the compressibility of the fluid is taken into account in order to conserve the mass of the intrusion during its motion. The mathematical model allows us taking into account an external stress field, density stratification and fracture toughness heterogeneities. The growth, arrest and direction of propagation of the crack is governed by an energetic criterion: the motion of the dike is driven by the minimisation of the total energy, given by the sum of the elastic strain energy and the gravitational potential energy — ignored by Dahm (2000b). Propagation is allowed when the energy release exceeds a fracture energy threshold.
The numerical model provides the path followed by the crack during propagation, as well as its shape and the stress and displacement fields induced in the surrounding medium.

In Chap. 3 the findings for the following relevant cases are illustrated (see also table 1.1):

- CASE 0, CASE 1-1b and CASE 2: homogeneous medium, transition from a rigid to a compliant medium, interaction with the free surface and transition from a compliant to a rigid medium.

- CASE 3, CASE 4 and CASE 5: density layering in a homogeneous elastic medium, in a medium with transition from a rigid to compliant and vice-versa.

- CASE 6, CASE 7 and CASE 8: fracture toughness heterogeneities. The pre-

CASE	μ_1 – μ_2 (GPa)	ρ_1 – ρ_2 (kg/m^3)	E_T^0 – E_T^{tr} (MPa·m)
0	30 – 30	3300 – 3300	0 – 0
1	30 – 1.5 to 24	3300 – 3300	0 – 0
1b	30 – 0	3300 – 3300	0 – /
2	1.5 to 24 – 30	3300 – 3300	0 – 0
3	30 – 30	3000 – 2800 and 2400	1 – 1
4	30 – 12	3000 – 2800 and 2400	1 – 1
5	12 – 30	2800 – 3000	1 – 1
6	30 – 30	3000 – 3000	3.5 – 1
7	30 – 12	3000 – 2800	5.2 – 1
8	12 – 30	2800 – 3000	1.5 – 1

Table 1.1: *Parameters used in the shown cases. The index 1 and 2 refer to the first (lower) and second (upper) layer;* E_T^0 *is the energy threshold for propagation in the medium and* E_T^{tr} *on the interface separating the two layers. The density of the intrusion is 2600 kg/m*^{3} *with a Bulk modulus* $K_f = 10$ *GPa and a volume (per unit length)* $V_0 = 3 \cdot 10^{-3}$ *km*^{2}.

vious configurations are tested reproducing the condition of weakly welded layers.

The last paragraph of Chap. 3 is dedicated to a performance analysis of the elementary dislocation approximation close and across the boundary between different rigidities.

Chap. 4 is dedicated to the analogue experiments performed to validate the findings of the theoretical model. The ascent of tilted air-filled cracks propagating through layered gelatins was observed and the experimental results was quantitatively compared with the results of the numerical model.
The laboratory work presented in this chapter consist in three experiments:

- CASE 0: a tilted air-filled crack propagates through a homogeneous layer of gelatin until it reaches the free surface.
- CASE I: the tilted air-filled crack starts the propagation from the bottom of a rigid layer of gelatin and it enters in a compliant layer.
- CASE II: the tilted air-filled crack starts the propagation in a compliant layer

of gelatin and it reaches and passes the boundary with a more rigid gelatin layer.

The path and shape of air-filled cracks were measured from the records of the experiments. The parameters of the gelatin was measured and the numerical model was set to that values to compare the output with the experimental observations.

In Chap. 5 the developed mathematical model and the analogue experiments are discussed and an overview on the implication of this work for dike propagation in the crust is presented. A paragraph with the future possibly development of the mathematical model conclude this chapter.

Chapter 2

Mathematical model

2.1 Oblique dislocations in a homogeneous medium

Let us consider a dislocation surface Σ, oriented according to the unit normal $\mathbf{n}$ and bounded by a dislocation line $\mathcal{D}$, over which the displacement $\mathbf{u}$ suffers a prescribed jump $\mathbf{b}$ (termed as the Burgers vector): the dislocation condition may be simply written

$$\oint_{\mathcal{L}} du_i = -b_i \tag{2.1}$$

where $\mathcal{L}$ a closed contour encircling the dislocation line $\mathcal{D}$ (Figure 2.1). In a homogeneous isotropic elastic medium, the equations governing the equilibrium configuration of the surrounding medium can be written (e.g. Landau & Lifschitz, 1967):

$$\frac{1}{1-2\nu}\nabla(\nabla\cdot\mathbf{u}) + \nabla^2\mathbf{u} = \hat{\tau}\times\mathbf{b}\,\delta(\vec{\xi}) \tag{2.2}$$

where ν is the Poisson ratio of the elastic medium, $\hat{\tau}$ is the unit vector along $\mathcal{D}$ and $\vec{\xi}$ a 2D vector with origin on $\mathcal{D}$, spanning a surface $S_{\mathcal{L}}$ bounded by the contour line $\mathcal{L}$. It may be noted that the orientation $\mathbf{n}$ of the dislocation surface plays no explicit role in the equilibrium equation (2.2): only the dislocation line appears through its orientation $\hat{\tau}$ and the Burgers vector $\mathbf{b}$.

For a homogeneous unbounded medium, simple analytical solutions exist if the dislocation surface is a half-plane (and the dislocation line is the straight line bounding it). Three independent elementary dislocations may be considered, ac-

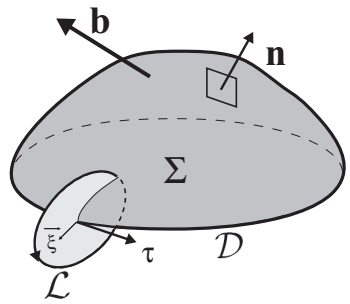

Figure 2.1: *Scheme and notation employed to describe a dislocation surface*

cording to the relative direction of $\mathbf{b}$, $\hat{\tau}$ and $\mathbf{n}$: a screw dislocation has $\mathbf{b}$ parallel to $\hat{\tau}$, an edge dislocation has $\mathbf{b}$ perpendicular to $\hat{\tau}$ and $\mathbf{n}$, a tensile dislocation has $\mathbf{b}$ parallel to $\mathbf{n}$ and perpendicular to $\hat{\tau}$. In the following we shall restrict to consider tensile and edge dislocations.

If $\hat{\tau}$ is along the y axis, a plane strain configuration may be assumed and the displacement field due to a vertically dipping tensile dislocation surface, with $\mathbf{b}$ along x, is

$$\begin{aligned} u_x^{(x)} &= \frac{b^{(x)}}{2\pi}\left[\Phi + \frac{1}{2(1-\nu)}\frac{xz}{r^2}\right] &= b^{(x)} g_x(x,z) \\ u_z^{(x)} &= -\frac{b^{(x)}}{4\pi(1-\nu)}\left[(1-2\nu)\ln r + \frac{z^2}{r^2}\right] &= b^{(x)} g_z(x,z) \end{aligned} \tag{2.3}$$

where the superscript $^{(x)}$ denotes the direction of the Burgers vector, $r = \sqrt{x^2+z^2}$ and $\Phi \in [-\pi, +\pi]$ is the clockwise angle around the y axis shown in Figure 2.2-a:

$$\Phi = \begin{cases} \frac{\pi}{2} + \arctan\frac{z}{x} & \text{if } x > 0 \\ -\frac{\pi}{2} + \arctan\frac{z}{x} & \text{if } x < 0 \end{cases} \tag{2.4}$$

It is easily shown that Φ is continuous and differentiable if $z < 0$, while it jumps from $-\pi$ to $+\pi$ when x changes sign, if $z > 0$.

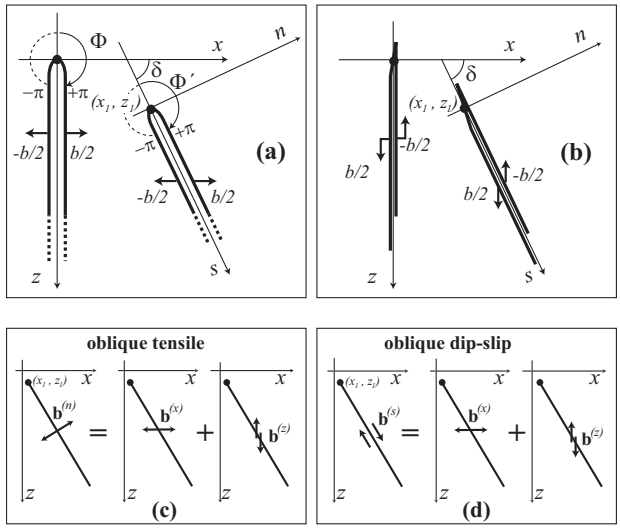

Figure 2.2: *(a) A vertically dipping tensile dislocation has the same solution of an obliquely dipping dislocation with horizontal Burgers vector, if Φ' is employed instead of Φ. (b) A vertical edge (dip-slip) dislocations has the same solution of an oblique dislocation with vertical Burgers vector, if Φ' replaces Φ. Tensile (c) and edge (d) dislocations on obliquely dipping surfaces may be written as linear combinations of type (a) and (b) dislocations.*

The solution for a vertical dip-slip dislocation with $\mathbf{b}$ along z is

$$\begin{aligned} u_x^{(z)} &= \frac{b^{(z)}}{4\pi(1-\nu)}\left[(1-2\nu)\ln r - \frac{z^2}{r^2}\right] &= b^{(z)} h_x(x,z) \\ u_z^{(z)} &= \frac{b^{(z)}}{2\pi}\left[\Phi - \frac{1}{2(1-\nu)}\frac{xz}{r^2}\right] &= b^{(z)} h_z(x,z) \end{aligned} \tag{2.5}$$

where the superscript $^{(z)}$ denotes the direction of the Burgers vector.

Shifting the dislocation line from $x = z = 0$ to $x = x_1, z = z_1$ simply requires a translation of coordinates, which is obtained replacing x and z with $x - x_1$ and $z - z_1$ in the previous formulas. Since the equations (2.1-2.2) do not depend on the orientation of the dislocation surface, if the dislocation half-plane dips at an arbitrary angle $\delta \neq \frac{\pi}{2}$ with respect to the horizontal plane $z = 0$, the

same equations (2.3-2.5) hold, provided that Φ is substituted by the angle Φ' with a jump discontinuity along the dipping half-plane; if the variables n and s are introduced (Figure 2.2a-b)

$$\begin{cases} n = (x - x_1)\sin\delta - (z - z_1)\cos\delta \\ s = (x - x_1)\cos\delta + (z - z_1)\sin\delta \end{cases} \tag{2.6}$$

(n is normal to the dislocation plane and s in the dip direction), we obtain simply:

$$\Phi' = \begin{cases} \frac{\pi}{2} + \arctan\frac{s}{n}, & \text{if } n > 0 \\ -\frac{\pi}{2} + \arctan\frac{s}{n}, & \text{if } n < 0 \end{cases} \tag{2.7}$$

It is to be noted that the strain and stress fields are independent of the dip angle δ, since Φ and Φ' have the same derivatives with respect to x and z.

However, after Φ is replaced by Φ', eq.n (2.3) provides the solution for a Burgers vector along x, which is no longer perpendicular to the dislocation surface. Similarly, eq.n (2.5) still provides the displacement when the Burgers vector is along z, which is no longer parallel to the obliquely dipping dislocation surface. Accordingly, an obliquely dipping tensile dislocation, opening by $\mathbf{b}^{(n)}$ in the direction perpendicular to the dislocation surface, has $b_x^{(n)} = b^{(n)}\sin\delta$, $b_z^{(n)} = -b^{(n)}\cos\delta$ and the solution is

$$\begin{cases} u_x^{(n)} = b^{(n)} g_x \sin\delta - b^{(n)} h_x \cos\delta \\ u_z^{(n)} = b^{(n)} g_z \sin\delta - b^{(n)} h_z \cos\delta \end{cases} \tag{2.8}$$

Similarly, a shear dislocation slipping by $\mathbf{b}^{(s)}$ in the direction parallel to the obliquely dipping dislocation plane, has $b_x^{(s)} = b^{(s)}\cos\delta$ and $b_z^{(s)} = b^{(s)}\sin\delta$; the solution for the displacement due to an inclined dip-slip dislocation is then

$$\begin{cases} u_x^{(s)} = b^{(s)} g_x \cos\delta + b^{(s)} h_x \sin\delta \\ u_z^{(s)} = b^{(s)} g_z \cos\delta + b^{(s)} h_z \sin\delta \end{cases} \tag{2.9}$$

2.2 Oblique dislocations in a layered medium

If the medium is composed by two half-spaces, endowed with different elastic parameters, welded along the plane $z = 0$, equations (2.3-2.5) must be replaced by the solutions for elementary tensile and edge dislocations provided in Bonafede & Rivalta (1999) and Rivalta et al. (2002) for a vertically dipping dislocation surface. These solutions were obtained employing the solutions (2.3-2.5) in each of the two half-spaces and employing an appropriate Love's strain function to remove discontinuities which would appear in traction and displacement over the welded interface $z = 0$. These analytic solutions still contain terms proportional to Φ, needed to fulfil the dislocation condition (2.1), and are written explicitly in the Appendix A. Here we shall indicate them formally as:

$$\begin{cases} u_x^{(x)}(x, z; x_1, z_1; \delta = \frac{\pi}{2}) = b^{(x)} g_x(x, z; x_1, z_1) \\ u_z^{(x)}(x, z; x_1, z_1; \delta = \frac{\pi}{2}) = b^{(x)} g_z(x, z; x_1, z_1) \end{cases} \tag{2.10}$$

for a vertical tensile dislocation, where g_x contains a term $\frac{\Phi}{2\pi}$, and

$$\begin{cases} u_x^{(z)}(x, z; x_1, z_1; \delta = \frac{\pi}{2}) = b^{(z)} h_x(x, z; x_1, z_1) \\ u_z^{(z)}(x, z; x_1, z_1; \delta = \frac{\pi}{2}) = b^{(z)} h_z(x, z; x_1, z_1) \end{cases} \tag{2.11}$$

for a vertical dip-slip dislocation, where h_z includes a term $\frac{\Phi}{2\pi}$.

If a dipping dislocation surface in a layered medium is considered, the same formulas still hold, provided only that Φ is replaced by Φ' in g_x and in h_z; we write them as:

$$\begin{array}{l} u_i^{(x)}(x, z; x_1, z_1; \delta) = b^{(x)} g_i'(x, z; x_1, z_1; \delta) \\ u_i^{(z)}(x, z; x_1, z_1; \delta) = b^{(z)} h_i'(x, z; x_1, z_1; \delta) \end{array} \qquad i = x, z.$$

In the following, it will be convenient to consider Burgers vectors $\mathbf{b}^{(n)}$ perpendicular and $\mathbf{b}^{(s)}$ parallel to the dislocation plane. If the former (normally opening) configuration is considered we have $b_x^{(n)} = b^{(n)} \sin\delta$ and $b_z^{(n)} = -b^{(n)} \cos\delta$, so

that

$$\begin{aligned} u_i^{(n)}(x,z;x_1,z_1;\delta) &= b^{(n)} \cdot [\ g_i'(x,z;x_1,z_1;\delta)\sin\delta - \\ &\qquad h_i'(x,z;x_1,z_1;\delta)\cos\delta\ ], \quad i=x,z. \end{aligned}$$

If the latter (dip-slip) configuration is considered, we have $b_x^{(s)} = b^{(s)}\cos\delta$ and $b_z^{(s)} = b^{(s)}\sin\delta$, so that

$$\begin{aligned} u_i^{(s)}(x,z;x_1,z_1;\delta) &= b^{(s)} \cdot [\ g_i'(x,z;x_1,z_1;\delta)\cos\delta + \\ &\qquad h_i'(x,z;x_1,z_1;\delta)\sin\delta\ ], \quad i=x,z. \end{aligned}$$

Finally, we can write the displacement field for a tilted elementary dislocation with arbitrary Burgers vector $\mathbf{b}$ as the sum of the displacement fields due to it's components $b^{(n)}$ perpendicular and $b^{(s)}$ parallel to the dislocation surface (see Fig. 2.3c,d). We have:

$$\begin{aligned} u_i(x,z;x_1,z_1;\delta) &= b^{(n)} \cdot G_i(x,z;x_1,z_1;\delta) + \\ &\qquad b^{(s)} \cdot H_i(x,z;x_1,z_1;\delta), \quad i=x,z. \end{aligned} \tag{2.12}$$

where:

$$\begin{aligned} G_i &= g_i'(x,z;x_1,z_1;\delta)\sin\delta - h_i'(x,z;x_1,z_1;\delta)\cos\delta \\ H_i &= g_i'(x,z;x_1,z_1;\delta)\cos\delta + h_i'(x,z;x_1,z_1;\delta)\sin\delta \end{aligned}$$

A finite (along dip) dislocation surface between x_1, z_1 and x_2, z_2, with Burgers vector $\mathbf{b}$, is simply obtained subtracting from the solution (2.12) with dislocation line in $x = x_1, z = z_1$ the same solution with dislocation line in x_2, z_2: such a finite dislocation surface will be termed "dislocation element". If c is the half-width of the dislocation element, and x_0, z_0 are the coordinates of its mid point,

$$\begin{aligned} c &= \tfrac{1}{2}\sqrt{(x_2-x_1)^2+(z_2-z_1)^2} \\ x_0 &= \tfrac{1}{2}(x_1+x_2), \quad z_0 = \tfrac{1}{2}(z_1+z_2) \end{aligned},$$

we may write the displacement for a closed dislocation element of length $l = 2c$

as:

$$\begin{aligned} u_i^c(x,z;x_0,z_0;\delta) &= b^{(n)} \cdot \Delta G_i(x,z;x_0,z_0;\delta) + \\ & \quad b^{(s)} \cdot \Delta H_i(x,z;x_0,z_0;\delta)\,, \quad i = x,z. \end{aligned} \tag{2.13}$$

where:

$$\Delta G_i(x,z;x_0,z_0;\delta) = G_i(x,z;x_1,z_1;\delta) - G_i(x,z;x_2,z_2;\delta)$$
$$\Delta H_i(x,z;x_0,z_0;\delta) = H_i(x,z;x_1,z_1;\delta) - H_i(x,z;x_2,z_2;\delta)$$

From the expression (2.13) we can easily calculate the deformation and the stress fields. For the stress tensor we obtain the expression:

$$\begin{aligned} \sigma_{ij}^c(x,z;x_0,z_0;\delta) &= b^{(n)} \cdot \Delta S_{ij}^{(n)}(x,z;x_0,z_0;\delta) \quad + \\ & \quad b^{(s)} \cdot \Delta S_{ij}^{(s)}(x,z;x_0,z_0;\delta) \end{aligned} \tag{2.14}$$

where $\Delta S_{ij}^{(n)}(x,z;x_0,z_0;\delta)$ and $\Delta S_{ij}^{(s)}(x,z;x_0,z_0;\delta)$ are built following the same procedure outlined above for the displacement field: we start from the stress filed generated by a vertically dipping tensile ($\sigma_{ij}^{(x)}$) and dip-slip ($\sigma_{ij}^{(z)}$) semi-infinite elementary dislocations:

$$\begin{aligned} \sigma_{ij}^{(x)}(x,z;x_1,z_1) &= b^{(x)} s_{ij}^{(x)}(x,z;x_1,z_1) \\ & \qquad\qquad\qquad\qquad\qquad\qquad i = x,z. \\ \sigma_{ij}^{(z)}(x,z;x_1,z_1) &= b^{(z)} s_{ij}^{(z)}(x,z;x_1,z_1) \end{aligned} \tag{2.15}$$

where the *loading functions* $s_{ij}^{(x)}(x,z;x_1,z_1)$ and $s_{ij}^{(z)}(x,z;x_1,z_1)$ are respectively equals to $g_{i,j}$ and $h_{i,j}$ (i.e. the derives in x and z directions of the functions g_i and h_i) and are explicitly written in Appendix B.
For an obliquely dipping surface the stress field generated by a tensile ($\sigma_{ij}^{(n)}$) and dip-slip ($\sigma_{ij}^{(s)}$) semi-infinite dislocations are:

$$\begin{aligned}
\sigma_{ij}^{(n)}(x,z;x_1,z_1,\delta) &= b^{(n)}[s_{ij}'^{(x)}(x,z;x_1,z_1)\cos\delta - s_{ij}'^{(z)}(x,z;x_1,z_1)\sin\delta] \\
\sigma_{ij}^{(s)}(x,z;x_1,z_1,\delta) &= b^{(s)}[s_{ij}'^{(x)}(x,z;x_1,z_1)\cos\delta + s_{ij}'^{(z)}(x,z;x_1,z_1)\sin\delta] \\
& \qquad\qquad\qquad\qquad\qquad\qquad\qquad\qquad i = x, z.
\end{aligned}$$

where the loading functions $s_{ij}'^{(x)}(x,z;x_1,z_1)$ and $s_{ij}'^{(z)}(x,z;x_1,z_1)$ are respectively equals to $g'_{i,j}$ and $h'_{i,j}$ (i.e. the derives in x and z directions of the displacement's loading functions g'_i and h'_i). It is easy to notice that $g'_{i,j} = g_{i,j}$ and $h'_{i,j} = h_{i,j}$ so that we can write:

$$\begin{aligned}
\sigma_{ij}^{(n)}(x,z;x_1,z_1,\delta) &= b^{(n)}S_{ij}^{(n)}(x,z;x_1,z_1,\delta) \\
\sigma_{ij}^{(s)}(x,z;x_1,z_1,\delta) &= b^{(s)}S_{ij}^{(s)}(x,z;x_1,z_1,\delta)
\end{aligned} \qquad i = x, z.$$

with

$$S_{ij}^{(n)} = s_{ij}^{(x)}(x,z;x_1,z_1)\cos\delta - s_{ij}^{(z)}(x,z;x_1,z_1)\sin\delta$$

$$S_{ij}^{(s)} = s_{ij}^{(x)}(x,z;x_1,z_1)\cos\delta + s_{ij}^{(z)}(x,z;x_1,z_1)\sin\delta$$

finally, we obtain the solution for the stress field generated by a closed dislocation surface (eq. 2.14) subtracting the solution for a dislocation line x_2, z_2:

$$\begin{aligned}
\Delta S_{ij}^{(n)}(x,z;x_0,z_0;\delta) &= S_{ij}^{(n)}(x,z;x_1,z_1;\delta) - \\
&\quad\; S_{ij}^{(n)}(x,z;x_2,z_2;\delta) \\
\Delta S_{ij}^{(s)}(x,z;x_0,z_0;\delta) &= S_{ij}^{(s)}(x,z;x_1,z_1;\delta) - \\
&= S_{ij}^{(s)}(x,z;x_2,z_2;\delta)
\end{aligned} \tag{2.16}$$

It must be noted that the tensorial function $s_{ij}^{(n)}$ and $s_{ij}^{(s)}$ do not depend on δ because they are obtained through differentiations and linear combinations of the functions g_i' and h_i', where δ appears only in the term Φ', and it was already noted that Φ and Φ' have the same derivatives with respect to x and z. This means that, in terms of stress (and deformation too), the only parameters that characterise an elementary dislocation, are the position of the dislocation line and the Burgers vector.

Finally, tractions acting on the dislocation plane are obtained from equation (2.16) performing a rotation of coordinates by an angle $\theta = \frac{\pi}{2} - \delta$ according to the usual rules of tensor algebra. In order to simplify the notation, we shall write N^n, S^n for the normal and shear components $\Delta S_{nn}^{(n)}, \Delta S_{ns}^{(n)}$ due to a normally opening dislocation element with Burgers vector b^n and N^s, S^s for the normal and shear components $\Delta S_{nn}^{(s)}, \Delta S_{ns}^{(s)}$ due to a dip-slip dislocation element with Burgers vector b^s.

2.3 Crack model

In a "crack model" of a dike, the normal traction σ and the shear traction τ released over the dislocation surface are prescribed instead of the Burgers vector. If a normal traction σ^0 and a shear traction τ^0 were present before dike emplacement and they drop to σ^1 and τ^1 after emplacement, crack opening must provide a normal traction $\sigma^1 - \sigma^0 = -\sigma$ and a shear traction $\tau^1 - \tau^0 = -\tau$. We may easily calculate the Burgers vector needed to generate these tractions at the mid point (x_0, z_0) of a dislocation element (Figure 2.3-a):

$$\begin{cases} b^n\, N^n + b^s\, N^s = -\sigma \\ b^n\, S^n \ + b^s\, S^s \ = -\tau \end{cases} \tag{2.17}$$

where the stresses N^n, N^s and S^n, S^s were introduced at the end of the previous section. This linear 2×2 system allows to calculate the tensile and shear components b^n and b^s of the Burgers vector when the stress drops σ and τ are assigned.

According to the boundary-element technique of solution, a crack may be approximated by a distribution of dislocation elements with different Burgers vectors (to be determined) as sketched in Figure 2.3-b. The normal traction and the shear

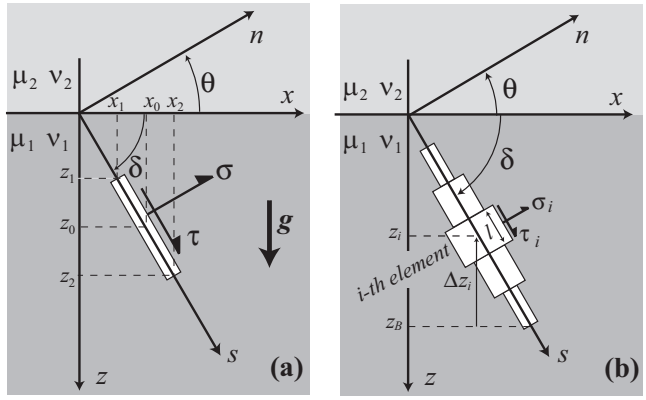

Figure 2.3: *(a) Normal and shear tractions released at the mid-point of a dislocation element; (b) the boundary element approximation of a crack.*

traction at the mid point of each dislocation element are set equal respectively to $-\sigma$ and $-\tau$ and, from these conditions, the Burgers vector is computed for each dislocation element. Of course, the approximation is better if the discretisation is finer and a curved crack surface may be approximated if the dip angle δ_i is allowed to vary.

2.3.1 Boundary element technique: a set of elementary interacting dislocation

In the following mathematical model, a dike is represented as a crack, built according to the boundary element technique. A boundary element crack is made by N interacting dislocation elements (see Fig. 2.3), opening within an elastic layered medium, under assigned stress (or pressure) condition, prescribed at the centre of each dislocation element. The mathematical problem to be solved consists in balancing the stress, produced by all the N dislocation elements at the centre of each dislocation, with the assigned normal and shear stress drop at that

point. So the 2×2 linear system in (2.17) generalises to a $2N \times 2N$ linear system:

$$\begin{cases} \sum_{j=1}^{N} \left[b_j^n \, N_{ij}^n + b_j^s \, N_{ij}^s \right] = -\sigma_i \\ \sum_{j=1}^{N} \left[b_j^n \, S_{ij}^n + b_j^n \, S_{ij}^s \right] = -\tau_i \end{cases} \quad \text{with} \quad i = 1, \cdots, N \tag{2.18}$$

where b_j^n and b_j^s are the normal and dip-slip components of the Burgers vector of the j-th dislocation element, σ_i and τ_i are the normal and shear tractions released, at the mid-point of the i-th dislocation, and N_{ij}^n, S_{ij}^n, N_{ij}^s and S_{ij}^s are the influence coefficients, i.e. the tractions computed at the mid-point of the i-th dislocation $(x = x_i, z = z_i)$, due to the j-th dislocation with mid-point in $(x_0 = x_j, z_0 = z_j)$.

The linear system (2.18) is then solved with the additional constraint $b_j^n \geq 0$, since negative values of b^n would provide interpenetration of matter. In order to fulfil this condition, we devise a simple iterative method that converges well for our purposes.

2.3.2 Fluid filled fractures

In the following we shall consider a finite batch of magma, with assigned mass M_0, ascending through an elastic medium. During magma ascent, new fractures develop above the top of the dike while dike walls come into contact again near the bottom.

In a fluid-filled dike, the normal stress after emplacement is $\sigma^1 = -p_f$ (fluid pressure) while the shear stress vanishes $\tau^1 = 0$, if the dike filling fluid moves slowly enough to neglect viscous friction on crack walls. Accordingly, we put $\sigma = p_f + \sigma^0 = \Delta P$ (ΔP is the "overpressure") and $\tau = \tau^0$ in the r.h.s. of eq.n (2.18).

For the sake of simplicity, we shall not consider any deviatoric component in the initial stress field. More specifically, the initial normal stress σ_i^0 at the centre of the i-th dislocation element, has the lithostatic gradient $-\rho_r g$ (proportional to the density ρ_r of the elastic medium and to the gravity acceleration g) while σ_i^1 has the hydrostatic gradient $-\rho_f g$ (proportional to fluid density ρ_f). We take into account

that fluid density may change according to dike volume in order to achieve mass conservation. A reference configuration is considered in which the overpressure is assigned over the crack length L_0 as

$$\Delta P_0(z_i) = (\rho_m - \rho_0)\, g\, \Delta z_i \tag{2.19}$$

where $\Delta P_0(z_i)$ is the over-pressure at z_i, ρ_r is the density of the embedding medium, ρ_0 is the fluid density and Δz_i is the difference between the depth z_B of the bottom of the crack and the mid-point z_i of the i-th dislocation element (see Figure 2.3).

We assume this as the reference configuration, in which the overpressure vanishes at the bottom tip and the volume of the intrusion and its density assume the reference values V_0 and ρ_0. We shall consider a nearly incompressible fluid, with very high (but finite) bulk modulus K_f, so that ρ_f is practically independent of pressure changes ($\rho_f \sim \rho_0$), while pressure is highly sensitive to volume changes, according to

$$\Delta P_K = -K_f\, \frac{V - V_0}{V_0} \tag{2.20}$$

During propagation, any variation of the crack volume from V_0 to V implies a fluid density variation;

$$\rho_f = \rho_0 + \Delta\rho_f \tag{2.21}$$

where

$$\Delta\rho_f = -\rho_0\, \frac{V - V_0}{V} \simeq -\rho_0\, \frac{V - V_0}{V_0} \tag{2.22}$$

During propagation the overpressure is then

$$\Delta P(z_i) = (\rho_r - \rho_f)\, g\, \Delta z_i + \Delta P_K \tag{2.23}$$

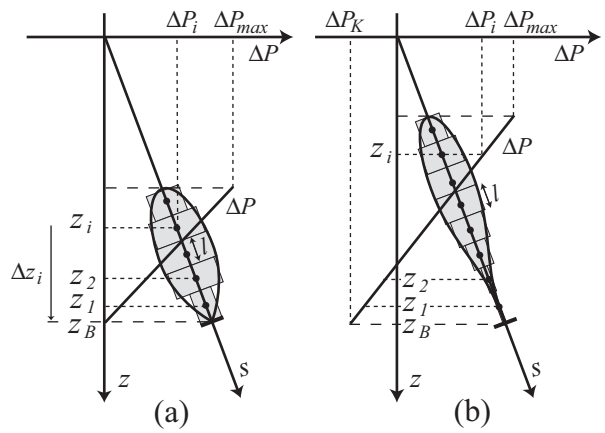

Figure 2.4: *Overpressure in a fluid-filled crack: (a) reference configuration, with overpressure* $\Delta P_0(z_i) = (\rho_r - \rho_0)g\Delta z_i$*; (b) actual configuration with overpressure* $\Delta P(z_i) = (\rho_r - \rho_f)g\Delta z_i + \Delta P_K$*.*

Substituting equations (2.19) and (2.21) in (2.23) we obtain:

$$\Delta P(z_i) = \Delta P_K + \Delta P_0(z_i) - \Delta\rho_f \, g \, \Delta z_i \tag{2.24}$$

For a boundary element crack, we can express the volume V as:

$$V = \sum_{j=1}^{N} l \cdot b_j^n \tag{2.25}$$

where $l = 2c$ is the length of the dislocation elements constituting the crack. Note that all volumes in our $2D$ plane strain model, are meant per unit length along the y axis.

By equation (2.25), we can express equation (2.20) as:

$$\Delta P_K = -\frac{K_f}{V_0}(\sum_{j=1}^{N} l \cdot b_j^n) + K_f \tag{2.26}$$

and similarly, substituting (2.25) in equation (2.22), we obtain:

$$\Delta\rho_f = -\frac{\rho_0}{V_0}(\sum_{j=1}^{N} l \cdot b_j^n) + \rho_0 \tag{2.27}$$

Now, substituting in equation (2.24) ΔP_K from (2.26) and $\Delta\rho_f$ from (2.27), we obtain:

$$\begin{aligned}\Delta P(z_i) = \Delta P_0(z_i) + K_f - \rho_0\, g\, \Delta z_i + \\ -(K_f - \rho_0\, g\, \Delta z_i)\frac{l}{V_0}(\sum_{j=1}^{N} b_j^n)\end{aligned} \tag{2.28}$$

Hence Eq. (2.18) becomes:

$$\begin{cases} \sum_{j=1}^{N} \left[b_j^n\, N_{ij}^n + b_j^s\, N_{ij}^s\right] = \Delta P(z_i) \\ \sum_{j=1}^{N} \left[b_j^n\, S_{ij}^n + b_j^s\, S_{ij}^s\right] = 0 \end{cases} \quad \text{with} \quad i = 1, \cdots, N \tag{2.29}$$

where $N = L_0/l$. Substituting the over-pressure profile (2.28) in the linear system (2.29) we obtain:

$$\begin{cases} \sum_{j=1}^{N} \left[b_j^n \left(N_{ij}^n + \frac{l(K_f - \rho_0 g \Delta z_i)}{V_0}\right) + b_j^s\, N_{ij}^s\right] = \\ \qquad\qquad = \Delta P_0(z_i) + K_f - \rho_0\, g\, \Delta z_i \\ \sum_{j=1}^{N} \left[b_j^n\, S_{ij}^n + b_j^s\, S_{ij}^s\right] = 0 \end{cases} \tag{2.30}$$

$$\text{with} \quad i = 1, 2, \cdots, N$$

The linear system (2.30) can be further simplified noting that, typically

$$K_f \gg \rho_0\, g\, \Delta z_i$$

since, for a km-long magma-filled fracture, we have $K_f \simeq 10^{10}$ Pa, and $\rho_0\, g\, \Delta z_i^{max} \simeq$

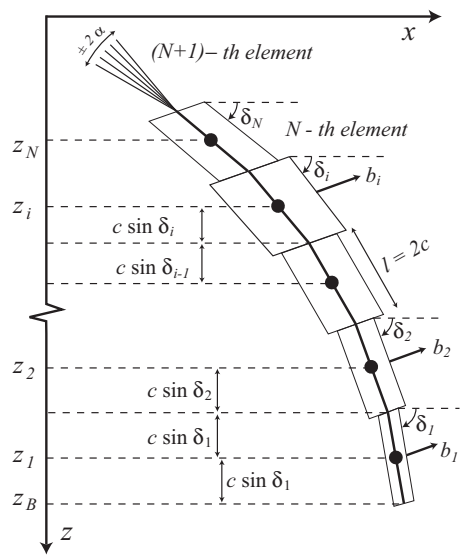

Figure 2.5: *Model parameters employed to describe crack propagation.*

$3 \cdot 10^3 \times 10 \times 10^3 = 3 \cdot 10^7$ Pa. Then, neglecting the term $\rho_0 g \Delta z_i$ in (2.30), we obtain:

$$\begin{cases} \displaystyle\sum_{j=1}^{N} \left[b_j^n \left(N_{ij}^n + \frac{l}{V_0} K_f \right) + b_j^s \, N_{ij}^s \right] = \Delta P_0(z_i) + K_f \\ \displaystyle\sum_{j=1}^{N} \left[b_j^n \, S_{ij}^n + b_j^s \, S_{ij}^s \right] = 0 \end{cases} \qquad \text{with} \quad i = 1, 2, \cdots, N \tag{2.31}$$

The growth and propagation of the dike is modelled iteratively, by adding a dislocation element at the top of the fluid-filled crack and deleting, if this is the case, dislocation elements with $b_i^n \leq 0$ at the bottom. When this happens, the stress intensity factor vanishes at the bottom end: this assumption agrees with the fact that the elastic medium is left fractured after the crack passage and cannot sustain any tensile stress (see Fig. 2.4b).

At each step of our iterative mathematical model, we re-evaluate the pressure profile in order to calculate the new equilibrium configuration of the crack. Fluid-dynamic effects are not considered, since the model describes the propagation

path as a sequence of static equilibrium configurations; this should be a reasonable approximation if the propagation velocity and the fluid viscosity are low.

As far as the crack is far away from the rigidity discontinuity in $z = 0$, the volume increase due to the opening of a new dislocation element at the top, is accompanied by a simultaneous, uniform, pressure drop that induces the closing of the bottom dislocation element. When the crack is close to a rigidity discontinuity, the number of closing dislocations at the bottom, for each new dislocation opening at the top, may vary depending on the rigidity contrast $r = \mu_2/\mu_1$. If the crack migrates toward a higher rigidity layer ($r > 1$), it may happen that no dislocation closes at the bottom since the length of the dike has to increase in order to conserve the mass of the intrusion, due to the minor opening (lower b_i^n) near the high rigidity layer. If the crack moves toward a lower rigidity layer ($r < 1$) the opposite may happen (more than one dislocation may close at the bottom for each new dislocation opening at the top).

2.3.3 An energetic criterion for propagation

We calculate the energy release during propagation as the difference between the strain energy and the gravitational energy in two consecutive configurations. Propagation is allowed if the energy release exceeds a specific fracture energy threshold (i.e. the energy required to fracture the new surface).

The strain energy per unit length along y, corresponding to a fracture with length $L = N \cdot l$ (Aki & Richards, 1980, p. 55-56) is:

$$W(L) = \sum_{i=1}^{N} \frac{l}{2} \left(\sigma_i^n \cdot b_i^n + \sigma_i^s \cdot b_i^s\right) \tag{2.32}$$

At the next iteration, we add a dislocation element of length l at the top of the fracture. The strain energy will be:

$$W(L+l) = \sum_{i=1}^{N+1} \frac{l}{2} \left(\sigma_i^{n\prime} \cdot b_i^{n\prime} + \sigma_i^{s\prime} \cdot b_i^{s\prime}\right) \tag{2.33}$$

where primes indicate terms computed at equilibrium of the new configuration

(with $N+1$ dislocation elements). The specific strain energy release is $\Delta W = [W(L) - W(L+l)]/l$, which is positive if the strain energy decreases. Note that in a homogeneous unbounded medium, in absence of external stress of tectonic origin, a fluid-filled fracture, with the condition of vanishing stress intensity factor at the bottom, propagates maintaining its length and shape. Indeed, in this case, we obtain, from our model:

$$b_1^{n\prime} = 0 \quad \text{and} \quad b_i^{n\prime} = b_{i-1}^n, \quad \sigma_i^{n\prime} = \sigma_{i-1}^n \quad \text{for} \quad i \geq 2$$

Thus, $W(L) = W(L+l)$ and $\Delta W = 0$, so that the crack would not propagate spontaneously if only the strain energy were considered. This shows the need for considering also the gravitational energy release. However, if the hosting medium is layered, with a discontinuity in the elastic parameters, we obtain $\Delta W > 0$ if the propagation is toward the lower rigidity layer and $\Delta W < 0$ if the propagation is towards the higher rigidity.

On the contrary, the release of gravitational energy is always positive if the fluid-filled fracture propagates upward and the density of the intrusion is lower than the density of the hosting medium. In terms of the gravity potential (which is defined up to a constant term), the upward propagation of a low density intrusion within a higher density medium is equivalent to the upward propagation of a negative mass. For a fracture with length $L = N \cdot l$ the gravitational energy, calculated up to an arbitrary constant K, is:

$$G(L) = K + g\,\Delta\rho \sum_{i=1}^{N} (l \cdot b_i^n \cdot \Delta z_i) \tag{2.34}$$

where $\Delta\rho = \rho_f - \rho_r$, g is the gravity acceleration, $l \cdot b_i^n$ is the volume (per unit length) of the ith dislocation element (that hosts fluid instead of the elastic medium) and Δz_i is the difference between the bottom of the crack z_B and the depth z_i of the centre of the ith dislocation element (see Fig. 2.5):

$$\Delta z_i = \frac{l}{2} \sum_{j=1}^{i} (\sin\delta_{j-1} + \sin\delta_j)$$

with δ_j the dip angle of the jth dislocation element and δ_0 conventionally chosen equal to zero, so that $\sin\delta_0 = 0$.
At the next iteration we add a dislocation element of length l at the top of the fracture. The gravity potential is then:

$$G(L+l) = K' + g\,\Delta\rho' \sum_{i=1}^{N+1} \left(l \cdot b_i^{n\prime} \cdot \Delta z_i\right) \tag{2.35}$$

where $\Delta\rho' = \rho_f' - \rho_r$. Again, primes indicate terms computed at the equilibrium of the new configuration.
Note that the constant K' in the (2.35) in not necessary equal to K (in eq. 2.34): in particular $K = K'$ only if the total volume per unit length of the dike V is equal to the new volume V' (with V and V' according to eq. 2.25). In this case we have also $\Delta\rho = \Delta\rho'$. Defining the specific gravitational energy release (positive if the energy decreases) as $\Delta G = [G(L) - G(L+l)]/l$ we simply obtain:

$$\Delta G = g\,\Delta\rho \sum_{i=1}^{N+1} \Delta z_i \left(b_i^n - b_i^{n\prime}\right)$$

In general, if $V' \neq V$, we have to consider two contributions in order to re-write eq. (2.35) up to the same constant of the (2.34): (i) the variation in the density of the intrusion; (ii) the redistribution of mass in the housing rocks due to the volume change in the dike. The first contribution was already introduced by considering the new density $\Delta\rho'$ defined by eq. (2.22). The second contribution should consider variations in the density of the host rocks. Rigorously we should calculate the deformation field generated by the dike in order to compute, as a function of the coordinates (x, z), the deviation (with respect to the previous configuration) in the density of the host rocks. By integration of the "deviated density filed" we should obtain a term $k = g \int z\,[\rho_r(x,z) - {\rho_r}'(x,z)]\,dxdz$ that allows us to write $K' = K + k$.
An approximation that simplify the calculation of k can be introduced by the following consideration. If we do not consider this term k and simply assume $K = K'$, we introduce an error in ΔG corresponding to the loose of a mass δm equal to the volume variation of the dike $\Delta V = V - V'$ with the density of the

rocks ρ_r. A good estimation of k can be obtained considering δm as uniforming re-distributed around the dike. With this approximation we can write:

$$k = g\rho_r \sum_{i=1}^{N+1} \left(l \cdot \overline{\Delta b^n} \cdot \Delta z_i \right)$$

with

$$\overline{\Delta b^n} = \frac{1}{N+1} \sum_{i=1}^{N+1} (b_i^n - b_i^{n\prime})$$

now we can write the eq. (2.35) with $K' = K + k$:

$$G(L+l) = K + \Delta\rho' \, g \sum_{i=1}^{N+1} \left(l \cdot b_i^{n\prime} \cdot \Delta z_i \right) + g\rho_r \sum_{i=1}^{N+1} \left(l \cdot \overline{\Delta b^n} \cdot \Delta z_i \right) \quad (2.36)$$

and we obtain the specific gravitational energy release, $\Delta G = [G(L) - G(L+l)]/l$, using eq. (2.36) and (2.34):

$$\Delta G = g \sum_{i=1}^{N+1} \Delta z_i \left(\Delta\rho \cdot b_i^n - \Delta\rho' \cdot b_i^{n\prime} - \rho_r \overline{\Delta b^n} \right) \quad (2.37)$$

In the previous sections we have never considered density layering in the host rocks. The introduction of density stratification in the mathematical model do not change any theoretical consideration developed since now unless the introduction of a density ρ_r dependent from the depth z. The presence of an interface between layers with different densities introduce a term ΔG_{int} in the calculation of the specific gravitational energy release due to the displacement of the interface. This contribute can be calculated as:

$$\Delta G_{int} = \Delta\rho_{1-2} \cdot g \int_{-\infty}^{+\infty} - \left[u(x, z=0) - u'(x, z=0) \right] dx \quad (2.38)$$

where $\Delta\rho_{1-2}$ is the difference between the density of the lower and upper layer respectively, $u(x, z=0)$ is the displacement at the interface and the prime indicates again terms calculated at the equilibrium of the new configuration. The minus

inside the integral is due to the choice of z axis in downward direction. Equation 2.38 can be easily discretised in order to be computed in our numerical code.
Now we can generalise eq. 2.37 for density layering adding the term ΔG_{int} due to the interface displacement and writing $\Delta\rho$ and ρ_r as functions of z:

$$\Delta G = g \sum_{i=1}^{N+1} \Delta z_i \left[\Delta\rho(z) \cdot b_i^n - \Delta\rho'(z) \cdot b_i^{n\prime} - \rho_r(z)\overline{\Delta b^n} \right] + \frac{\Delta G_{int}}{l} \tag{2.39}$$

The specific total energy release (per unit advancement of the crack tip) is the sum of the two contributions ΔW and ΔG:

$$\Delta E = \Delta W + \Delta G \tag{2.40}$$

As said at the beginning of this section, propagation is allowed if this energy exceeds a specific fracture energy threshold per unit lengthening. This threshold E_T can be estimated as (Dahm, 2000b):

$$E_T = K_c^2 \frac{1-\nu}{2\mu} \tag{2.41}$$

where K_c is the fracture toughness. Elastic-brittle materials follow the relation:

$$K_c = 2 \cdot \sqrt{\gamma_s \mu (1+\nu)} \tag{2.42}$$

(see Griffith, 1920; Menand & Tait, 2002) so that:

$$E_T = 2(1-\nu^2)\gamma_s \tag{2.43}$$

where γ_s is termed “specific surface fracture energy” which depends only on the composition and temperature of the elastic solid.

2.3.4 Direction of propagation

In order to choose the direction of fracture propagation, we open a test dislocation element in different directions and calculate the energy release for each of these configurations (see Fig. 2.5). We choose the direction that maximises the energy

release and allow the propagation in this direction only if the energy release exceeds the fracture energy threshold (as discussed in the previous paragraph). If δ_N is the dip angle of the last dislocation element at the top of the crack, we try 5 different directions of propagation by the opening of a test dislocation with dip angle of:

$$\delta_{N+1} = (\delta_N - 2\alpha);\ (\delta_N - \alpha);\ \delta_N;\ (\delta_N + 2\alpha);\ (\delta_N + 2\alpha)$$

where α is chosen in the range of $[2^\circ, 5^\circ]$, depending on the number N of elements constituting the crack (usually N is in the range of $40 \div 80$ elements), in order to obtain a stable path for the crack propagation.

Chapter 3

Numerical results

In order to isolate the influence of the elastic discontinuity on the path followed by the crack, we show in section 3.1 results obtained without introducing any external (tectonic) stress or density stratification in the hosting rocks and show our mathematical results for a vanishing energy threshold (CASE 0 - 1 and 2). Dikes start to propagate far enough from the transition so that initially they do not suffer the presence of the discontinuity. We set model parameters to typical sub-crustal values (see Table 3.1). In section 3.2 we show results obtained with density and/or rigidity stratification (CASE 3 - 4 and 5). In this cases we set the mathematical model to three significant geological configuration (see Table 3.3). In section 3.3 we introduce in the housing medium a weak surface at the interface separating different rocks (CASE 6 - 7 and 8).

During propagation we conserve $M_0 = V_0 \cdot \rho_0$ that represents a mass-per unit length in our 2D model. The output of the mathematical model provides: (i) crack propagation path; (ii) crack shape, (iii) stress changes and displacements induced in the medium, (iv) energy release per unit lengthening during propagation.

3.1 Rigidity stratification

Before showing the results obtained for the transition from a stiff to a compliant medium (CASE 1) and the inverse configuration (CASE 2), we consider the simplest possible configuration: a tilted dike propagating in a homogeneous un-

$\rho_0 = 2600$ kg/m^3	$V_0 = 3 \cdot 10^{-3}$ km^2	$K_f = 10$ GPa
$\rho_r = 3300$ kg/m^3	$1.5 \leq \mu \leq 30$ GPa	$\nu = 0.25$

Table 3.1: *Parameters used in CASE 0, 1, 2: ρ_0, V_0 and K_f are the reference density, volume (per unit length) and Bulk modulus of the fluid intrusion, ρ_r, μ and ν are the density, rigidity and Poisson ratio of the host rock.*

bounded medium under the effect of gravity (CASE 0).

In all the cases we set the parameters of the mathematical model to the values reported in Table 3.1. The results for CASE 1, 2, and 3 are summarised in Table 3.2.

3.1.1 CASE 0 (Homogeneous Medium)

We show in Fig. 3.1 the output of the model for CASE 0: the path followed by the dike, its shape (Fig. 3.1-a) and the specific energy release (Fig. 3.1-b). In this case we choose a uniform rigidity $\mu = 30$ GPa and an initial length for the dike of 2.70 km with the other parameters set according to Table 3.1. Note that we impose an initial length for the fracture that is found to be less than L_0 (the reference length providing vanishing overpressure at the bottom tip for the assigned volume V_0). This choice implies that the initial volume comes out to be less than the reference volume V_0 and, as a consequence, we have a very high initial positive contribution ΔP_K to the pressure $\Delta P(z_i)$ (see eq. 2.23 and Fig. 2.4-b). Such an internal pressure provides a quasi-elliptical initial shape (see Fig. 3.1-a1), that in general will be far from the characteristic tear-drop shape, since the contribution ΔP_K is very high with respect to the buoyancy terms. In this initial configuration, the stress intensity factors at both tips of the dike are positive, and this should provide crack extension in both directions. We allow crack growth only at the upper tip but this assumption is inessential in a homogeneous infinite medium if the lengthening of the dike is straight (as may be checked “a posteriori”). The term ΔP_K becomes quickly smaller during crack growth, since V increases, so that the contribution of buoyancy terms to the stress drop becomes dominant. In Figure 3.1-a2, the length is 3.96 km and the drop-shape is not fully attained, yet. The final characteristic tear-drop shape has a length of 4.98 km (Figure 3.1-a3 and 3.1-a4)

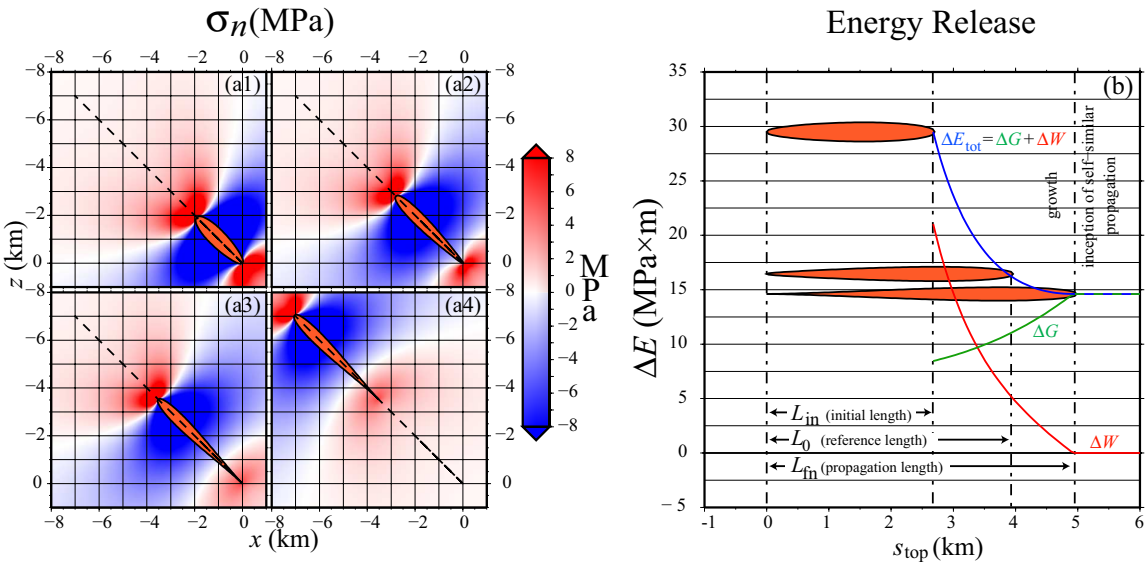

Figure 3.1: *Case 0: growth and propagation of a* $45°$ *tilted fluid-filled fracture in a homogeneous elastic medium. Panels a(1-4): energetically preferred path (dashed line), shape of the dike (opening exaggerated by a factor* 1500*) and tensile stress induced in the medium, normal to the dike plane. Panel b: total specific energy release per unit of propagation and its contributions* ΔW *(elastic deformation energy) and* ΔG *(gravitational energy) plotted as functions of the* s*-coordinate of dike's upper tip. We show the shape of the dike at its initial length (*$L_{in} = 0.8$ *km), at its reference length (*$L_0 = 1.22$ *km) and at its final length (*$L_{fn} = 1.52$ *km).*

and remains constant (in the homogeneous case we are considering) during the subsequent propagation, with positive ΔG and vanishing ΔW (see Figure 3.1-b).

The path followed by the crack is a straight line: this behaviour can be easily and intuitively understood at the beginning of the growth phase. In fact, since the deformation energy release ΔW dominates with respect to the gravitational term ΔG (see Figure 3.1-b), we expect the opening of the new dislocation at the upper tip in the same direction of the crack's dip angle, in order to optimise the mutual interaction between the dislocation elements (or maximise the tensile stress acting on each of them), which drives the opening of the crack.
When the contribution of the gravitational energy ΔG becomes greater and dominates in driving the propagation, it might be expected that the crack should deviate toward the vertical direction, in order to open the new dislocation in a higher point and optimise the gravity potential drop. Instead, even considering only the gravitational energy, the path chosen results to be rectilinear along dip. This can be understood considering that the gravitational energy release is larger if more mass is displaced to shallower depth. Owing to mutual interaction among elementary dislocations, crack opening (and mass shift) is maximum for rectilinear fracture lengthening while a deviation toward the vertical would provide less mass shifted to slightly shallower depth. Actual computation shows that the maximum total energy release, in a homogeneous medium, is obtained in the former case.

3.1.2 CASE 1

In this case the rigidity of the lower elastic half space is $\mu_1 = 30$ GPa while the rigidity of the upper half space is $\mu_2 < \mu_1$. We define as rigidity contrast $r = \mu_2/\mu_1$ and show the results of our simulations varying the rigidity contrast according to the values $r = \{0.8; 0.6; 0.4; 0.2; 0.05\}$.

The typical rigidity contrasts that we can encounter in natural cases can reach a ratio of an order of magnitude in case of contact between layers of basaltic rocks ($\mu \simeq 30$ GPa) and sandstones ($\mu \simeq 3$ GPa). The same order for the rigidity ratio is obtained considering a transition from basalt to tuff or pyroclastic sediments. A rigidity ratio between 0.5-0.3 can be observed at the boundary between granitic crust and sandstones. Lower contrasts are typically inferred at the Moho,

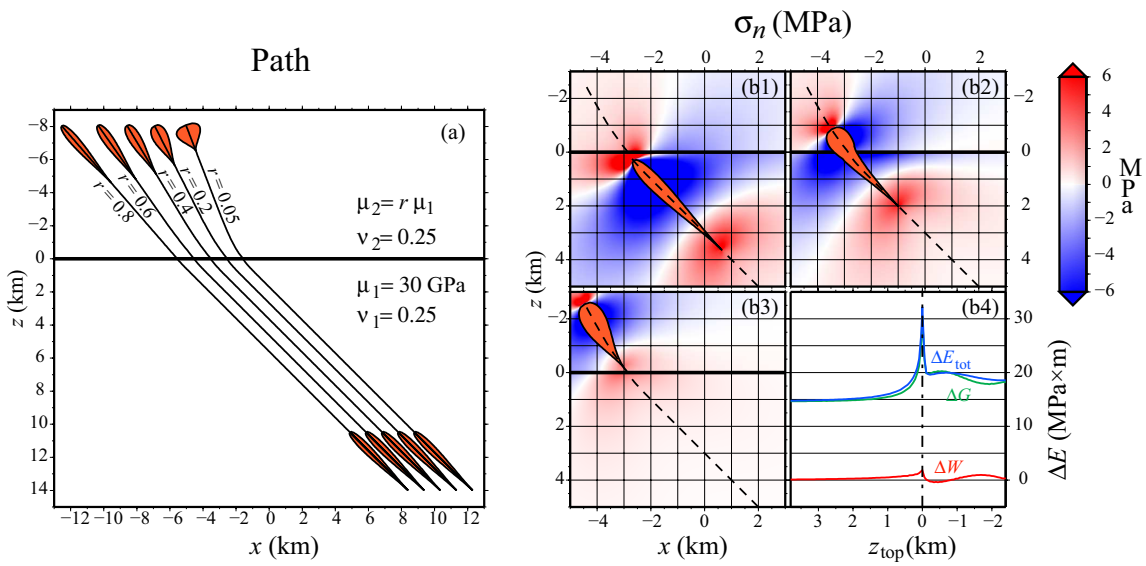

Figure 3.2: *CASE 1: propagation of a* $45°$ *dipping, fluid-filled fracture, in a layered elastic medium. Panel (a): energetically preferred path and initial and final shape of the dike (opening exaggerated by a factor* 500*) for different rigidity contrasts. In all these simulations we used an initial number of dislocation elements* $N = 71$ *and a test angle* $\alpha = 2°$*. Panels (b1) – (b3): energetically preferred path (dashed line), shape of the dike (exaggerated by a factor* 500*) and normal stress induced in the medium for* $r = 0.2$*. Panel (b4): diagram of the specific total energy release, plotted as functions of the* z*-coordinate of the top of the dike.*

in which the purely elastic ratio can reach values $\simeq 0.5$. In the case of the Moho, an important role could be played by the effective rigidity felt by the dike, due to viscoelastic properties of the mantle (Eissa & Kazi, 1988).

The initial crack length is chosen equal to the "equilibrium-length" of propagation, obtained when the stress intensity factor vanishes at the lower tip (as already discussed for CASE 0).

In Figure 3.2-a we show the path of the crack and its initial and final shape for different rigidity contrasts. The most interesting feature consists in a change of the direction of propagation near the boundary separating different rigidities. The energetically favourite path provides a sort of refraction angle due to the influence of the elastic discontinuity. In particular, passing from a stiff to a compliant medium, this model shows a greater deviation toward the vertical direction if r is lower. Note that the dike inflates and shortens considerably after crossing the interface.

In Figure 3.2-b we zoom on a particular configuration ($r = 0.2$). We highlight changes in the shape of the dike approaching and crossing the boundary separating a stiff ($\mu_1 = 30$ GPa) from a compliant medium ($\mu_2 = 6$ GPa). We can observe also the stress change induced in the medium by the dike (Fig. 3.2, panels b1 - b2 - b3): in particular we can notice how the boundary is affected initially by a tensile stress and then by a compressive stress concentrating under the transition boundary. We plotted the normal stress in the dike reference frame n, s (when the dislocation surface is not straight we consider the average dip as the direction of the s axis).

In Figure 3.2, panel (b4), we show the specific energy release in the case $r = 0.2$: that will help us in interpreting the results obtained for the energetically preferred path. The deviation towards the vertical direction is well understandable considering that: (i) the elastic deformation energy decreases (then ΔW increases) approaching a compliant medium and, as a consequence, a deviation in the direction of a shorter path joining the crack to the compliant half space is preferred; (ii) the presence of a compliant medium, favours the opening of the upper dislocation elements, very close to the boundary transition; a greater opening of the uppermost dislocations implies an upper translation of the crack's centre of mass with higher release of gravitational energy. We evaluate the two energy

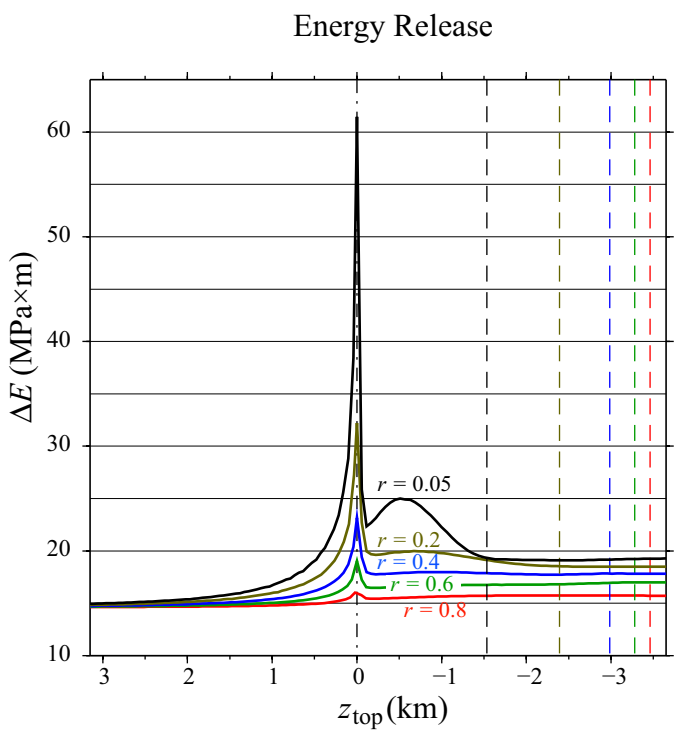

Figure 3.3: *CASE 1: specific total energy release ΔE, for different rigidity contrasts, plotted as functions of the z-coordinate of the top of the dike. Vertical dashed lines mark the position of the upper tip when the bottom tip crosses the interface.*

terms ΔW and ΔG separately. In this case we can immediately observe that the deformation energy release is almost null unless the dike is close to the transition surface and its contribution is almost an order of magnitude less than the gravitational contribution. The gravitational energy is dominant in driving the path of propagation across the elastic discontinuity, but it depends strongly on the elastic properties of the medium since, close to the boundary, the dike volume and shape change (influencing the overpressure through ΔP_K and displacing the centre of mass). Even if $\Delta W \ll \Delta G$, the elastic deformation contribution is not negligible: very close to a discontinuity in the elastic parameters (especially for low dip angles, low density contrast or other particular conditions, see also CASE 2) the differences of gravitational energy, between the energy release obtained for different directions of propagation, are of the same order as the elastic deformation differences and the elastic contribution becomes important for the direction of propagation.

In Figure 3.3 we show the specific energy release $\Delta E = \Delta W + \Delta G$ as a function of the vertical coordinate of the upper tip of the dike. It is interesting to notice (i) the constant rate of energy release during the straight propagation (far from the elastic discontinuity); (ii) the sharp peak (much higher for lower r) when the crack approaches the boundary of the compliant medium; (iii) the higher level of energy release until even the bottom tip of the crack has crossed the interface. These numerical results may help explaining (at least qualitatively) the observations of velocity variations in analogue models and agree with theoretical models studying the velocity of fluid-filled fractures in homogeneous media, where the internal fluid dynamics is considered: indeed, a constant energy release rate means a constant velocity considering a constant viscous dissipation during the motion (consistent with our results far from the elastic discontinuity); the peak in energy release means a sharp acceleration (the higher energy release is available to increase the kinetic energy of the dike filling fluid) that is consistent with the observation of fluid-filled fractures in layered gelatin (Rivalta et al., 2005, Fig. 4).

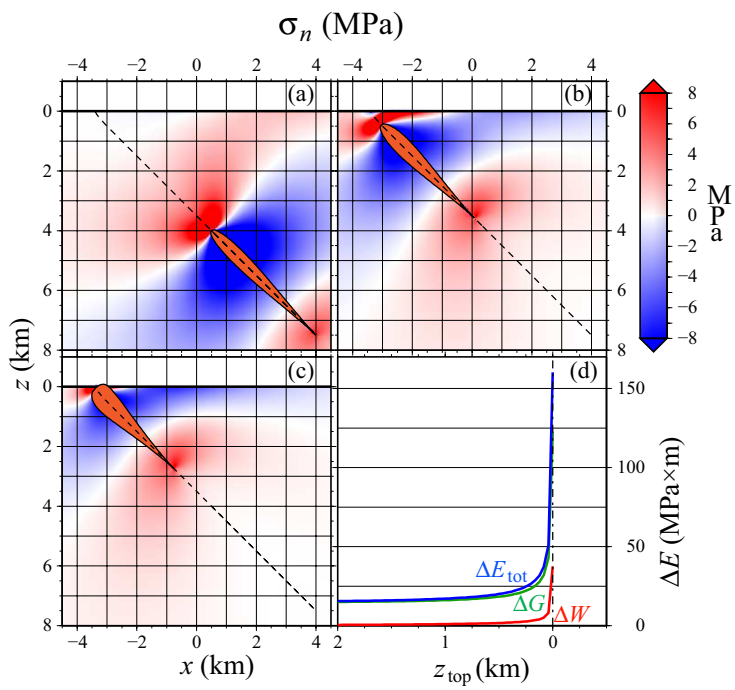

Figure 3.4: *CASE 1b: propagation of a* $45°$ *dipping, fluid-filled fracture, in a homogeneous half space with free surface. Panels (a) - (b) - (c) show the energetically preferred path (dashed line), the shape of the dike (exaggerated by a factor* 500*) and the normal stress induced by the crack in the elastic medium. Panel (d): diagram of the total specific energy release per unit of propagation and its contributions* ΔW *(elastic deformation energy) and* ΔG *(gravitational energy) plotted as functions of the* z*-coordinate of the top of the dike.*

3.1.3 CASE 1b (Free Surface)

Now we consider the propagation of the dike in a homogeneous half space with a rigidity $\mu = 30$ GPa, bounded by a free surface in $z = 0$. These results are obtained setting model parameters as in CASE 1, apart from $\mu_2 = 0$ ($r = 0$).

In Figure 3.4 we show in panels (a) - (b) - (c) the path of the crack, its shape and the stress induced in the elastic medium. The path followed by the crack is a straight line that ends with a deviation toward the vertical direction, affecting only the uppermost dislocation elements (hardly appreciable in the figure). In fact, this deviation, as in CASE 1, starts very close to the free surface: in this simulation we have a dike of 4.95 km length and we obtain a deviation from $45°$ to $60°$ for the dip angle, concentrated mostly in the shallowest 200 m of propagation (from 500 to 200 m depth the dip angle changes only from $45°$ to $48°$). On the contrary, the dike length is influenced by the free surface even at depths of the same order of the dike length: at the beginning of this simulation (4.00 km depth) the length of the dike is reduced by 1% in with respect to the length in an unbounded medium; 1.1 km depth it is shorter by 5% and at 550 m by 10%. The final length obtained in the simulation (at 20 m depth) is 25% less than the length obtained in a homogeneous unbounded medium. In the last panel of Figure 3.4 we show the gravitational and deformation energy contributions to the total energy release: even in the half-space the deformation energy release does not vanish (as it does in CASE 0), it is always much smaller than the gravitational contribution. Again, it is evident that the gravitational contribution increases significantly near the surface because the elastic response of the medium yields an increasing crack opening (and decreasing length) so that the centre of mass of the intrusion is displaced upward more than the upper tip.

The higher energy release close to the free surface explains the acceleration observed in gelatin experiments (Rivalta & Dahm, 2006), according to the arguments given at the end of the previous section.

3.1.4 CASE 2

In CASE 2 the rigidity of the upper medium is $\mu_2 = 30$ GPa. In this case we shall consider numerical values of the rigidity contrast $r = \{1.25; 1.66; 2.5; 5; 20\}$

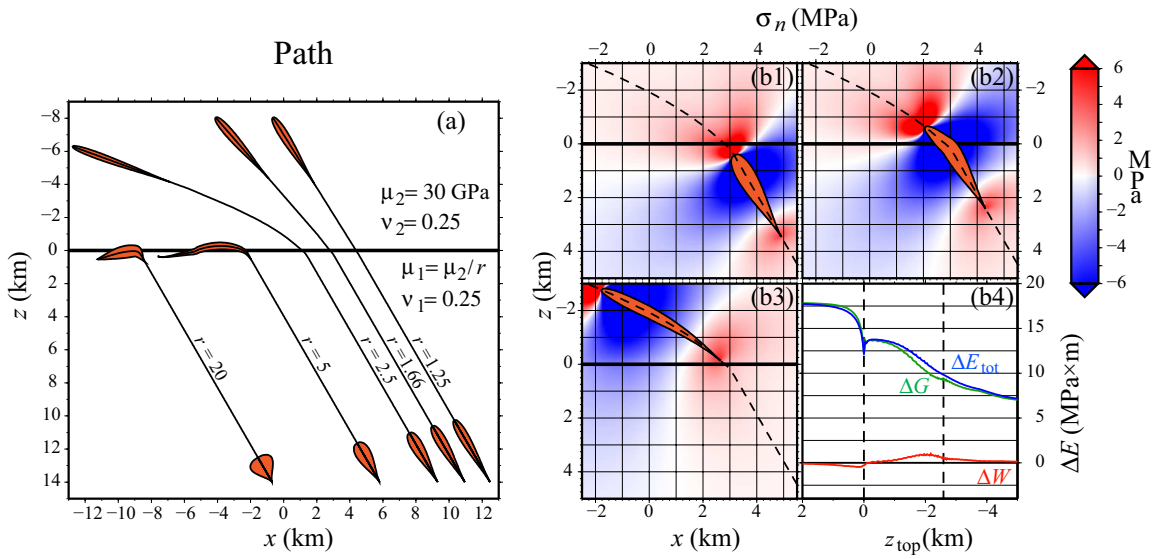

Figure 3.5: *CASE 2: propagation of a* $60°$ *dipping, fluid-filled fracture, in a layered elastic media. Panel (a): energetically preferred path and initial and final shape of the dike (exaggerated by a factor* 500*) for different rigidity contrasts. In this simulations we used an initial number of dislocation elements* $N = 43 - 71$ *and a test angle* $\alpha = (1-2)°$*. Panels (b1) – (b3): energetically preferred path (dashed line), shape of the dike (exaggerated by a factor* 500*) and normal stress induced in the medium, plotted in the dike reference frame, for* $r = 2.5$*. Panel (b4): total specific energy release plotted as function of the* z*-coordinate of the top of the dike.*

(reciprocal of CASE 1).

In Figure 3.5-a we show the path of the crack passing from a compliant to a stiffer medium. In this case we obtain a deviation toward the horizontal direction that is greater for a higher rigidity contrast; this effect, for differences of about an order magnitude in the rigidities, arrests the propagation: the dike assumes a lens shape along the interface ($r = 5$ and $r = 20$) and the stress intensity factor vanishes at both dike tips (in agreement with the assumption of vanishing fracture threshold). In this CASE 2 we observe an opposite (but greater) deflection with respect to CASE 1. This may be understood in the following terms: once the crack enters the stiffer medium, the test dislocation opens wider if it deflects toward the interface; the deflection continues until the whole crack has crossed (and the crack gets longer when entering a stiffer medium).

In Figure 3.5, panels (b1) - (b2) - (b3), we highlight changes in the shape of the dike approaching and crossing the boundary separating a compliant ($\mu_1 = 12$ GPa) from a stiffer medium ($\mu_2 = 30$ GPa) for which $r = 2.5$. While approaching and entering the stiffer medium, the normal stress increases due to the higher rigidity. In panel (b4), we show the contributions of gravitational and deformation energy to the total energy release: as in the previous cases, the magnitude of the deformation energy is much lower than the gravitational contribution. Anyway, as already noted for CASE 1, the gravitational energy is strictly connected to the dike shape which is governed by the elastic parameters and the variations of ΔW may be important in driving the direction of propagation. The deviation toward the horizontal direction is again understandable considering that: (i) the elastic deformation energy increases (ΔW decreases to negative values) approaching a stiffer medium; as a consequence, a deviation in the direction of the compliant half space is preferred; (ii) near the rigidity transition, the gravitational energy release decreases due to the less opening of the crack's head (and the consequent less advancement of the centre of mass) caused by the reaction of the stiffer medium.

In Figure 3.6, panels (a) - (b) - (c), we show changes in the shape of the dike approaching and crossing the boundary separating a compliant ($\mu_1 = 6$ GPa) from a stiffer medium ($\mu_2 = 30$ GPa) for which $r = 5$. Approaching and entering into the stiffer medium the normal stress increases due to the higher rigidity. In the final configuration, when the dike assumes a lens shape in the horizontal position,

	r	δ_{in}	δ_{fn}	α	l_{in} (km)	l_{fn} (km)	N_{in}	N_{fn}
CASE 1b	0	45°	60°	$\pm 1°$	4.95	3.75	99	75
CASE 1	0.05	45°	69°	$\pm 2°$	4.97	1.68	71	24
	0.2	45°	63°	$\pm 2°$	4.97	2.66	71	38
	0.4	45°	59°	$\pm 2°$	4.97	3.43	71	49
	0.6	45°	55°	$\pm 2°$	4.97	3.99	71	57
	0.8	45°	49°	$\pm 2°$	4.97	4.55	71	65
CASE 0	1	45°	45°	$\pm 2°$	2.70	4.98	45	83
CASE 2	1.25	60°	58°	$\pm 2°$	4.32	4.68	72	78
	1.66	60°	49°	$\pm 2°$	3.91	4.90	71	89
	2.5	60°	20°	$\pm 2°$	3.43	6.30	49	90
	5	60°	$sill$	$\pm 1°$	2.76	6.04	69	151
	20	60°	$sill$	$\pm 2°$	1.72	3.24	43	81

Table 3.2: *Results of the numerical model and initial (assumed) and final (computed) values of dike parameters.*

the stress decreases due to the low internal overpressure. Again we plotted the normal component of the stress tensor in the dike reference frame. In Figure 3.6 panel (d) we show the energy release as a function of the curvilinear abscissa (the path length starting from the upper tip in the initial configuration) normalised to its value when the crack crosses the transition boundary. When the crack assumes a low dip angle, the strain energy becomes dominant in driving the dike toward its final configuration.

In Figure 3.7 we show the total energy release as a function of the coordinate of the upper tip. The total energy release decreases sharply for higher rigidity contrasts. For moderate rigidity contrasts ($r = 1.25; 1.66; 2.5$) the propagation continues in the stiffer medium and the energy has a sharp local minimum in correspondence of the interface. The dike stops when $\Delta E = E_T$, what occurs even if the threshold E_T vanishes when $r = 5$ and $r = 20$. If $E_T > 0$, dike arrest may occur, typically close to the interface, for lower rigidity contrasts. These results are confirmed by experimental observations showing that fluid-filled fractures may stop in proximity of a transition to higher rigidity (Rivalta et al., 2005, Fig. 5).

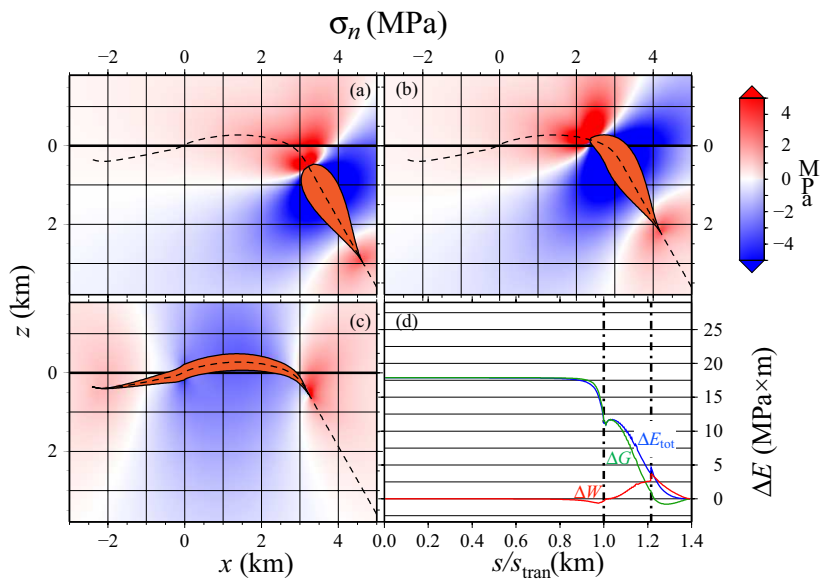

Figure 3.6: *CASE 2: propagation of a* $60°$ *dipping, fluid-filled fracture, in a layered elastic space with rigidity contrast* $r = 5$*. Panels (a) - (b) - (c) show the energetically preferred path (dashed line), the shape of the dike (exaggerated by a factor* 500*) and the normal stress induced by the crack in the elastic medium. In panel (d) the total specific energy release and its contributions* ΔW *(elastic deformation energy) and* ΔG *(gravitational energy) are plotted as functions of the distance travelled by the upper tip (normalised to the initial distance from the transition boundary.*

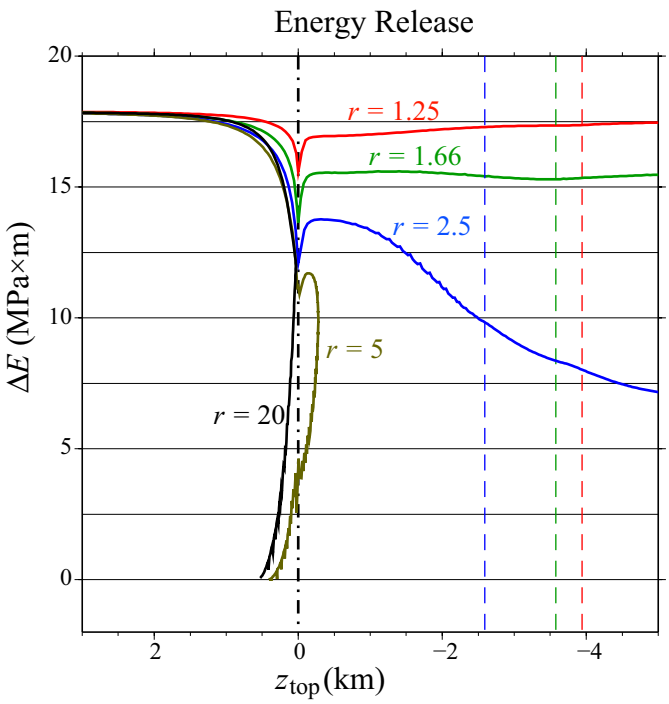

Figure 3.7: *CASE 2: specific total energy release for different values of rigidity contrasts, plotted as functions of the z-coordinate of the top of the dike. Vertical dashed lines mark the position of the upper tip when the bottom tip crosses the interface.*

3.1.5 Coulomb failure function and principal stresses close to an elastic discontinuity

An important aspect associated with dikes ascending in the crust is the seismicity due to the stress perturbation induced in the hosting medium by the dike's upper tip. This seismicity allows to localise a dike during the ascent and informs about its velocity and direction of propagation. Here I plot the Coulomb failure function (Cff) and calculate the axis relative to the maximum and minimum eigenvalues of the stress field induced by a dike in an elastic medium with a rigidity discontinuity. For each of the configuration proposed in section 3.1 I show results for a vertical (Fig. 3.8) and an inclined dike (Fig. 3.9). I used the simplest formulation for the Cff, defined as:

$$Cff = |\sigma_{xz}| + f \cdot \sigma_{xx}$$

where f is the friction coefficient and I took $f = 0.7$.
I plot the maximum Cff calculated on optimally oriented faults on planes perpendicular to the (x,z). I show also the maximum tensile (green lines and circles) and compressive (blue lines and circles) stress direction. From the Anderson theory of faulting, the dip angle of an optimally oriented fault (on which the Cff is maximum) deviates from the direction of the minimum stress eigenvector of $\pm\frac{1}{2}\arctan(f^{-1})$.

In Fig. 3.8 a vertical dike of 5 km length opens **a)** in a homogeneous medium; **b)** in a half-space at 1 km depth; **c)** in a medium with rigidity of 30 GPa at a distance of 1 km to the boundary separating a medium with rigidity of 12 GPa; **d)** the same as c) with inverse rigidities. Note that in Fig. 3.8 any external stress was considered in the medium, the Cff refers only to the stress field generated by the dike. In the homogeneous medium (Fig. 3.8-a) the maximum compressive stress over the upper tip of the dike is perpendicular to the (x,z) plane. In fact on the dike surface ($x = 0$) $\sigma_{xx} = \sigma_{zz}$ so that the minimum stress component results $\sigma_{yy} = \nu \cdot (\sigma_{xx} + \sigma_{zz})$. Note that on this plane I decided to plot the maximum eigenvector as horizontal, but this is an arbitrary choice: the maximum is equal on every direction in the plane (x,z). Near the plane $x = 0$ we have that σ_{xx} and σ_{zz} are both positive

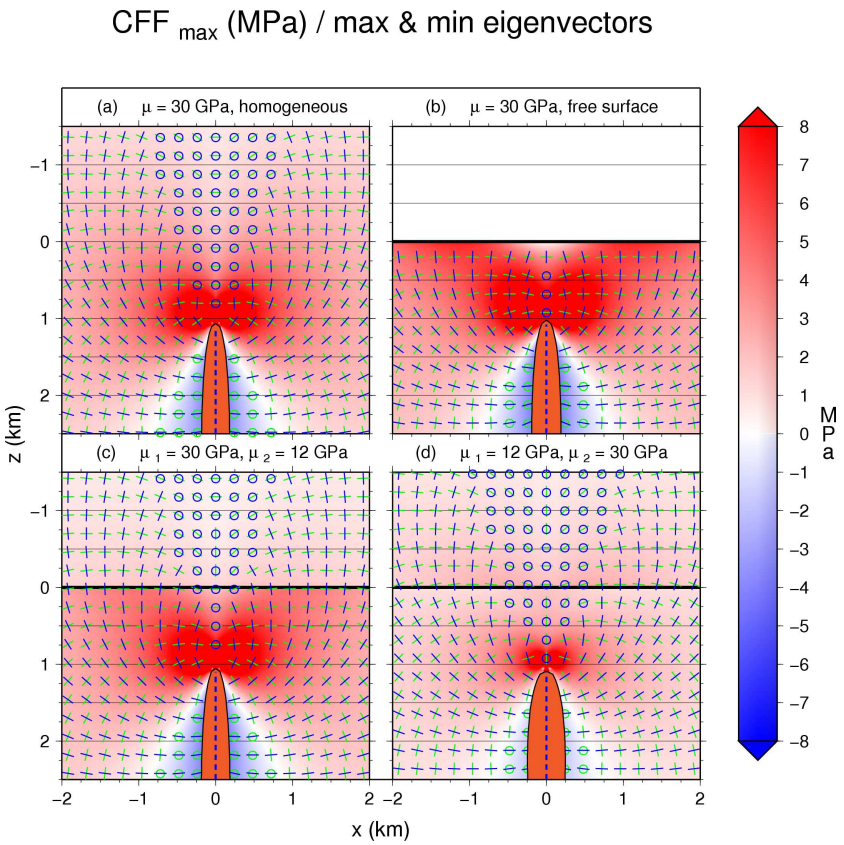

Figure 3.8: *Maximum Coulomb failure function on optimally oriented faults on planes perpendicular to the (x,z) for a vertical dike of 5 km length opening in a homogeneous medium (a), in a half-space (b), in a layered medium (d) and (e). Eigenvectors relative to the maximum (green) and minimum (blue) eigenvalue of the stress field due to the dike opening are plotted as lines if they are on the (x,z) plane or circles if they are perpendicular to (x,z).*

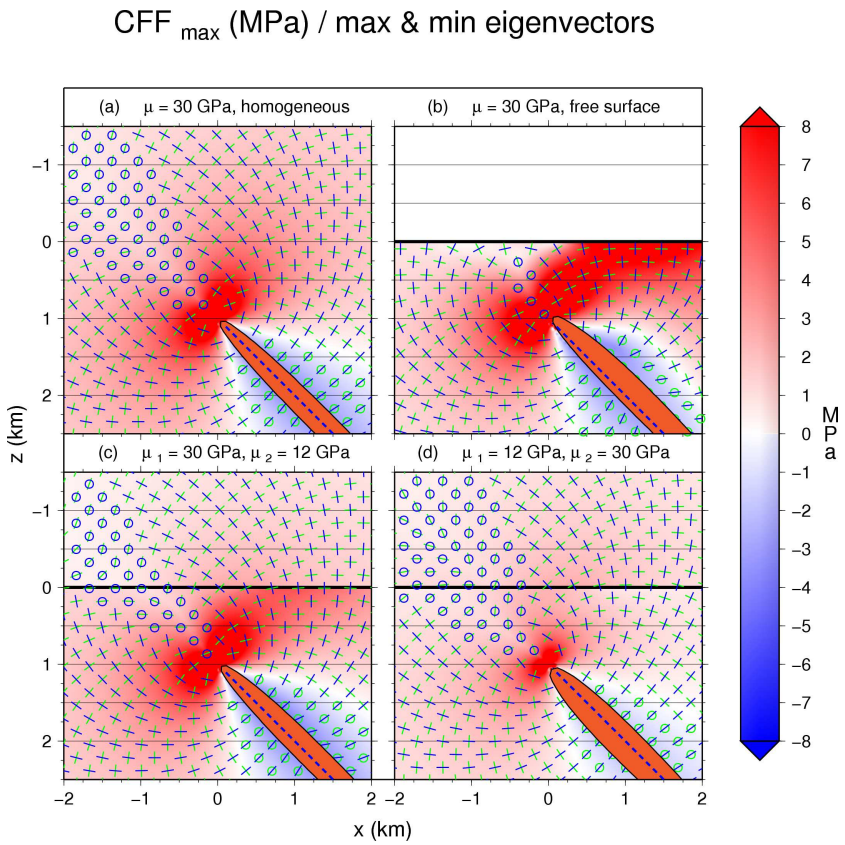

Figure 3.9: *Maximum Coulomb failure function on optimally oriented faults on planes perpendicular to the (x,z) for a 45° dipping dike of 5 km length opening in a homogeneous medium (a), in a half-space (b), in a layered medium (d) and (e). Eigenvectors relative to the maximum (green) and minimum (blue) eigenvalue of the stress field due to the dike opening are plotted as lines if they are on the (x,z) plane or circles if they are perpendicular to (x,z).*

and similar, so that again σ_{yy} results the minimum eigenvalue. It is interesting to notice that the uncertainty in the direction of maximum tensile stress is removed by the asymmetry introduced by free surface or the interface with a stiffer or compliant medium. In Fig. 3.8-b and 3.8-c, on the plane $x = 0$, the horizontal is effectively the direction of maximum tensile stress, in fact the presence of the free surface and of the compliant upper layer respectively, make the σ_{zz} component of the stress tensor lower than σ_{xx} (the effective rigidity in z direction is lower than in x direction). The opposite happens in the forth configuration (Fig. 3.8-d) were the effective rigidity in z direction is higher than in x direction, consequently the maximum eigenvalue is σ_{zz} and the tensile eigenvector is vertical. Looking at the Cff values, it is clear that faulting is favoured by the presence of a free surface or of a compliant upper layer. In this cases we expect shear fractures on planes inclined of an angle $\sim \pm\frac{1}{2}\arctan(f^{-1})$ ($\simeq 60°$ for $f = 0.7$) with respect to the vertical in the region where the Cff positive values are higher (approximately a line dipping at 40° – 50° from the surface to the dike upper tip).

In Fig. 3.9 a 45° dipping dike of 5 km length opens in the same configurations described above. Again an uncertainty for the direction of the maximum tensile axis is found in the homogeneous medium (Fig. 3.9-a) on the dike plane. Again I choose arbitrarily to plot the maximum eigenvectors on the crack surface perpendicular to the dipping direction of the dike. In the other cases the uncertainty is removed by the asymmetry introduced by free surface or the interface with a stiffer or compliant medium. In Fig. 3.9-b and Fig. 3.9-c is interesting to notice that the direction of maximum tensile stress, near the tip of the dike, does not results exactly perpendicular to the crack plane (as for a vertical dike) but tends to be parallel to the free surface (or interface). Moving away from the dike tip, on the crack plane, the maximum tensile stress becomes completely horizontal and continues its rotation overpassing the x direction.

The orientation of the maximum eigenvector of the stress field has a fundamental relevance for dike propagation: it is ascertained that the direction of propagation of a dike in an external stress filed tends to progressively deviate to the perpendicular direction with respect to the maximum tensile stress (see Watanabe et al., 2002). This rule seems to be applicable also to the stress field generated by the own dike. In fact, considering the behaviour of the maximum eigenvector on the

dike plane shown in Fig. 3.9-b and 3.9-c (and described above) and considering that the dike path, in presence of an external stress field, deflects to the perpendicular to the maximum tensile stress, we expect a deviation to the vertical direction for dikes that propagate to the free-surface or to the interface with a compliant medium (as predicted by the numerical results shown in the sec. 3.1.2 and 3.1.3). Moreover the opposite behaviour of the maximum tensile stress is shown in Fig. 3.9-d, where the upper layer is more rigid and the tensile eigenvector suggests the horizontal as favourite direction of propagation (as demonstrated in sec. 3.1.4).
Again, looking at the Cff values, it appears clear that the presence of the free surface or of the compliant upper layer favours fracturing of the host medium. In this cases we expect shear fractures on planes inclined of an angle $\sim 60°$ with respect to the compressive eigenvectors. In the red region of Cff, moving from the tip of the dike to the free surface (or interface), compressive axis dip from $\sim 45°$ to $\sim 90°$ (approximately on a line dipping at 30° – 40° from the dike upper tip to the surface).

3.2 Density and rigidity stratification

In this section we show results obtained considering a medium with density and rigidity layering.
We consider three different configurations: we start with the transition from a higher to a lower density layer, without introducing any rigidity transition in order to isolate the effect of the density layering (CASE 3); then we consider the same density configuration adding a rigidity transition from a stiff to a compliant medium (CASE 4). Finally we show the opposite configuration with transition from low to higher densities coupled with a rigidity transition from a compliant to a stiffer medium (CASE 5).

For each of the following cases we set the parameters of the mathematical model to the values reported in Table 3.3. The results for CASE 3, 4, and 5 are summarised in Table 3.4.

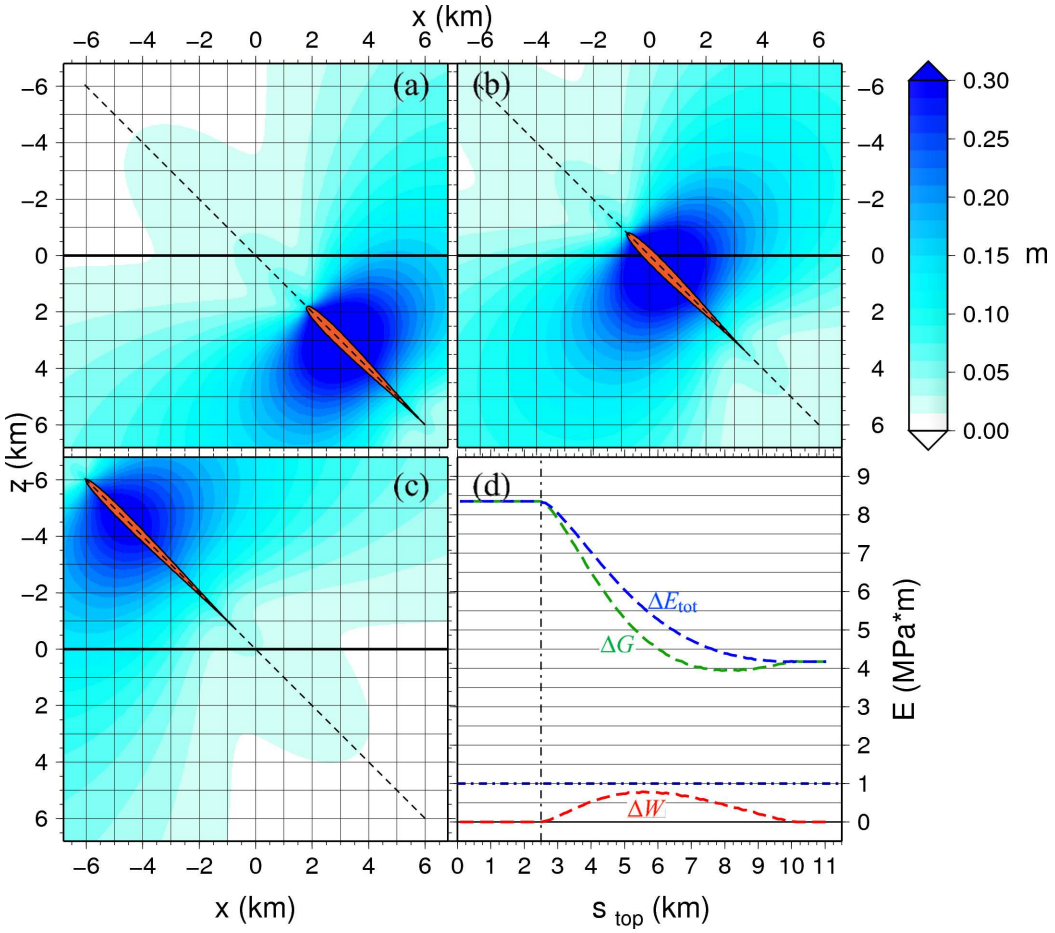

Figure 3.10: *CASE 3: propagation of a* $45°$ *dipping, fluid-filled fracture, in an elastic media with a density stratification of the type* $\rho_1 > \rho_2 > \rho_0$ *(where* ρ_0 *is the density of magma and* ρ_1 *and* ρ_2 *are the densities of lower and upper medium respectively). Panels (a), (b) and (c): energetically preferred path (dashed line), shape of the dike (exaggerated by a factor* 500*) and modulus of the displacement field. Panel (d): total specific energy release plotted as function of the* z*-coordinate of the top of the dike. The blue horizontal dashed line represents the energy threshold for propagation.*

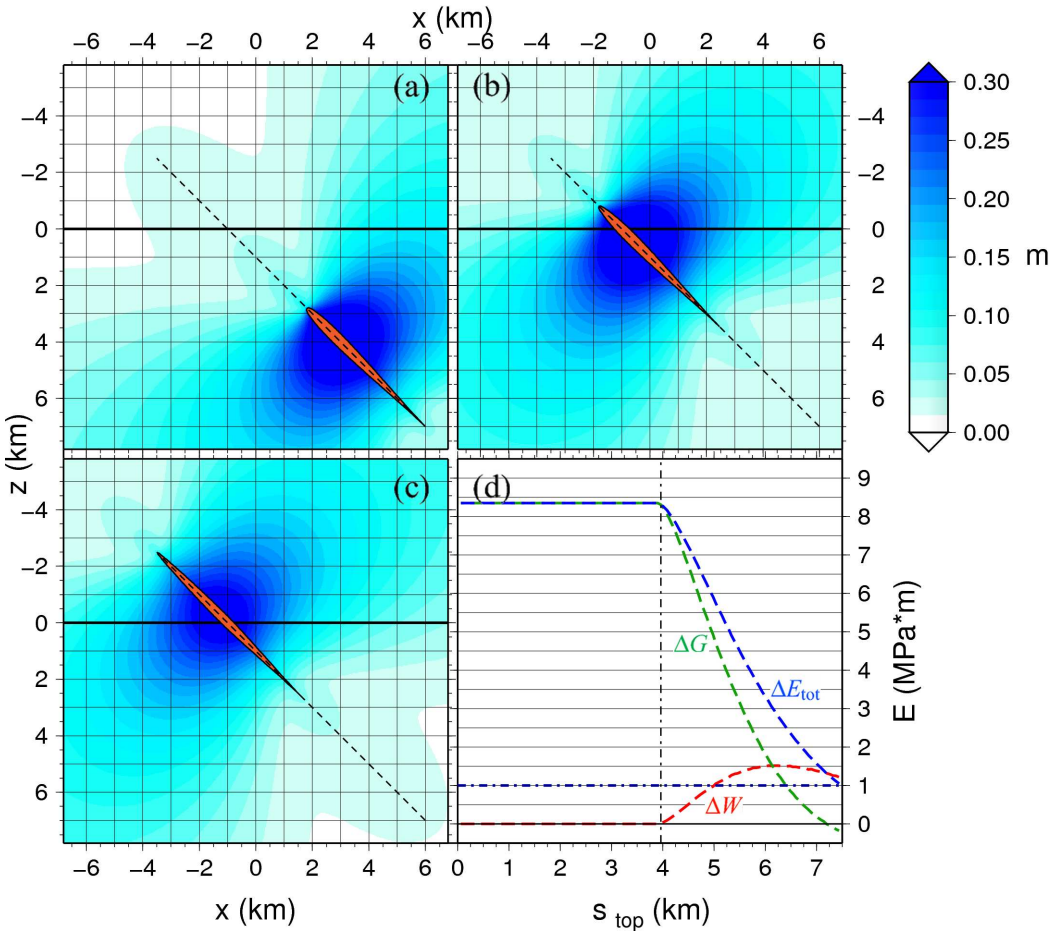

Figure 3.11: *CASE 3: propagation of a* $45°$ *dipping, fluid-filled fracture, in an elastic medium with a density stratification of the type* $\rho_1 > \rho_0 > \rho_2$*. Panels (a), (b) and (c): energetically preferred path (dashed line), shape of the dike (exaggerated by a factor* 500*) and modulus of the displacement field. Panel (d): total specific energy release plotted as function of the* z*-coordinate of the top of the dike. The blue horizontal dashed line represents the energy threshold for propagation.*

	ρ_1 (kg/m^3)	ρ_2 (kg/m^3)	ρ_0 (kg/m^3)	μ_1 (GPa)	μ_2 (GPa)
CASE 3	3000	2800	2600	30	30
	3000	2400	2600	30	30
CASE 4	3000	2800	2600	30	12
	3000	2400	2600	30	12
CASE 5	2800	3000	2600	12	30

Table 3.3: *Parameters used in CASE 3, 4, 5: ρ_0, is the reference density of the fluid intrusion, ρ_1, ρ_2, μ_1 and μ_2 are the densities and rigidities of the lower and upper layers respectively. In this cases we use a Poisson ratio $\nu = 0.25$ for the host rock. We consider a Bulk modulus $K_f = 10$ GPa and a volume (per unit length) $V_0 = 3 \cdot 10^{-3}$ km^2 for the intrusion.*

3.2.1 CASE 3

The path followed by the dike, its shape, the displacement field generated in the medium are plotted in Fig. 3.10 and 3.11, panels a-b-c. The specific energy release in Fig. 3.10 and 3.11 panel d. The rigidity is $\mu = 30$ GPa and the other parameters of the mathematical model are set according to Table 3.3.
In this case we consider two different density configurations: (i) we set the density of the upper medium lower than the density of the layer below but greater than the density of the intrusion: $\rho_1 > \rho_2 > \rho_0$ (shown in Fig. 3.10); (ii) we set the density of the upper medium lower of both: the density of the layer below and the density of the intrusion $\rho_1 > \rho_0 > \rho_2$ (shown in Fig. 3.11). In the last configuration magma is not buoyant with respect to the upper medium and the dike stops crossing the density transition.
Our model, in these configurations, shows straight propagation, suggesting that even if the contribution of elastic energy is generally smaller than that of gravitational, a change in host rock density along the dike's path is not sufficient to change its direction of propagation. As discussed in section 3.1.1, there is a strong interaction between elasticity and gravitational energy. The favourite direction of propagation results very often simply the direction of maximum opening of the last elements, that in absence of external stress or elastic heterogeneities, results the straight propagation.

In Figure 3.10, where the density of the upper medium was set to a higher

value than the density of the intrusion, the dike continues the propagation also within the upper layer, decreasing its opening due to the lower pressure gradient and increasing its length in order to conserve the mass of magma.
In Figure 3.11, where the density of the upper medium was set to a lower value than the density of the intrusion, the dike arrests when crossing the interface. Here we set the specific fracture energy threshold E_T (blue horizontal dashed line in panel d) to a constant value of 1 MPa·m (according to eq. 2.41 and 2.42 with a fracture toughness $K_c = 8.5$ MPa·km$^{1/2}$). Dike arrests when the specific total energy gained during the propagation becomes lower than the fracture energy threshold. Note that the contribution of elastic energy became essential for the last kilometre of propagation, where the gravitational contribution became lower than the energy threshold for propagation (green dashed line and blue horizontal dashed line in Fig. 3.11 panel d). At the arrest of the dike the stress intensity factor at the top is at the equilibrium with critical stress intensity factor of the host rock.

3.2.2 CASE 4

We show in Fig. 3.12 and 3.13 the output of the model for CASE 4: the path followed by the dike, its shape, the displacement field generated in the medium (panels a-b-c) and the specific energy release (panel d). In this case we choose a rigidity ratio $r = 0.4$ with $\mu_1 = 30$ GPa and $\mu_2 = 12$ GPa.
Also in this case we consider the same two different density configurations of CASE 3: $\rho_1 > \rho_2 > \rho_0$ (shown in Fig. 3.12) and $\rho_1 > \rho_0 > \rho_2$ (shown in Fig. 3.13). The densities employed for these simulations are listed in table 3.3. Again in the last configuration magma is not buoyant with respect to the upper medium and the dike stops when crossing the density transition.
In these configurations, the results of the mathematical model show a path followed by the dike that deviates from the straight propagation to the vertical direction. The two different density configurations do not change significantly the path of the dike. In Fig. 3.12 we show also (red dashed line) the path relative to a medium with homogeneous density ($\rho_2 = \rho_1$) with the same rigidity contrast ($r = 0.4$).

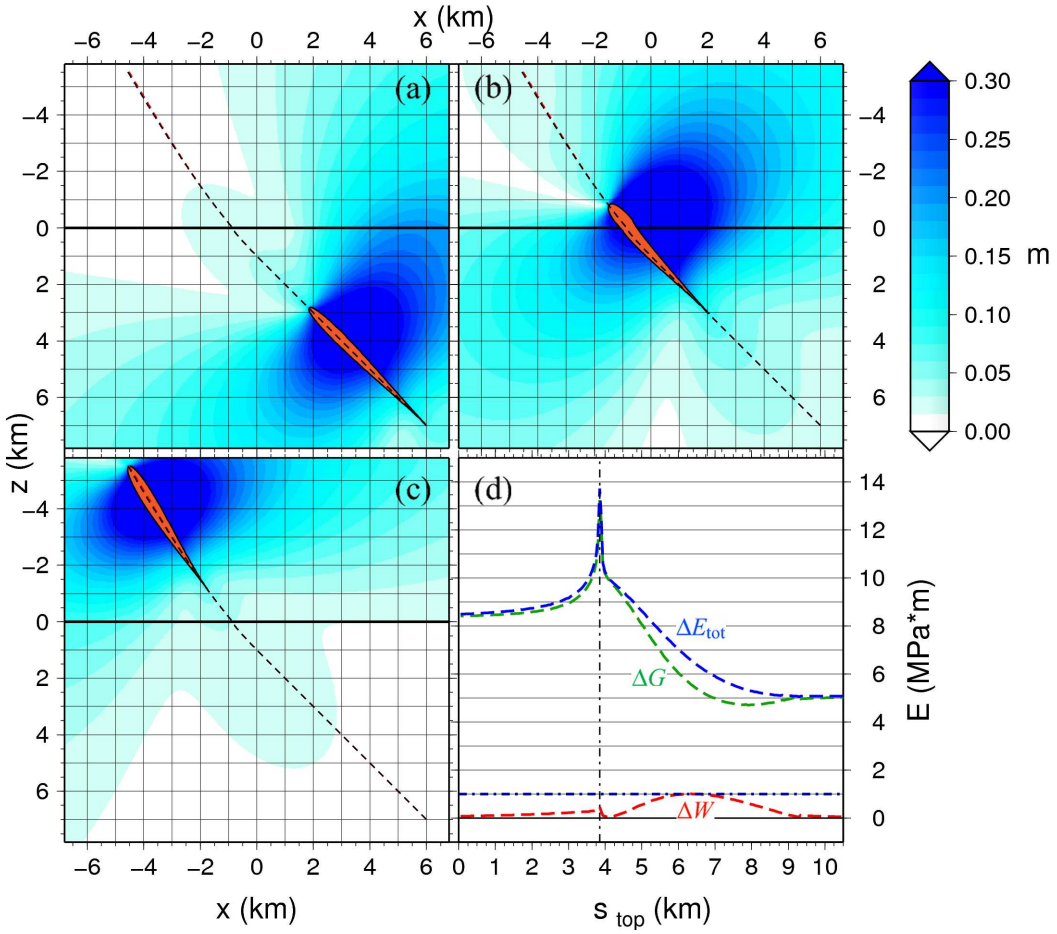

Figure 3.12: *CASE 4: propagation of a* $45°$ *dipping, fluid-filled fracture, in a layered elastic media with a density stratification of the type* $\rho_1 > \rho_2 > \rho_0$ *and rigidity stratification* $\mu_1 > \mu_2$*. Panels (a), (b) and (c): energetically preferred path (black dashed line), shape of the dike (exaggerated by a factor* 500*) and modulus of the displacement field. The red dashed line represents the energetically preferred path for* $\rho_2 = \rho_1$*. Panel (d): total specific energy release plotted as function of the* z*-coordinate of the top of the dike. The blue horizontal dashed line represents the energy threshold for propagation.*

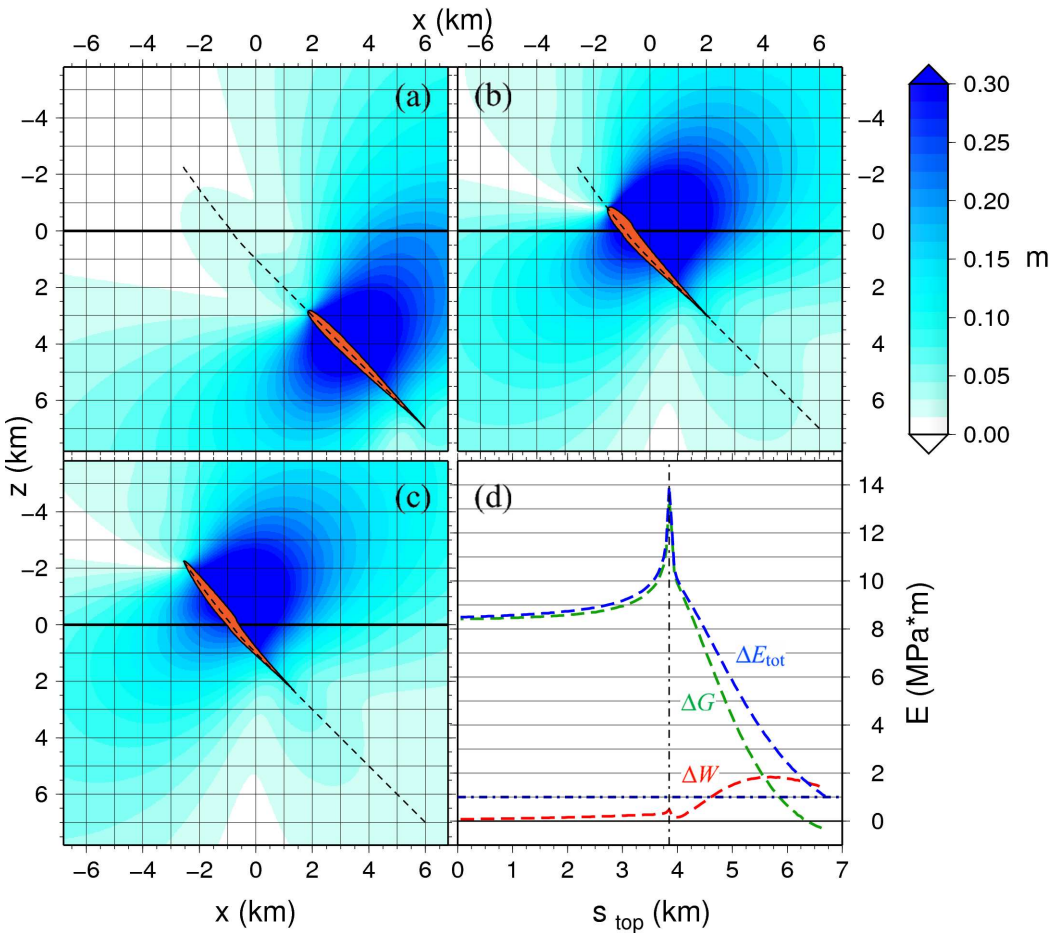

Figure 3.13: *CASE 4: propagation of a* $45°$ *dipping, fluid-filled fracture, in an elastic media with a density stratification of the type* $\rho_1 > \rho_0 > \rho_2$ *and rigidity stratification* $\mu_1 > \mu_2$*. Panels (a), (b) and (c): energetically preferred path (dashed line), shape of the dike (exaggerated by a factor* 500*) and modulus of the displacement field. Panel (d): total specific energy release plotted as function of the* z*-coordinate of the top of the dike. The blue horizontal dashed line represents the energy threshold for propagation.*

In Figure 3.12, where the density of the upper medium was set to a value larger than the density of the intrusion, the dike continues the propagation also in the upper layer changing its opening due to the lower pressure gradient and the lower rigidity. This two contributions act in the opposite direction: a lower density leads to lower overpressure and decreases the dike opening; a lower rigidity increases the opening at the same overpressure. The result is a shortening of 11% in the dike length.
In Figure 3.13, where the density of the upper medium was set to a lower value then the density of the intrusion, the dike arrests when crossing the interface. Note that also in this case, as the second configuration of CASE 3, the contribution of elastic energy became essential for the propagation in the last kilometre. Here the gravitational contribution became lower than the energy threshold and propagation is provided by the contribution of the elastic energy only (see Fig. 3.13 panel d). We set again the specific fracture energy threshold E_T (blue horizontal dashed line in panel d) to 1 MPa·m (fracture toughness $K_c = 8.5$ MPa·km$^{1/2}$). The dike arrests when the specific total energy gained during the propagation becomes lower than the fracture energy threshold.

3.2.3 CASE 5

We show in Fig. 3.14 the output of the model for CASE 5: the path followed by the dike, its shape, the displacement field generated in the medium (panels a-b-c) and the specific energy release (panel d). In this case we invert the rigidity ratio with respect to the CASE 4: $r = 2.5$ with $\mu_1 = 12$ GPa and $\mu_2 = 30$ GPa.
Here we consider only one density configuration: $\rho_2 > \rho_1$; this configuration certainly does not represent a typical geophysical scenario but we can refer our setting to a situation in which a rigid layer intrudes horizontally into a homogeneous matrix or (especially in volcanic areas) in which sedimentary rocks are deposited over a layer of tuffs or pyroclastic sediments. The densities employed for these simulations are listed in table 3.3. In Fig. 3.14 we show also (red dashed line) the path relative to a medium with homogeneous density ($\rho_2 = \rho_1 = 2800$ kg/m^3) and the same rigidity contrast ($r = 2.5$).
In this configuration, the results of the mathematical model show that the dike fol-

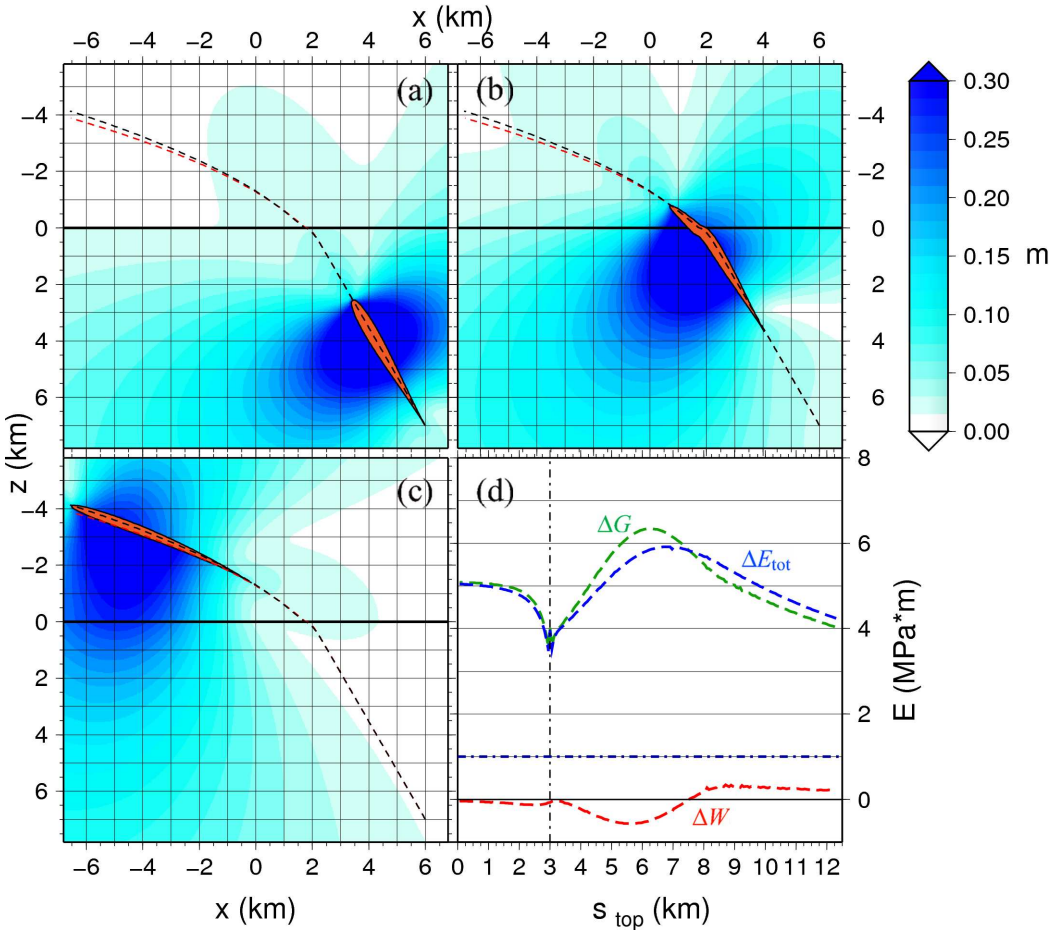

Figure 3.14: *CASE 5: propagation of a* $60°$ *dipping, fluid-filled fracture, in an elastic media with a density stratification of the type* $\rho_2 > \rho_1 > \rho_0$ *and rigidity stratification* $\mu_1 < \mu_2$*. Panels (a), (b) and (c): energetically preferred path (black dashed line), shape of the dike (exaggerated by a factor* 500*) and modulus of the displacement field. The red dashed line represents the energetically preferred path for* $\rho_2 = \rho_1$*. Panel (d): total specific energy release plotted as function of the* z*-coordinate of the top of the dike. The blue horizontal dashed line represents the energy threshold for propagation.*

	r	$\Delta\rho$ (kg/m^3)	δ_{in}	δ_{fn}	α	l_{in} (km)	l_{fn} (km)	N_{in}	N_{fn}
CASE 3	1	200	45°	45°	$\pm 1°$	6.00	7.60	75	95
		600 $^{(*)}$	45°	45°	$\pm 1°$	6.00	7.26	100	121
CASE 4	0.4	200	45°	59°	$\pm 1°$	5.95	5.30	119	106
		600 $^{(*)}$	45°	55°	$\pm 1°$	5.95	6.15	119	123
CASE 5	2.5	-200	60°	18°	$\pm 1°$	5.22	7.02	87	117

Table 3.4: *Results of the numerical model and initial (assumed) and final (computed) values of dike parameters. $\Delta\rho = \rho_1 - \rho_2$ is the difference between the density of the first and second layer respectively. The details of densities and rigidities employed in each case are listed in table 3.3. The asterisk $^{(*)}$ indicates a density configuration in which the magma is not buoyant in the upper medium ($\rho_1 > \rho_0 > \rho_2$), in this cases the dike arrests crossing the interface.*

lows a path that deviates from the straight propagation to the horizontal direction.

In this configuration the pressure gradient in upper medium is higher due to the grater density. Although the higher rigidity decreases the opening of the dike, moreover the deflection to the horizontal due to the rigidity transition decreases the pressure profile. The result is a lengthening of 35% in the dike length.
We set again the specific fracture energy threshold E_T (blue horizontal dashed line in panel d) to 1 MPa·m (fracture toughness $K_c = 8.5$ MPa·km$^{1/2}$). This values was not reached during the propagation so that the dike was not arrested.

3.3 Fracture toughness heterogeneities

In this section we show results obtained considering dike propagation in a medium made up of 2 half-spaces welded weakly. We reproduce this configuration in the mathematical model by setting the fracture toughness at the interface ($z = 0$) to a lower value with respect to the fracture toughness of the 2 homogeneous half-spaces.
We consider three different configurations: homogeneous medium with a weak-interface in $z = 0$ (CASE 6); then we consider a higher rigidity and more dense lower medium, below a compliant, less dense upper medium (CASE 7); finally we show the opposite configuration with a lower medium with low density and rigidity and an upper medium with higher rigidity and density (CASE 8).

	ΔE_T (MPa·m)	ρ_1 (kg/m^3)	ρ_2 (kg/m^3)	μ_1 (GPa)	μ_2 (GPa)
CASE 6	2.5	3000	3000	30	30
CASE 7	4.2	3000	2800	30	12
CASE 8	0.5	2800	3000	12	30

Table 3.5: *Parameters used in CASE 6, 7, 8: ΔE_T is the difference between the fracture energy threshold in the layers and at the interface: in this cases the fracture toughness of the media was ever greater than the fracture toughness on the surface $z = 0$; ρ_1, ρ_2, μ_1 and μ_2 are the densities and rigidities of the lower and upper layers respectively. In this cases we use a reference density $\rho_0 = 2600$ kg/m^3 for the fluid intrusion, a Bulk modulus $K_f = 10$ GPa and a volume (per unit length) $V_0 = 3 \cdot 10^{-3}$ km^2. We consider a Poisson ratio $\nu = 0.25$ for the host rock.*

For each of the following cases we set the parameters of the mathematical model to the values reported in Table 3.5.

3.3.1 CASE 6

We show in Fig. 3.15 the output of the model for CASE 6: the path followed by the dike, its shape, the displacement field generated in the medium (panels a-b-c) and the specific energy release (panel d). In this case we consider a homogeneous medium with a weak surface in $z = 0$.
We set the specific fracture energy threshold E_T (blue dashed line in panel d) to 4 MPa·m in the medium and to 1 MPa·m on the surface $z = 0$. The fracture energy drop make the interface ($z = 0$) the energetically preferred direction of propagation, in spite of the less efficient contribution to the total energy release of both: gravitational and elastic energy. Here (Fig. 3.15) and in the following 2 cases (Fig. 3.16 and 3.17) the black dashed line is the sum of the gravitational and elastic contributions (ΔG and ΔW) minus the fracture energy threshold (E_T). The dike arrests when the total energy release per unit lengthening (black dashed line) reaches zero. Note that in the last 2 km of the dike path, the propagation along the interface is allowed only by the contribution of the elastic deformation energy.

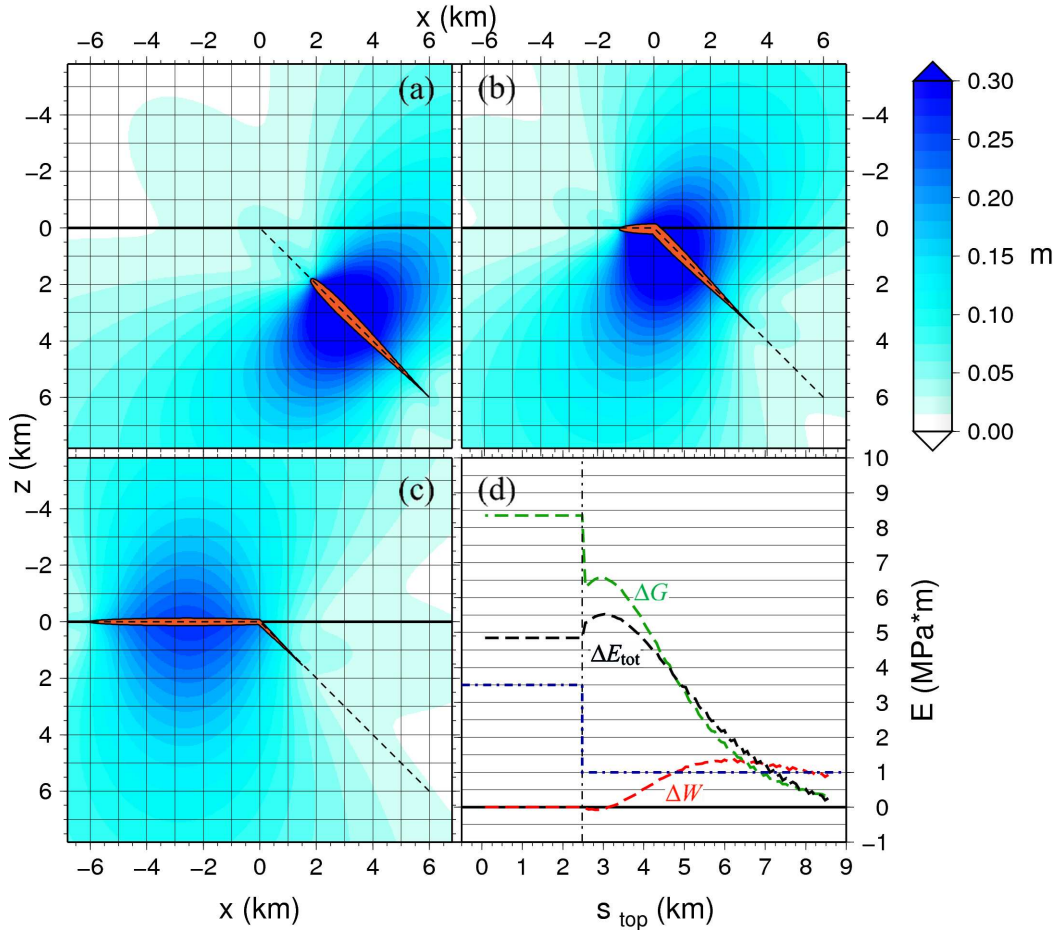

Figure 3.15: *CASE 6: propagation of a* $60°$ *dipping, fluid-filled fracture, in an elastic homogeneous medium with a weak surface in* $z = 0$*. Panels (a), (b) and (c): energetically preferred path (dashed line), shape of the dike (exaggerated by a factor* 500*) and modulus of the displacement field. Panel (d): total specific energy release plotted as function of the* z*-coordinate of the top of the dike. The blue dashed line represents the energy threshold for propagation filled by the dike during the propagation:* 8 *MPa·m in the medium (*$z > 0$ *or* $z < 0$*) and* 1 *MPa·m at the interface (*$z = 0$*).*

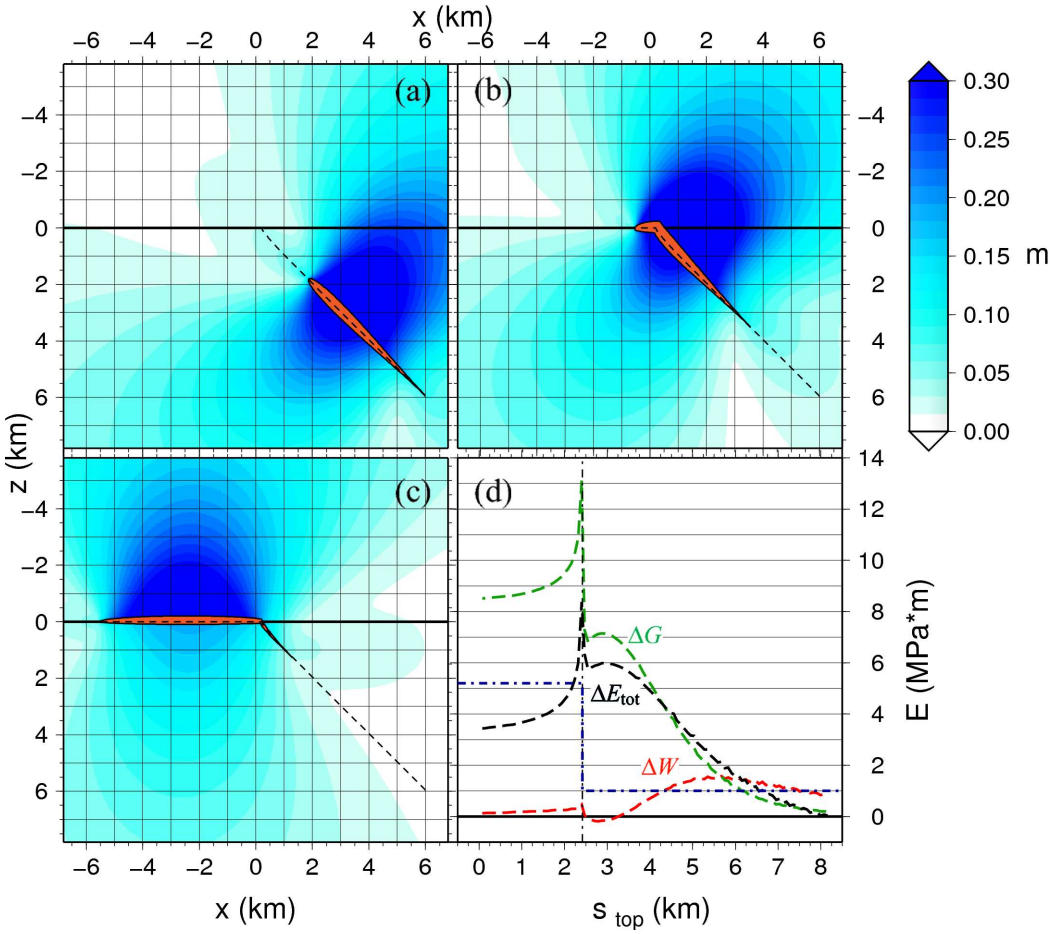

Figure 3.16: *CASE 7: propagation of a* $60°$ *dipping, fluid-filled fracture, in an elastic medium, with a weak surface in* $z = 0$*, made up of 2 homogeneous half-spaces: the lower with rigidity* $\mu_1 = 30$ *GPa and density* $\rho_1 = 3000$ *kg/m*^{3} *and the upper with rigidity* $\mu_2 = 12$ *GPa and density* $\rho_2 = 2800$ *kg/m*^{3}*. Panels (a), (b) and (c): energetically preferred path (dashed line), shape of the dike (exaggerated by a factor* 500*) and modulus of the displacement field. Panel (d): total specific energy release plotted as function of the* z*-coordinate of the top of the dike. The blue dashed line represents the energy threshold for propagation filled by the dike during the propagation:* 9 *MPa·m in the medium (*$z > 0$ *or* $z < 0$*) and* 1 *MPa·m at the interface (*$z = 0$*).*

3.3.2 CASE 7

We show in Fig. 3.16 the output relative to the configuration chosen in CASE 7. In this case we consider again a weak surface in $z = 0$; the elastic medium is made up of 2 homogeneous half-spaces: the lower with rigidity $\mu_1 = 30$ GPa and density $\rho_1 = 3000$ kg/m^3 and the upper with rigidity $\mu_2 = 12$ GPa and density $\rho_2 = 2800$ kg/m^3.
We set the specific fracture energy threshold E_T (blue dashed line in panel d) to 5.2 MPa·m in the medium and to 1 MPa·m on the surface $z = 0$. Again such a fracture energy drop along the interface make $z = 0$ the energetically preferred direction for propagation. Also in this case, as in the previous, the last 2 km of propagation along the interface, are allowed thank to the contribution of the elastic deformation energy.
Note that in this case we need a grater fracture energy drop in order to obtain dike propagation along the interface: in fact with this setting ($\mu_1 > \mu_2$), in absence of any fracture toughness discontinuity, we obtained (CASE 1 and 4) that the total energy release was maximised by a deviation to the vertical in the dike path.

3.3.3 CASE 8

In Fig. 3.17 we show the output for CASE 8. In this case we consider the opposite configuration with respect to CASE 7: lower half-space with rigidity $\mu_1 = 12$ GPa and density $\rho_1 = 2800$ kg/m^3 and upper half-space with rigidity $\mu_2 = 30$ GPa and density $\rho_2 = 3000$ kg/m^3. Again we set the weak surface in $z = 0$.
The specific fracture energy threshold E_T (blue dashed line in panel d) in the medium is 1.5 MPa·m and 1 MPa·m on the surface $z = 0$. Again we chosen a fracture energy drop along the interface high enough to make $z = 0$ the energetically preferred direction for propagation, in spite of the less efficient contribution of gravitational and elastic energy release. In this case, the last kilometre of propagation along the interface, is allowed by the contribution of the elastic deformation energy: here the gravitational contribution by them self should not be able to guarantee propagation.
Note that in this case a lower fracture energy drop is needed in order to obtain dike

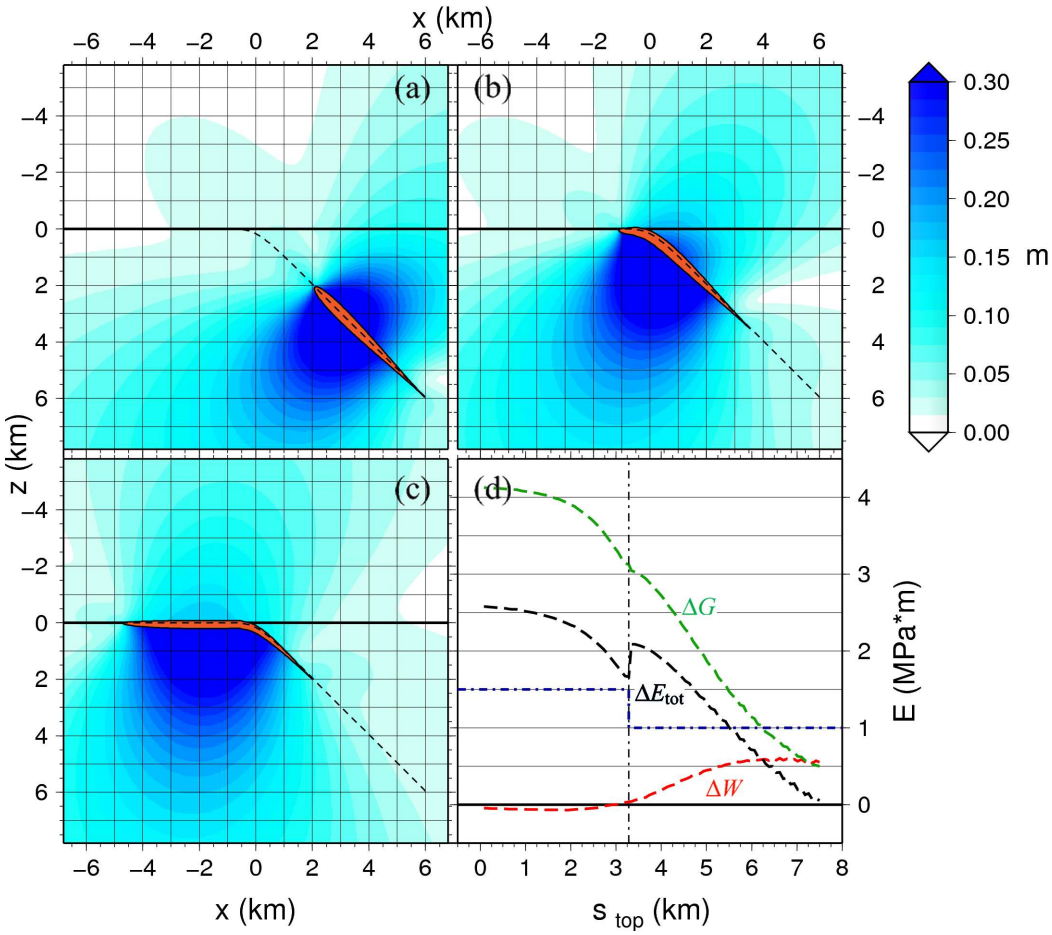

Figure 3.17: *CASE 8: propagation of a* $60°$ *dipping, fluid-filled fracture, in the opposite configuration of CASE 7: weak surface in* $z = 0$*,* $\mu_1 = 12$ *GPa,* $\rho_1 = 2800$ *kg/m*^{3}*,* $\mu_2 = 12$ *GPa,* $\rho_2 = 3000$ *kg/m*^{3}*. Panels (a), (b) and (c): energetically preferred path (dashed line), shape of the dike (exaggerated by a factor* 500*) and modulus of the displacement field. Panel (d): total specific energy release plotted as function of the* z*-coordinate of the top of the dike. The blue dashed line represents the energy threshold for propagation filled by the dike during the propagation:* 3.5 *MPa·m in the medium (*$z > 0$ *or* $z < 0$*) and* 0.5 *MPa·m at the interface (*$z = 0$*).*

propagation along the interface: in fact with this setting ($\mu_2 > \mu_1$), in absence of any fracture toughness discontinuity, we obtained (CASE 2 and 5) that the total energy release was maximised by a deviation to the horizontal in the dike path.

3.4 Discussion

Some of the results obtained from the numerical models were surprising to us: for instance, we expected that the dike should deviate significantly toward the vertical, even in a homogeneous medium, due to the buoyancy of the filling fluid. Instead, the dike dip remained constant in the numerical models, until the interface was reached. This was explained in section 3.1.1 (homogeneous medium) in terms of the more efficient upward displacement of the intrusion mass for rectilinear propagation. An experimental check of these results was provided by comparing our numerical findings with results from experiments in gelatin and will be presented in the next chapter.

Furthermore, the parameter values employed in the mathematical model need be discussed. The value assumed for magma density ρ_0 is much lower than the value $\rho_0 = \rho_r(1 - \alpha\Delta T)$ obtained for thermal expansion of the basaltic rocks (even a temperature difference $\Delta T \sim 10^3$ K provides $\Delta\rho \sim 100$ kg/m^3 only). Such small values of $\Delta\rho$ provide very low overpressure and very thin dike opening ($\Delta u \sim 10^{-2}$ m) employing deep crust rigidities ($\mu \sim 30$ GPa) and initial length $l \sim 10^3$ - 10^4 m. Such a thin dike, in presence of such a high ΔT, would become frozen in a very short time, which may be approximately estimated as $\sim \frac{\pi \Delta u^2 L^2 \rho_0}{4 k c_p \Delta T^2}$ (where L is the latent heat, ρ_0 is the density, k is the thermal conductivity and c_p the specific heat of magma) from Turcotte & Schubert (1982, Chapter 4). However it is not necessary that magma in the dike should be much hotter than the surrounding rocks in order to be fluid and lighter than the embedding medium: magma may be fluid because it is geochemically different than the surrounding rocks (which, even in source regions, are typically the refractory residual of the same primitive magma). Water, in particular, lowers consider-

ably the melting temperature. Moreover, at shallow depths, a highly vesciculated magma may easily be lighter than 2000 kg/m^3 with respect to 2900 kg/m^3 of basaltic rocks, without requiring a significant ΔT. A lower ΔT increases significantly the freezing time Δt, according to the previous formula. The value $\rho_0 = 2600$ kg/m^3, employed in the numerical model, (see Table 3.1) was arbitrary chosen within the reasonable range provided by the previous considerations. Field observations generally show dike thicknesses from a fraction of 1 m to several meters. The initial volume employed in our simulations (see Table 3.1) was chosen in order to provide ~ 1 m opening in a medium with 30 GPa rigidity. The opening increases up to a factor 10 when the dike enters a softer medium.

3.4.1 Numerical issues for an elementary dislocation close and across an elastic discontinuity

Here we show and discuss some results relative to an elementary closed dislocation, with overpressure assigned at its middle point, in proximity and across an elastic discontinuity.

As written in section 2.3 for the boundary element crack, the Burger vector of a single elementary closed dislocation, opening under assigned stress conditions, is chosen so that the stress due to the dislocation balances the pre-existent stress at its middle point. The choice to satisfy the equilibrium condition for the stresses at the middle point of the dislocation is justified only by the fact that this is the best choice in order to obtain a Burger vector, for the closed dislocation, that approximates well the maximum opening of a crack with the same (constant) pre-stress condition along the crack surface.

That means that, when the pre-stress on a dislocation surface is very far to be constant, we have no guarantee that the opening, obtained satisfying the equilibrium condition in the middle point of the dislocation, will be representative of the opening of a “real” crack. This is the case we are going to discuss. The presence of an elastic discontinuity generates an asymmetry of the stress field due to the elementary dislocation, and a discontinuity of the xx component of the stress tensor along the interface. In this case the stress field due to an elementary closed dislocation calculated at its middle point could be no more representative of the

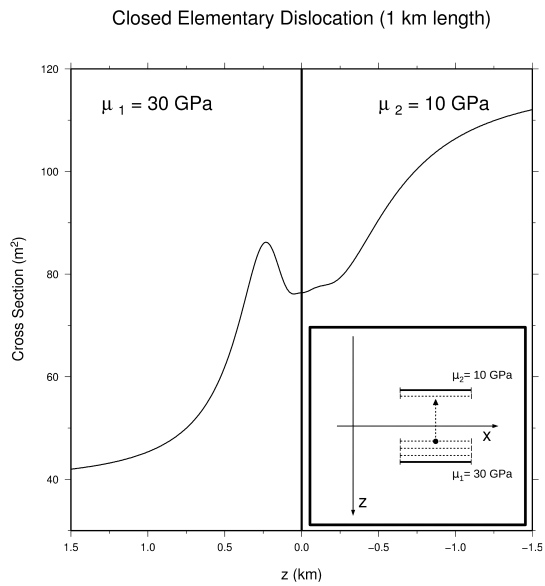

Figure 3.18: *Cross section area of a horizontal elementary closed dislocation as function of the z coordinate of its middle point in an elastic medium with rigidity transition in $z = 0$. The dislocation length is 1 km and the assigned overpressure is 1 MPa.*

opening of the dislocation. As a consequence an unreasonable Burger vector is required to balance the forces at the centre of the dislocation.

In Fig. 3.18 we show the opening of a horizontal elementary closed dislocation, with assigned constant overpressure, as a function of its z coordinate in a medium with an elastic discontinuity in $z = 0$. It is evident that the cross section of the elementary dislocation should grow monotonically while it is moving upward, since it is feeling a lower effective rigidity. On the contrary we obtain a relative maximum in the stiffer medium, near to the rigidity transition. This effect is clearly due to the closeness of the elastic discontinuity. In fact the distance at which we observe the anomalous maximum depends on the length of the dislocation: in Fig. 3.19 we shows the results of the same test performed with 2 boundary elements cracks with 10 and 100 elements respectively. In Fig. 3.19-a (10 elements crack) the maximum and the distance at which it appears, are reduced of a order of magnitude and in 3.19-b (100 elements crack) of 2 orders (resulting unnoticeable in the graph).

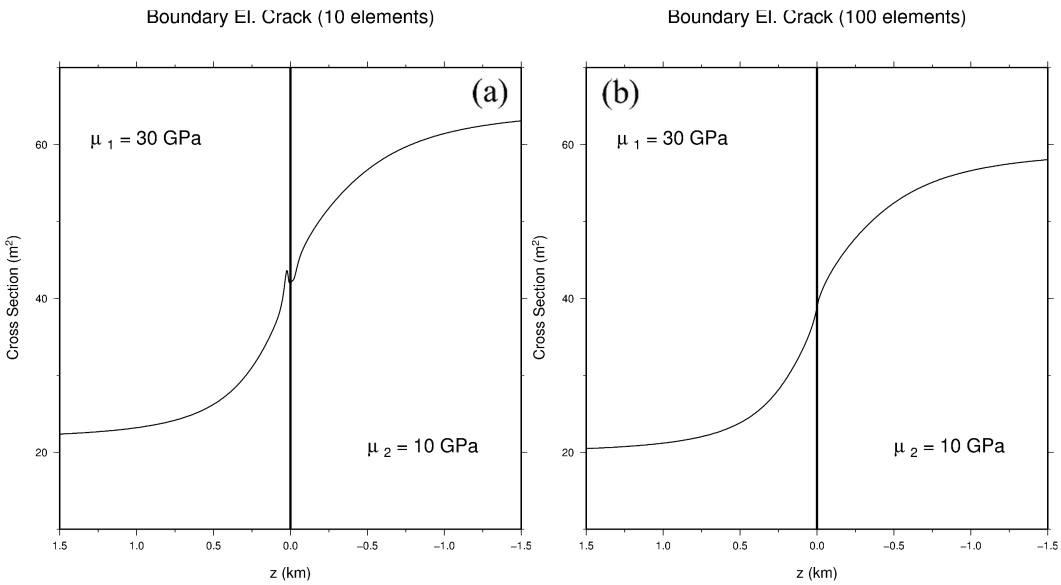

Figure 3.19: *Cross section area of a horizontal boundary elements crack as function of the z coordinate of its middle point in an elastic medium with rigidity transition in $z = 0$. Panel a and b refer to a crack made of 10 and 100 elements respectively. The crack length is 1 km and the assigned, constant overpressure is 1 MPa.*

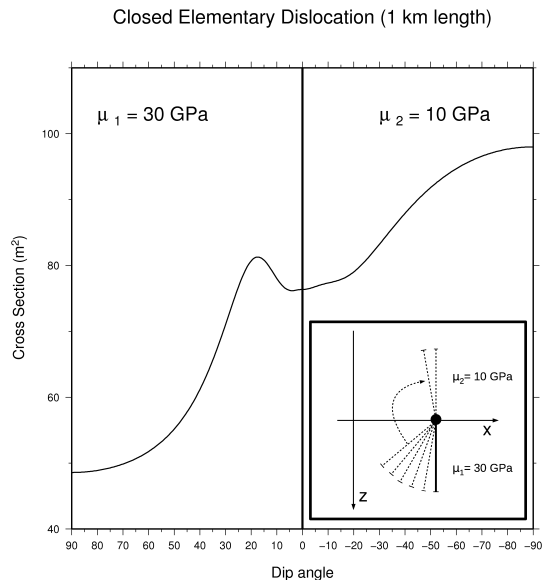

Figure 3.20: *Cross section area of a tilted elementary closed dislocation as function of the dip angle δ. The dislocation has a tip on the interface $z = 0$ that is a rigidity transition surface. The dislocation length is 1 km and the assigned overpressure is 1 MPa.*

This effect may introduce an error in the choice of the favourite direction for the opening of a single dislocation very close to the rigidity transition: in Fig. 3.20 we perform an analogous test fixing a tip of the elementary closed dislocation on the interface $z = 0$ and varying the dip angle from $90°$ to $-90°$ (see the insert in Fig. 3.20).

We obtain also in this case an analogous graph, with a relative maximum for a dip angle $\delta = 27.5°$. Using a boundary elements crack, or moving the dislocation away from the discontinuity, this effect progressively (and quickly) disappears.

The fact that this effect scales with the linear dimension of the elements of the crack, makes us confident that the possible errors introduced in our model are restricted to a region around the interface with thickness of maximum 2 elements of the boundary elements crack. Increasing the number of elements in our simulation we reduce the influence of this effect and we find stable paths for cracks made of 40-50 elements or more.

In Fig. 3.21-a we show the opening of a vertical elementary closed dislocation,

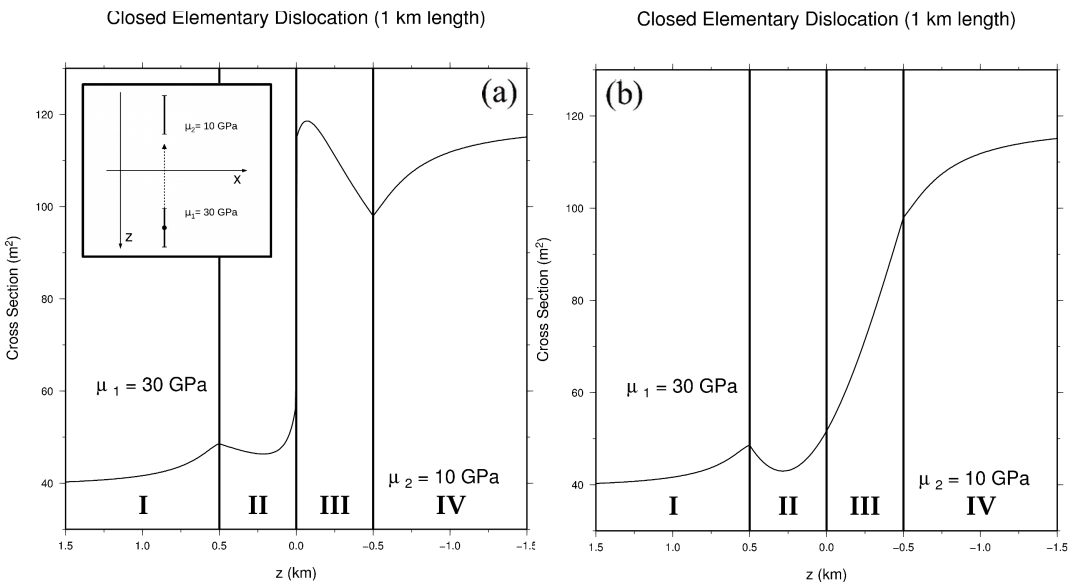

Figure 3.21: *Cross section area of a vertical elementary closed dislocation as function of the z coordinate of its middle point in an elastic medium with rigidity transition in $z = 0$. The dislocation length is 1 km and the assigned overpressure is 1 MPa. In panel b, where the dislocation is across the interface (region II and III), the dislocation is split in 2 elements in correspondence of $z = 0$.*

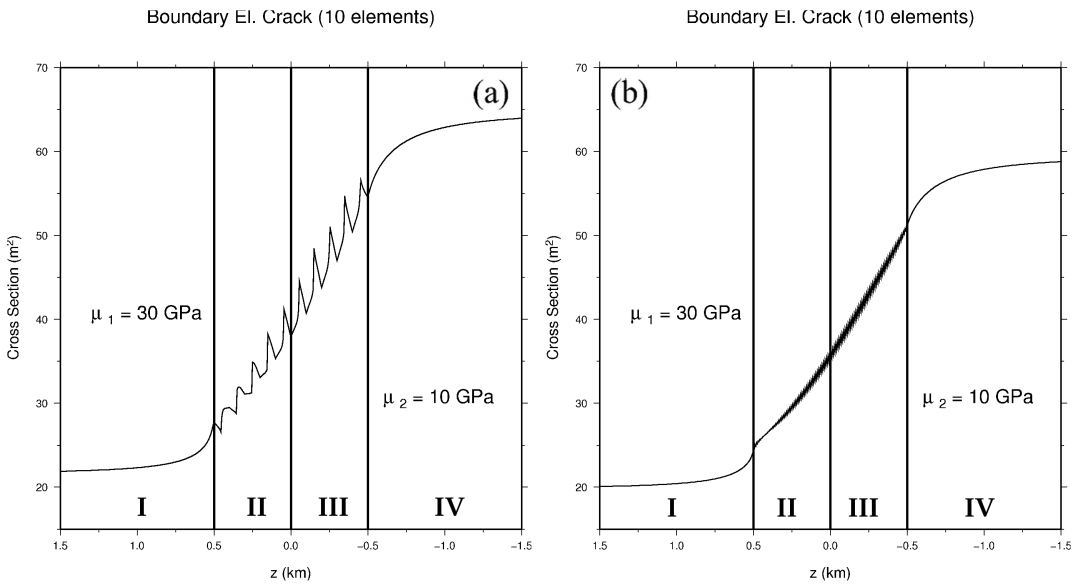

Figure 3.22: *Cross section area of a vertical boundary elements crack as function of the z coordinate of its middle point in an elastic medium with rigidity transition in $z = 0$. Panel a and b refer to a crack made of 10 and 100 elements respectively. The crack length is 1 km and the assigned, constant overpressure is 1 MPa.*

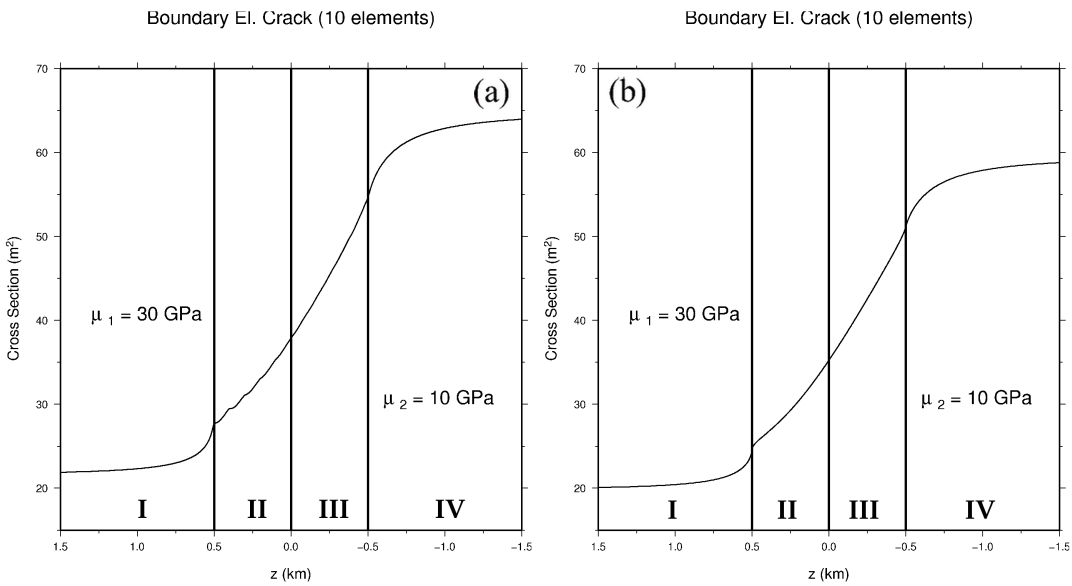

Figure 3.23: *Cross section area of a vertical boundary elements crack as function of the z coordinate of its middle point in an elastic medium with rigidity transition in $z = 0$. Panel a and b refer to a crack made of 10 and 100 elements respectively. The crack length is 1 km and the assigned, constant overpressure is 1 MPa. Here, when an element is across the interface, it is split in two in correspondence of $z = 0$.*

with assigned constant overpressure, as a function of its z coordinate in a medium with an elastic discontinuity in $z = 0$. The graph is divided in 4 region in which the dislocation is: (I) totally embedded in the lower half space ($\mu_1 = 30GPa$); (II) across the interface with its middle point in the lower half space; (III) across the interface with its middle point in the upper half space; (IV) totally embedded in the upper half space ($\mu_2 = 10GPa$). Also in this case we expect that the cross section of the dislocation grows monotonically approaching and entering in the upper compliant medium. On the contrary, we obtain, Fig. 3.21-a, that the opening of the elementary dislocation, under constant overpressure condition, has an unexpected behaviour in region II and III. In region II we observe an unreasonable relative minimum for $z = 0.2km$ (the length of the dislocation is 1 km) with the cross section of the dislocation that decreases from $z = 0.5$ to $z = 0.2$. In region III we obtain a relative maximum for $z = -0.05$ and the cross section decreases from $z = -0.05$ to $z = -0.5$. Moreover the graph in Fig. 3.21-a shows a discontinuity in $z = 0$ that consists in a sudden change in the opening of the dislocation when its centre oversteps the interface. The discontinuity in the opening can be related to the discontinuity in $z = 0$ of the σ_{xx} component of the stress field. In fact the compressive stress, induced by an elementary dislocation across the interface, "accumulates" in the stiffer half-space, in proximity of the rigidity transition, and quickly falls down in the compliant half-space. When the elementary dislocation is across the transition, the presence of such highly variable compressive stresses on the dislocation surface makes the middle point of the dislocation not the best location to calculate the Burger vector that satisfies the equilibrium of stresses
In Fig. 3.21-b we present the same case splitting, in correspondence of $z = 0$, the dislocation which is across the interface, into two elementary closed dislocations. We can appreciate that the discontinuity in $z = 0$ disappears as the maximum in the region III. Again we observe a relative minimum in region II (for $z = 0.25$) and in general, for region II and III, the opening of the dislocation appears to be underestimated. That is understandable considering that an elementary dislocation always overestimates the cross section of a crack and in region II and III, in which we use a 2 elements crack, a generic reduction of the cross section is expected.
In analogy with the previous case (horizontal dislocation) we try to by-pass the

problems due to the elementary dislocation approximation, introducing a boundary elements crack. In Fig. 3.22 we show results obtained for a crack built with 10 elements (3.22-a) and 100 elements (3.22-b). As expected the discontinuity in the cross section decrease in amplitude but is cyclically reproduced each time that a dislocation element passes the interface.

The undesired effect seems to be conclusively solved using a boundary elements crack and splitting into two elements the dislocation each time which it is across the interface. In Fig. 3.23-a and 3.23-b we show respectively a 10 and 100 elements crack with no dislocations across the interface.

Chapter 4

Analogue models

Here we compare our numerical findings with results from experiments in gelatin. We used 200 Bloom gelatin powder from the company AG Stoess. The gelatin is diluted in water at different concentrations in order to control the resulting rigidity of the gelatin mass. It is poured into a cylindrical container (diameter $d = 29$ cm, height $H = 40$ cm). We inject a lighter fluid (air) from an inclined hole at the bottom of the container close to the lateral walls (see Fig.3.10). Poisson's ratio for gelatin is very close to $\nu = 0.5$ (gelatin has about the same compressibility as water). Dike propagation is recorded with High Definition Camcorders. We measure incidence and refraction angles of the crack trajectory inspecting snapshots of the recorded movies.

Propagating cracks filled with viscous fluids show a characteristic shape with a head region followed by a thin channel where a little portion of the fluid is left behind. The less viscous the fluid, the thinner the channel. Because of its low viscosity, air seemed the best choice for our purpose, since the air mass left behind by the head of the fracture during propagation is negligible.

In order to compare the 3D experimental results, obtained in a medium with finite dimensions, with numerical results obtained from a 2D plane strain model in an unbounded medium, a few considerations are needed. The first problem to be taken into account is the lateral dimension w of the dike (which is infinite in the plane strain model). During propagation in the 2D model we imposed conservation of the mass per unit length $M_0 = V_0 \cdot \rho_0$. In order to estimate the

Figure 4.1: *Experimental set-up.*

corresponding 3D volume $V_0^{(3D)}$ (and conserve the total mass $M_0^{(3D)} = V_0^{(3D)}\rho_0$) we must evaluate the breadth w of fluid-filled fractures. In the analogue experiments we observe that w is typically smaller than, but similar to, its length L. In a plane strain model, the 2D volume for a tear-drop crack (assuming a homogeneous medium, linear overpressure profile with vanishing Stress Intensity Factor at the trailing edge) is

$$V_0 = \left[\frac{\pi(1-\nu)\Delta\rho\, g \sin\delta}{2\mu}\right]\left(\frac{L}{2}\right)^3$$

so that

$$L = 2\left[\frac{2\mu}{\pi(1-\nu)\Delta\rho\, g \sin\delta}\cdot V_0\right]^{\frac{1}{3}}$$

it is a sufficiently good approximation, to our purpose, to write the 3D volume as:

$$V^{(3D)} \approx V_0 \cdot \frac{w}{2}$$

Finally, considering the breadth $w \approx \frac{3}{4}L$ (from lab. observations), we can write:

$$V^{(3D)} \approx V_0 \cdot \frac{3}{8}L = \frac{3}{4}\left[\frac{2\mu}{\pi(1-\nu)\Delta\rho\, g \sin\delta}\right]^{\frac{1}{3}} V_0^{\frac{4}{3}} \tag{4.1}$$

From the product $V^{(3D)}\rho_0$ we estimate the intrusion's mass as:

$$M_0^{(3D)} = \frac{3}{4}\left[\frac{2\mu}{\pi(1-\nu)\Delta\rho\, g \sin\delta}\right]^{\frac{1}{3}} V_0^{\frac{4}{3}} \cdot \rho_0 \tag{4.2}$$

For example, according to eq. (4.2), for the dikes considered in the previous simulations (see Table 3.1 for the employed reference values), with μ varying in the range $(1.5 \div 30)$ GPa, we obtain $M_0^{(3D)} \approx (0.8 \div 2.3)10^8$ kg. This mass represents the order of magnitude of the mass of a real dike having a cross section $V_0 = 100\, m^2$ on the plane (x, z). Moreover, in our 2D model, we conserve the product $V_0 \cdot \rho_0$, representing a mass per unit length. As a consequence, if the breadth of the corresponding 3D dike were to change during propagation (in particular when it crosses the interface between different layers), the total mass $M_0^{(3D)} = \frac{1}{2}V_0 w \rho_0$ would change. This is clearly an intrinsic limitation of a plane strain model, in which mass flow in the strike direction is forbidden. During experiments in layered gelatin, we observe that the relative change of w is typically small, so that we shall consider w constant; this means that the 2-D mass M_0 given by eq. (4.2) remains approximately constant during propagation even for a 3D dike. In the next paragraph, when we show the comparison between numerical and analogue models, we use eq. (4.1) to set the input 2D volume V_0, knowing the real injected volume V_{in}.

Another problem concerns the finite dimensions of the medium in the analogue experiments. We try to simulate a semi-infinite half-space as closely as possible by producing gelatin layers much thicker than the crack length and similar to the lateral dimension of the container. As far as the propagation path is concerned, observations show that a crack feels appreciably the presence of the container and of the interface between layers only when it is much closer to them than its length L.

Finally, we run our numerical code employing the measured values of density

r	μ_1 (kPa)	μ_2 (kPa)	V_{air} (ml)	δ_{in}	δ_{fn}	δ_{fn}^{th}
0	1.20 ± 0.15	-	2.0 ± 0.2	$(55 \pm 1)^\circ$	$(55 \pm 1)^\circ$	$(55 \pm 2)^\circ$
0.37	1.6 ± 0.2	0.6 ± 0.1	10 ± 1	$(68 \pm 1)^\circ$	$(72 \pm 1)^\circ$	$(73 \pm 1)^\circ$
1.73	1.10 ± 0.15	1.9 ± 0.2	8 ± 1	$(65 \pm 1)^\circ$	$(50 \pm 1)^\circ$	$(52 \pm 10)^\circ$

Table 4.1: *Parameters employed in the numerical runs to reproduce the analogue experiments: r is the rigidity contrast, $\mu_{1,2}$ are the measured rigidities respectively of the lower and upper gelatin layers, V_{air} is the volume of the intrusion. $K_f = 140\,\mathrm{kPa}$, $\nu = 0.5$ and $\rho_{gel} = 10^3\,\mathrm{kg/m^3}$ are, respectively, the bulk modulus assumed for the air intrusion, the Poisson ratio and the density assumed for both gelatin layers. The experimentally determined initial value of the dip angle is δ_{in} and the final dip δ_{fn} is compared with the theoretical value δ_{fn}^{th} with error bounds computed taking into account the uncertainty in μ_1, μ_2. Note that the calculated dip angle δ_{fn}^{th} for $r = 0$ represents the average dip angle while only the last 4 out of 71 elements deviate from the straight direction (the uppermost dips at 67°).*

and rigidity of the gelatin layers, the values of density, compressibility and initial volume of the air intrusion (see Tab. 4.1) and compare the results of the analogue and the numerical models.

4.1 Experimental results: CASE 0 (free surface)

We injected a volume $V_{in} = 2$ ml of air into a homogeneous gelatin layer with rigidity $\mu = 1.2 \pm 0.2$. The path of propagation is shown in Fig.4.2. Crack propagation is very slow and rectilinear, until the upper tip gets very close to the free surface as predicted in section 3.1.3. The initial dip angle is $\delta_{in} = (55 \pm 1)^\circ$ and do not change until the crack gets the free surface: the measured final dip angle is $\delta_{fn} = (55 \pm 1)^\circ$. Shape and angles resulting from a correspondent run of the numerical code are shown in Fig.4.3, where a dashed line indicates the path obtained setting the fluid parameters according to Table 4.1 and the elastic parameters as reported in panel 4.2-a4. In this case, from the mathematical model we obtain a deviation to the vertical direction for the dip angles of the last elements 4 elements (over 71). The deviation resulting from the mathematical simulation, involves the last 2.5 mm of propagation for a crack with initial length of 5.2 cm.

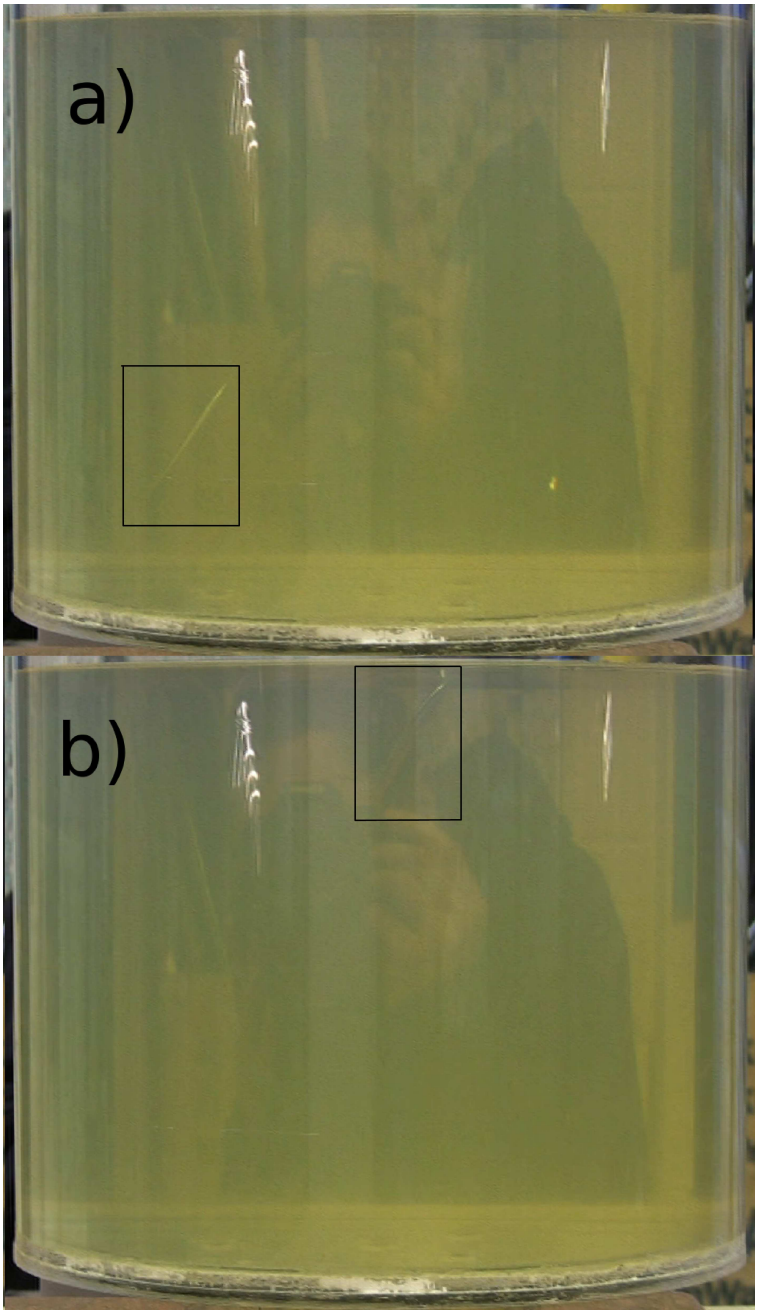

Figure 4.2: *CASE 0: Snapshots from the record of the first experiment in Table 4.1 (free surface). In panel (a) and (b) cross section views of the air-filled crack are shown. The snapshots was taken at the beginning of the experiment, few seconds after the air injection, and at the end of the experiment, with the crack upper tip very close to the free surface.*

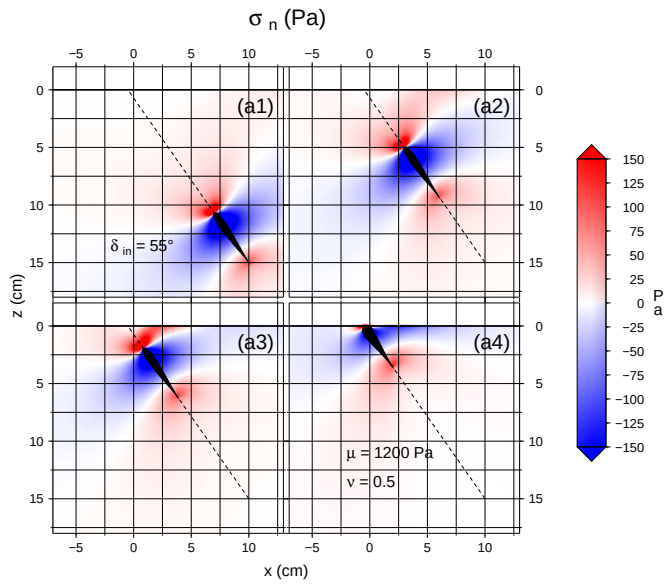

Figure 4.3: *Results of the mathematical simulation of gelatin experiment: CASE 0. We employed in the mathematical model a test angle* $\alpha = 2°$ *and an initial number of dislocation elements* $N = 88$.

With the temporal and spatial resolution of ours recording instruments we was not able to observe this deviation in the analogue experiment, also because of the crack acceleration very close to the free surface. Although the average dip angle for the boundary element crack results to be $55.3°$ in the "final" configuration. Considering this average dip angle from the mathematical model, experimental and numerical results agree within the experimental errors.

4.2 Experimental results: CASE I

We injected a volume $V_{in} = 10$ ml of air into a medium made up by a lower gelatin layer with rigidity $\mu_1 = 1.6 \pm 0.2$ KPa and an upper layer with rigidity $\mu_2 = 0.6 \pm 0.1$ KPa. The path of propagation is shown in Fig.4.4. Crack propagation is very slow and rectilinear, until the upper tip gets very close to the interface, where the dip sharply changes toward the vertical. The crack follows a 'refracted' trajectory as predicted in section 3.1.2. The incidence, dip angle is $\delta_{in} = (68 \pm 1)°$

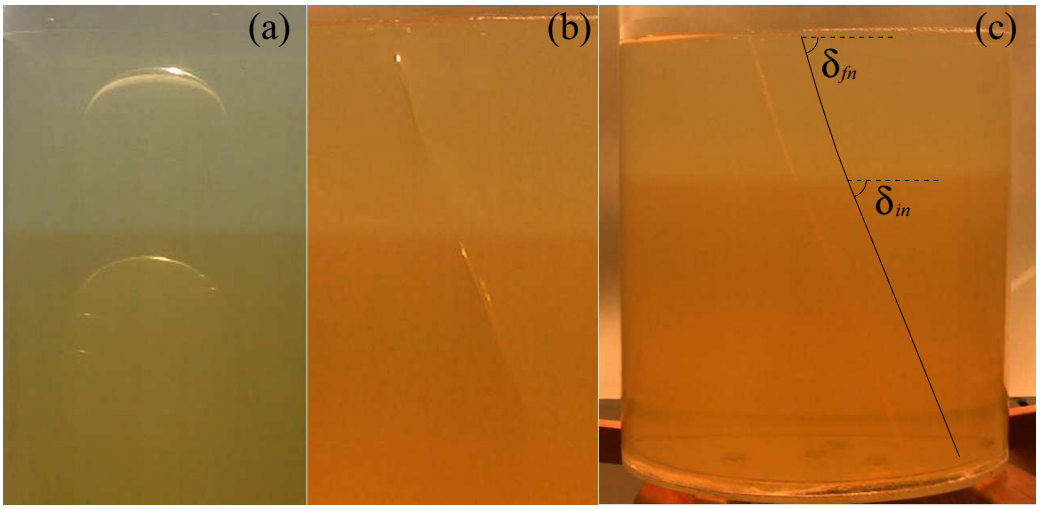

Figure 4.4: *CASE I: Snapshots from the record of the second experiment in Table 4.1 ($r = 0.37$). In panel (a) and (b) frontal and cross section views of the air-filled crack are shown: snapshots taken before and after the rigidity transition are superposed. In panel (c) the path followed by the crack is highlighted, after crack passage, by injection of red dye from the bottom of the fractured channel. Lines reproducing the crack path are shifted to the right with respect to the real crack.*

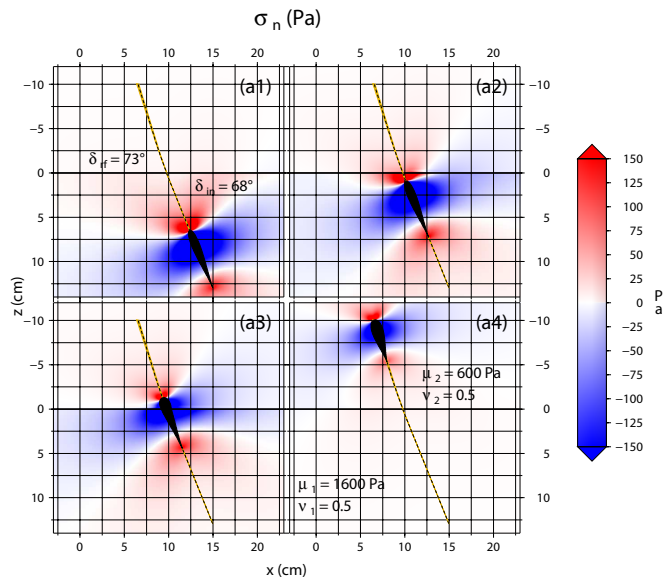

Figure 4.5: *Results of the mathematical simulation of gelatin experiment: CASE I. We employed in the mathematical model a test angle* $\alpha = 1.6°$ *and an initial number of dislocation elements* $N = 145$.

and the refraction angle is $\delta_{rf} = (72 \pm 1)°$. Shape and angles resulting from a correspondent run of the numerical code are shown in Fig.4.5, where a dashed line indicates the path obtained setting the fluid parameters according to Table 4.1 and the elastic parameters as reported in panel 4.5-a4. Paths uncertainties are obtained employing the upper and lower estimates of the r-value computed from measured gelatin rigidities (i.e. $r_{max} = \frac{\mu_2+\Delta\mu_2}{\mu_1-\Delta\mu_1}$ and $r_{min} = \frac{\mu_2-\Delta\mu_2}{\mu_1+\Delta\mu_1}$). In this case the path is very stable even perturbing the model parameters. Experimental and numerical results agree within the experimental errors.

4.3 Experimental results: CASE II

We injected a total volume $V_{in} = 8$ ml of air into a gelatin made up by a soft lower layer ($\mu_1 = 1.10 \pm 0.15$ KPa) and a more rigid upper layer ($\mu_2 = 1.9 \pm 0.2$ KPa). In this experiment the total volume V_{in} was injected in two steps: after an initial injection of 2 ml, sufficient for the propagation in the compliant medium, we

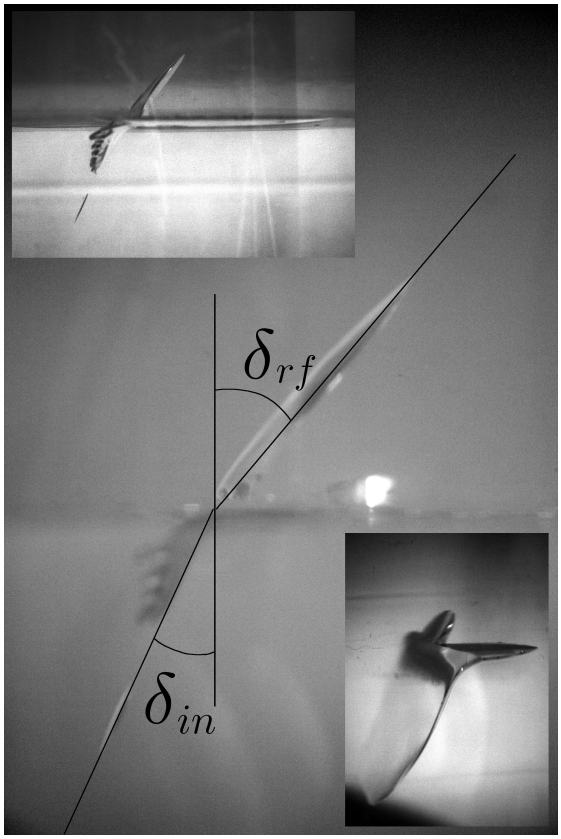

Figure 4.6: *CASE II: propagation of an air-filled crack from soft to rigid gelatin layers. The initial volume of the crack (2 ml) was not sufficient to propagate into the more rigid layer: the crack stopped at the interface. After a supplementary injection of 6 ml of air, the crack bifurcated along the interface (images in the insets) and into the stiffer medium, with a dip angle* δ_{rf}*. In the central image, a line is drawn to highlight the path followed by the crack propagating from the soft into the rigid layer.*

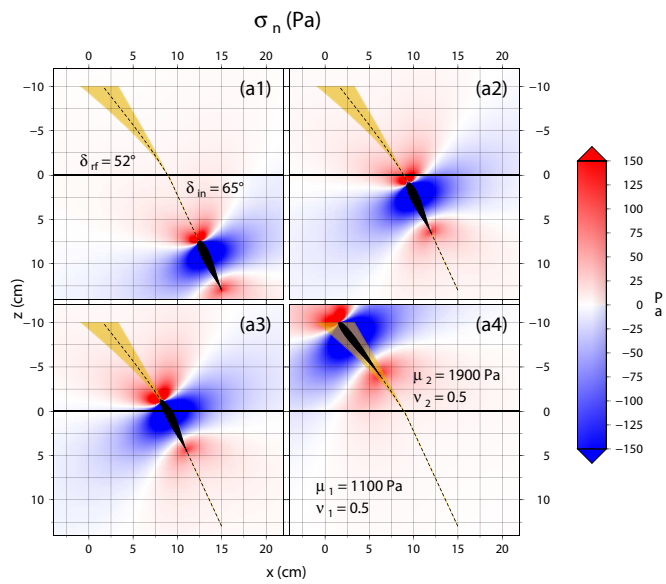

Figure 4.7: *Results of the mathematical simulation of gelatin experiment: CASE II. We employed in the mathematical model a test angle* $\alpha = 1°$ *and an initial number of dislocation elements* $N = 111$.

added 6 ml of air in order to obtain a sufficient total volume of the intrusion for the propagation in the stiffer layer (see Fig.4.6). Again, the crack follows a 'refracted' trajectory, as predicted in paragraph 3.1.4. The incidence, dip angle is $(65 \pm 1)°$ and the refraction angle is $(50 \pm 1)°$. In Fig.4.7 we report shape and angles resulting from a correspondent run of the numerical code. The dashed line indicates the path obtained setting the fluid parameters according to Table 4.1 and the elastic parameters as reported in panel 4.7-a4. The paths delimiting the wide orange area are obtained employing the upper and lower estimates of the r-value computed from measured gelatin rigidities (i.e. $r_{max} = \frac{\mu_2+\Delta\mu_2}{\mu_1-\Delta\mu_1}$ and $r_{min} = \frac{\mu_2-\Delta\mu_2}{\mu_1+\Delta\mu_1}$). In this case, perturbing the elastic parameters, we obtain a considerable variability in the refracted angle, according to the considerations exposed in section 3.1.4. Experimental and numerical results agree within errors. Unfortunately, we were not able to produce gelatin layers with rigidity contrasts lower than 0.37 so that the extreme cases of dike-to-sill conversions could not be observed.

Chapter 5

Discussion and conclusions

This work illustrates the relevance of elastic and density layering in the path of dikes and other fluid-filled fractures and demonstrates that the direction of propagation of fluid-filled cracks changes when they cross the interface between materials with different elastic properties. Explicit solutions from the mathematical model were shown taking into account elastic and density discontinuities and fracture toughness heterogeneities.
Results from numerical 2D boundary-element modelling and laboratory experiments on air injection in gelatin provide the same path deviation as a function of elastic parameters, density difference between host rock and fluid, mass and compressibility of the fluid.

5.1 Numerical model

The boundary-element code is based on 2D plane strain analytical solutions for a medium made of two welded half spaces with different elastic parameters. The dike trajectory is chosen among a range of possibilities according to energy minimisation. Mass is conserved during propagation, and the dike walls close at the lower tip while a new fracture is created at the top. Real dikes may lose or gain mass along their path. Since one focus on a limited region close to a layer interface, the assumption of mass conservation should not be restrictive.

This model does not account for fluid dynamics inside the dike nor for ther-

mal effects. Since it does not include the viscosity of the fluid, it cannot reveal any information related to velocity of propagation. Changes in viscous dissipation, possibly occurring when the dike crosses the interface, may affect the energy balance in a way that the present model cannot quantify.

The simulations show that gravitational energy has an important effect on the propagation path. Elastic parameters lead to increasing or decreasing crack opening and hence to shape changes. This modifies the position of the centre of gravity of the fluid batch and its potential gravitational energy. This interaction between elasticity and gravity had never been highlighted before.

The layer interface is modelled analytically. This allows us to retain many significant figures in the solution of the crack problem even when the crack is very close to or is crossing the interface. The difference in energy release for various directions of the test elements may be very similar but in the tested configurations this code can distinguish the preferred direction with sufficient accuracy. Numerical results are stable when the crack is discretised with more than $N = 40$ elements. As for the deviation angle α of the test dislocations, stable paths are found when α is $\sim 180°/N$. The uncertainty on the preferred propagation direction is in the order of the test angle used in the run.

5.2 Analogue experiments

Our numerical results on the propagation path agree qualitatively and quantitatively with the performed laboratory experiments. This supports the validity of the energetic criterion employed to predict the propagation direction of a slowly moving crack. In particular, this proves that the energy contributions important to predict dike path are the gravitational potential energy and the elastic strain energy. Although the energy loss due to viscous dissipation at crack tip or fluid motion within the crack has been shown to be important in constraining the propagation velocity (see Dahm, 2000b; Roper & Lister, 2005, 2007), the present numerical model predicts within errors the propagation path — at least for air-filled fractures slowly moving in gelatin.

The comparison between numerical models and analogue experiments allows us to validate the numerical model with experimental observations and vice-versa.

For instance, it has been shown experimentally that the crack lateral breadth w is nearly constant before and after crossing the interface (see Rivalta et al., 2005, Fig. 2), so that mass is conserved automatically when M_0/w is conserved. If w should vary significantly — e.g. while crossing the interface, when the frontal shape of the fracture is complicated — an additional correction should be introduced. The fact that the 2D mathematical model predicts incidence and refraction angles within errors demonstrates that 3D effects are small.

A free surface is present in the experiments and not in the layered numerical models — its effect was found to be important for the velocity change (Rivalta & Dahm, 2006) close to the free-surface itself. Numerical results shows (CASE 1b, sec. 3.1.3) the propagation direction is affected by the presence of the free surface only when the upper tip is closer to it than 1% of the fracture length. This makes us confident that the effects of a free surface are negligible when considering changes of propagation direction at the interface between different layers if the thickness of the upper layer is larger than dike length. Moreover, rigid lateral and bottom walls of the container provide boundary conditions of vanishing displacement which, in the numerical model, are imposed at infinity. In the anologue experiments, the interface crossing ever occurs near the centre of the container, in order to minimise undesired effects from its lateral surface.

Experimental conditions do not reproduce very large contrasts of elastic parameters. On one hand, this prevents us validating the numerical models where the contrast is $r \gtrsim 2$ or $r \lesssim 0.3$. On the other hand, moderate rigidity contrasts may be more representative of typical crustal values inferred from seismic soundings. However, in certain conditions, when the propagation is very slow, the temperature is high and the deformation is large, then anelastic processes are relevant which may provide much lower effective rigidity at depth than felt by seismic waves. Results of the numerical model for high rigidity contrast may apply to these conditions.

5.3 Implications for dike propagation in the crust

The illustrated refraction-like behaviour occurring as the crack crosses the interface between layers of different rigidities has various implications for magma

dikes in the mantle and crust.

Dikes inclined with respect to the vertical are expected to develop at depth, close to a magma chamber, due to the tensional stress field provided by chamber inflation: for instance, maximum tensional axes around a spherical inflating source are perpendicular to the radial direction so that dikes can be generated at any angle. Furthermore, oblique dikes form if magma ascends through weakness planes, such as the ring faults usually present within volcanic calderas (e.g. Burchardt, 2008; Gudmundsson & Brenner, 2005).

If a dike always meets transitions from more rigid to more compliant layers, its path is predicted to gradually approach the vertical direction. The deviatoric stress field of tectonic origin (which is ignored in the present paper) is considered to be responsible for the nearly vertical dip often observed for real dikes, but the refraction phenomenon described above may be important, as well.

In any case, observations of strongly inclined dikes are frequent (e.g. Burchardt, 2008) and inclined dikes are often inferred from inversion of deformation data (e.g. Froger et al., 2004; Sigmundsson et al., 1999) and from seismic data (e.g. Chouet et al., 2003).

On the other hand, transition from compliant to stiff rocks is often found when competent lava beds are superposed onto pyroclastic deposits. In such cases our model predicts dike deflection toward the horizontal or even sill formation, as found in the field by Burchardt (2008); Gudmundsson & Brenner (2005). A striking example of such a behaviour is shown in Figure 5.1. Similar results are found by Kavanagh et al. (2006) with gelatin experiments.

Moderate rigidity contrasts may be more representative of typical crustal values inferred from seismic soundings. However, in certain conditions -when the propagation is very slow, the temperature is high and the deformation is large - then anelastic processes are relevant which may provide much lower effective rigidity at depth than inferred by seismic waves. A slow dike, feeling an effective long-term rigidity rather than a short-term one, would effectively see the mantle-crust boundary (or any boundary between a viscoelastic and an elastic medium) as a transition toward a more rigid medium, hence tending to deflect toward the horizontal. As mentioned in the introduction, recent geophysical studies on the topography of the Moho at continental rift zones have evidenced the presence of

Figure 5.1: *A dike deflected toward the horizontal when approaching a stiffer layer. The picture was taken by Prof. Michael S. Ramsey, University of Pittsburgh, in the Colorado River Grand Canyon, Arizona. The dike is basalt and intrudes diagonally into the Hakatai Shale (the red host rock); the stiffer rock above the dike is Shinumo Quartzite. Typical rigidity values for these rocks yield a ratio* $r = \mu_2/\mu_1 \sim 6$.

stacked sills from low to mid crustal depths (see Thybo & Nielsen, 2009; White et al., 2008). Smith et al. (2004) evidenced a 50° dipping magma body at about 30 km depth in the Lake Tahoe area, where it stopped after propagating a few km, as inferred from migration of induced seismicity. According to our model, this may be explained in terms of magma meeting a rheological discontinuity.

An important role for sill formation may be played by density stratification: preliminary tests adding to the model a density contrast superposed to the rigidity transition, have shown that, as far as the dike density is lower than both layers, the influence of density layering can change slightly the deviation due to the elastic discontinuity but cannot be the only responsible for this phenomenon. If the fluid density is higher than in the upper medium, the dike stops soon after reaching the neutral buoyancy level (as already suggested by Lister & Kerr (1991)).

Further investigations considering the local and tectonic stress field are necessary in order to establish quantitatively what implications tectonic stretching may have on sill formation and, more generally, on the propagation path in proximity of elastic discontinuities, since sharp stress heterogeneities typically arise from rigidity discontinuities.

The model might be also generalised to account for viscous energy loss, provided by fluid motions and continuous magma supply from a deep source.

The evidence for the refraction behaviour in gelatin experiments (see Fig. 6b in Kavanagh et al., 2006, for an additional example of refraction from a compliant to a more rigid medium) seems to be less readily available in field observations. However, most observations on dikes are limited to the upper crust, where most dikes arrive already vertical, so that they would not be deviated as they cross a rigidity transition; moreover, if layers near the surface are thin and rigidity contrasts alternate (for example a set of $r < 1$ and $r > 1$ transitions), dikes would see an average effective rigidity. Therefore, a field validation of our findings may be possible in case of deep erosion of thick layers with high rigidity contrast.

5.3.1 Future work

A development of this model should be aimed at the study of dike propagation under the effect of topographic load and tectonic stress field, since sharp stress

heterogeneities typically arise from rigidity discontinuities.
Studies of dike-dike and sill-dike interaction should be an other application of this model that could be developed also to account for an interacting magma-chamber providing a certain magma supply.
The model should be applied also to the study of the seismicity induced by dike propagation, using a more realistic model for the Coulomb failure function. The model might be also generalised to account for viscous energy loss, provided by fluid motions and continuous magma supply from a deep source.

Appendix A

In appendix A we write the functions $g_x(x, z; x_1, z_1)$, $g_z(x, z; x_1, z_1)$, $h_x(x, z; x_1, z_1)$ and $h_z(x, z; x_1, z_1)$, that appears in equations (2.10) and (2.11), relative to the displacement field generated by a vertically dipping, semi-infinite, elementary dislocation in a bounded medium.
For a tensile dislocation (eq. 2.10), the *loading function* relative to the x component of the displacement is:

$$\begin{cases} g_x(x, z > 0; x_1, z_1 > 0) = \dfrac{1}{2\pi}\left[\Phi(x, z; x_1, z_1) + \dfrac{1}{2(1-\nu_1)}\dfrac{(x-x_1)(z-z_1)}{r^2}\right] - \displaystyle\sum_{j=1}^{4} U^I_{1j}\, Y_{1j} \\ g_x(x, z < 0; x_1, z_1 > 0) = \dfrac{1}{2\pi}\left[\Phi(x, z; x_1, z_1) + \dfrac{1}{2(1-\nu_2)}\dfrac{(x-x_1)(z-z_1)}{r^2}\right] - \displaystyle\sum_{j=1}^{4} U^I_{2j}\, Y_{2j} \\ g_x(x, z > 0; x_1, z_1 < 0) = \dfrac{1}{2\pi}\left[\Phi(x, z; x_1, z_1) + \dfrac{1}{2(1-\nu_1)}\dfrac{(x-x_1)(z-z_1)}{r^2}\right] - \displaystyle\sum_{j=1}^{4} U^{II}_{2j}\, Y_{2j} \\ g_x(x, z < 0; x_1, z_1 < 0) = \dfrac{1}{2\pi}\left[\Phi(x, z; x_1, z_1) + \dfrac{1}{2(1-\nu_2)}\dfrac{(x-x_1)(z-z_1)}{r^2}\right] - \displaystyle\sum_{j=1}^{4} U^{II}_{1j}\, Y_{1j} \end{cases} \tag{A.1}$$

where $r = \sqrt{(x-x_1)^2 + (z-z_1)^2}$ is the distance between the dislocation line and the point (x, z), Φ is the function 2.4 translated of a vector (x_1, z_1) and matrix U^I, U^{II} and Y are written respectively in (A.5), (A.6) and (A.12).
For the z component we have:

$$\begin{cases} g_z(x, z > 0; x_1, z_1 > 0) = -\dfrac{1}{4\pi(1-\nu_1)}\left[(1-2\nu_1)\ln\dfrac{r}{2c} - \dfrac{(z-z_1)^2}{r^2}\right] - \displaystyle\sum_{j=1}^{4} U^I_{3j}\, Y_{3j} \\ g_z(x, z < 0; x_1, z_1 > 0) = -\dfrac{1}{4\pi(1-\nu_2)}\left[(1-2\nu_2)\ln\dfrac{r}{2c} - \dfrac{(z-z_1)^2}{r^2}\right] - \displaystyle\sum_{j=1}^{4} U^I_{4j}\, Y_{4j} \\ g_z(x, z > 0; x_1, z_1 < 0) = -\dfrac{1}{4\pi(1-\nu_1)}\left[(1-2\nu_1)\ln\dfrac{r}{2c} - \dfrac{(z-z_1)^2}{r^2}\right] - \displaystyle\sum_{j=1}^{4} U^{II}_{4j}\, Y_{4j} \\ g_z(x, z < 0; x_1, z_1 < 0) = -\dfrac{1}{4\pi(1-\nu_2)}\left[(1-2\nu_2)\ln\dfrac{r}{2c} - \dfrac{(z-z_1)^2}{r^2}\right] - \displaystyle\sum_{j=1}^{4} U^{II}_{3j}\, Y_{3j} \end{cases} \tag{A.2}$$

where c is needed to make non-dimensional the argument of the logarithm and, for a closed dislocation, is its half-length.

For a dip-slip dislocation (eq. 2.11), the loading function relative to the x component of the displacement is:

$$\begin{cases} h_x(x, z > 0; x_1, z_1 > 0) = \dfrac{1}{4\pi(1-\nu_1)}\left[(1-2\nu_1)\ln\dfrac{r}{2c} + \dfrac{(z-z_1)^2}{r^2}\right] - \displaystyle\sum_{j=1}^{4} T^I_{3j}\, Y_{3j} \\ h_x(x, z < 0; x_1, z_1 > 0) = \dfrac{1}{4\pi(1-\nu_2)}\left[(1-2\nu_2)\ln\dfrac{r}{2c} + \dfrac{(z-z_1)^2}{r^2}\right] - \displaystyle\sum_{j=1}^{4} T^I_{4j}\, Y_{4j} \\ h_x(x, z > 0; x_1, z_1 < 0) = \dfrac{1}{4\pi(1-\nu_1)}\left[(1-2\nu_1)\ln\dfrac{r}{2c} + \dfrac{(z-z_1)^2}{r^2}\right] - \displaystyle\sum_{j=1}^{4} T^{II}_{4j}\, Y_{4j} \\ h_x(x, z < 0; x_1, z_1 < 0) = \dfrac{1}{4\pi(1-\nu_2)}\left[(1-2\nu_2)\ln\dfrac{r}{2c} + \dfrac{(z-z_1)^2}{r^2}\right] - \displaystyle\sum_{j=1}^{4} T^{II}_{3j}\, Y_{3j} \end{cases} \tag{A.3}$$

where the matrix T^I and T^{II} are written in A.9 and A.10.

For the z component we have:

$$\begin{cases} h_z(x, z>0; x_1, z_1>0) = \dfrac{1}{2\pi}\left[\Phi(x,z;x_1,z_1) - \dfrac{1}{2(1-\nu_1)}\dfrac{(x-x_1)(z-z_1)}{r^2}\right] - \displaystyle\sum_{j=1}^{4} T_{1j}^{I}\, Y_{1j} \\ h_z(x, z<0; x_1, z_1>0) = \dfrac{1}{2\pi}\left[\Phi(x,z;x_1,z_1) - \dfrac{1}{2(1-\nu_2)}\dfrac{(x-x_1)(z-z_1)}{r^2}\right] - \displaystyle\sum_{j=1}^{4} T_{2j}^{I}\, Y_{2j} \\ h_z(x, z>0; x_1, z_1<0) = \dfrac{1}{2\pi}\left[\Phi(x,z;x_1,z_1) - \dfrac{1}{2(1-\nu_1)}\dfrac{(x-x_1)(z-z_1)}{r^2}\right] - \displaystyle\sum_{j=1}^{4} T_{2j}^{II}\, Y_{2j} \\ h_z(x, z<0; x_1, z_1<0) = \dfrac{1}{2\pi}\left[\Phi(x,z;x_1,z_1) - \dfrac{1}{2(1-\nu_2)}\dfrac{(x-x_1)(z-z_1)}{r^2}\right] - \displaystyle\sum_{j=1}^{4} T_{1j}^{II}\, Y_{1j} \end{cases} \tag{A.4}$$

The matrix U^I and U^{II} are:

$$U^I = \begin{pmatrix} -\dfrac{1-\nu_1}{\mu_1}C_2 + \dfrac{1-2\nu_1}{2\mu_1}D & \dfrac{1}{2\mu_1}(C_2-D) & \dfrac{3-4\nu_1}{2\mu_1}(C_2-D) & -\dfrac{1}{\mu_1}(C_2-D) \\ -\dfrac{1-\nu_2}{\mu_2}C_1 + \dfrac{1-2\nu_2}{2\mu_2}D & \dfrac{1}{2\mu_2}(C_1+D) & -\dfrac{1}{2\mu_2}(C_1-D) & 0 \\ \dfrac{1-\nu_1}{\mu_1}D - \dfrac{1-2\nu_1}{2\mu_1}C_2 & -\dfrac{1}{2\mu_1}(C_2-D) & \dfrac{3-4\nu_1}{2\mu_1}(C_2-D) & \dfrac{1}{\mu_1}(C_2-D) \\ \dfrac{1-\nu_2}{\mu_2}D - \dfrac{1-2\nu_2}{2\mu_2}C_1 & \dfrac{1}{2\mu_2}(C_1+D) & -\dfrac{1}{2\mu_2}(C_1-D) & 0 \end{pmatrix} \tag{A.5}$$

$$U^{II} = \begin{pmatrix} -\dfrac{1-\nu_2}{\mu_2}C_1 - \dfrac{1-2\nu_2}{2\mu_2}D & \dfrac{1}{2\mu_2}(C_1+D) & \dfrac{3-4\nu_2}{2\mu_2}(C_1+D) & -\dfrac{1}{\mu_2}(C_1+D) \\ -\dfrac{1-\nu_1}{\mu_1}C_2 - \dfrac{1-2\nu_1}{2\mu_1}D & \dfrac{1}{2\mu_1}(C_2-D) & -\dfrac{1}{2\mu_1}(C_2+D) & 0 \\ -\dfrac{1-\nu_2}{\mu_2}D - \dfrac{1-2\nu_2}{2\mu_2}C_1 & -\dfrac{1}{2\mu_2}(C_1+D) & \dfrac{3-4\nu_2}{2\mu_2}(C_1+D) & \dfrac{1}{\mu_2}(C_1+D) \\ -\dfrac{1-\nu_1}{\mu_1}D - \dfrac{1-2\nu_1}{2\mu_1}C_2 & \dfrac{1}{2\mu_1}(C_2-D) & -\dfrac{1}{2\mu_1}(C_2+D) & 0 \end{pmatrix} \tag{A.6}$$

where C_1, C_2 and D are:

$$C_1 = \frac{\delta(a_1 + c_p) + \gamma d}{e^2 - d^2} \quad C_2 = \frac{-\delta(a_2 + c_p) + \gamma d}{e^2 - d^2} \quad D = \frac{\delta c_m - \gamma e}{e^2 - d^2} \tag{A.7}$$

with:

$$\begin{aligned}
&a_1 = \frac{3 - 4\nu_1}{4\mu_1^2}; && a_2 = \frac{3 - 4\nu_2}{2\mu_2^2}; \\
&d = \frac{1 - 2\nu_2}{2\mu_2} - \frac{1 - 2\nu_1}{2\mu_1}; && e = \frac{1 - \nu_2}{\mu_2} - \frac{1 - \nu_1}{\mu_1}; \\
&c_p = \frac{1 + (3 - 4\nu_1)(3 - 4\nu 2)}{8\mu_1\mu_2}; && c_m = -\frac{1 + (3 - 4\nu_1)(3 - 4\nu 2)}{8\mu_1\mu_2}; \\
&\delta_1 = \frac{1}{2\pi}\frac{\mu_1}{1 - \nu_1}; && \delta_2 = \frac{1}{2\pi}\frac{\mu_2}{1 - \nu_2}; \qquad \delta = \delta_2 - \delta_1; \\
&\gamma_1 = \frac{1}{4\pi}\frac{1}{1 - \nu_1}; && \gamma_2 = \frac{1}{4\pi}\frac{1}{1 - \nu_2}; \qquad \gamma = \gamma_2 - \gamma_1.
\end{aligned} \tag{A.8}$$

The matrix T^I and T^{II} are:

$$T^I = \begin{pmatrix} \mu_1\kappa_1 - \mu_2\kappa_2 & \gamma_1 - 2\mu_2\kappa_1 & -\gamma_1 - 2\mu_1\kappa_1 & 2(\gamma_1 - 2\mu_2\kappa_1) \\ \mu_1\kappa_1 - \mu_2\kappa_2 & \gamma_2 - 2\mu_1\kappa_2 & -\gamma_2 - 2\mu_1\kappa_1 & 0 \\ \gamma_1 - \mu_1\kappa_1 - \mu_2\kappa_2 & \gamma_1 - 2\mu_2\kappa_1 & \gamma_1 - 2\mu_1\kappa_1 & 2(\gamma_1 - 2\mu_2\kappa_1) \\ \gamma_2 - \mu_1\kappa_1 - \mu_2\kappa_2 & -\gamma_2 + 2\mu_1\kappa_2 & \gamma_2 - 2\mu_1\kappa_1 & 0 \end{pmatrix} \tag{A.9}$$

$$T^{II} = \begin{pmatrix} -\mu_1\kappa_1 + \mu_2\kappa_2 & \gamma_2 - 2\mu_1\kappa_2 & -\gamma_2 + 2\mu_2\kappa_2 & 2(\gamma_2 - 2\mu_1\kappa_2) \\ -\mu_1\kappa_1 + \mu_2\kappa_2 & \gamma_1 - 2\mu_2\kappa_1 & -\gamma_1 + 2\mu_2\kappa_2 & 0 \\ \gamma_2 - \mu_1\kappa_1 - \mu_2\kappa_2 & \gamma_2 - 2\mu_1\kappa_2 & \gamma_2 - 2\mu_2\kappa_2 & 2(\gamma_2 - 2\mu_1\kappa_2) \\ \gamma_1 - \mu_1\kappa_1 - \mu_2\kappa_2 & -\gamma_1 + 2\mu_2\kappa_1 & \gamma_1 - 2\mu_2\kappa_2 & 0 \end{pmatrix} \tag{A.10}$$

where κ_1 and κ_2 are:

$$\kappa_1 = \frac{1}{2\pi}\frac{1}{\mu_1 + (3 - 4\nu_1)\mu_2} \quad \kappa_2 = \frac{1}{2\pi}\frac{1}{\mu_2 + (3 - 4\nu_2)\mu_1} \tag{A.11}$$

The matrix Y is:

$$\begin{cases} Y_{11} &= \dfrac{\pi}{2}\mathrm{sgn}\left[(z_1+z)(x-x_1)\right] \\ & \quad -\arctan\left(\dfrac{z_1+z}{x-x_1}\right) \\ Y_{12} &= \dfrac{z(x-x_1)}{(x-x_1)^2+(z+z_1)^2} \\ Y_{13} &= \dfrac{z_1(x-x_1)}{(x-x_1)^2+(z+z_1)^2} \\ Y_{14} &= \dfrac{2zz_1(x-x_1)(z_1+z)}{\left[(x-x_1)^2+(z+z_1)^2\right]^2} \end{cases} \qquad \begin{cases} Y_{21} &= \dfrac{\pi}{2}\mathrm{sgn}\left[(z_1-z)(x-x_1)\right] \\ & \quad -\arctan\left(\dfrac{z_1-z}{x-x_1}\right) \\ Y_{22} &= \dfrac{z(x-x_1)}{(x-x_1)^2+(z-z_1)^2} \\ Y_{23} &= \dfrac{z_1(x-x_1)}{(x-x_1)^2+(z-z_1)^2} \\ Y_{24} &= \dfrac{2zz_1(x-x_1)(z_1-z)}{\left[(x-x_1)^2+(z-z_1)^2\right]^2} \end{cases} \tag{A.12}$$

$$\begin{cases} Y_{31} &= \dfrac{1}{2}\ln\dfrac{(x-x_1)^2+(z+z_1)^2}{(2c)^2} \\ Y_{32} &= -\dfrac{z(z+z_1)}{(x-x_1)^2+(z+z_1)^2} \\ Y_{33} &= -\dfrac{z_1(z+z_1)}{(x-x_1)^2+(z+z_1)^2} \\ Y_{34} &= \dfrac{zz_1\left[(x-x_1)^2-(z_1+z)^2\right]}{\left[(x-x_1)^2+(z+z_1)^2\right]^2} \end{cases} \qquad \begin{cases} Y_{41} &= \dfrac{1}{2}\ln\dfrac{(x-x_1)^2+(z-z_1)^2}{(2c)^2} \\ Y_{42} &= -\dfrac{z(z-z_1)}{(x-x_1)^2+(z-z_1)^2} \\ Y_{43} &= -\dfrac{z_1(z-z_1)}{(x-x_1)^2+(z-z_1)^2} \\ Y_{44} &= \dfrac{zz_1\left[(x-x_1)^2-(z_1-z)^2\right]}{\left[(x-x_1)^2+(z-z_1)^2\right]^2} \end{cases}$$

Appendix B

In appendix B we write the functions $s_{ij}^{(x)}(x,z;x_1,z_1)$ and $s_{ij}^{(z)}(x,z;x_1,z_1)$, that appears in equations (2.15), relative to the stress field generated by a vertically dipping, semi-infinite, elementary dislocation in a bounded medium.

For a tensile dislocation (first equation in 2.15), the *loading function* relative to the (xx) component of the stress tensor is:

$$\begin{cases} s_{xx}^{(x)}(x,z>0;x_1,z_1>0) &= -\dfrac{\mu_1}{2\pi(1-\nu_1)}\cdot\dfrac{(z-z_1)[3(x-x_1)^2+(z-z_1)^2]}{r^4}+ \\ & +(2C_2-D)I_{11}-(C_2-D)I_{12}-3(C_2-D)I_{13}+2(C_2-D)I_{14} \\ s_{xx}^{(x)}(x,z<0;x_1,z_1>0) &= -\dfrac{\mu_2}{2\pi(1-\nu_2)}\cdot\dfrac{(z-z_1)[3(x-x_1)^2+(z-z_1)^2]}{r^4}+ \\ & -(2C_1+D)I_{21}-(C_1+D)I_{22}+(C_1-D)I_{23} \\ s_{xx}^{(x)}(x,z>0;x_1,z_1<0) &= -\dfrac{\mu_1}{2\pi(1-\nu_1)}\cdot\dfrac{(z-z_1)[3(x-x_1)^2+(z-z_1)^2]}{r^4}+ \\ & -(2C_2-D)I_{21}-(C_2-D)I_{22}+(C_2+D)I_{23} \\ s_{xx}^{(x)}(x,z<0;x_1,z_1<0) &= -\dfrac{\mu_2}{2\pi(1-\nu_2)}\cdot\dfrac{(z-z_1)[3(x-x_1)^2+(z-z_1)^2]}{r^4}+ \\ & +(2C_1+D)I_{11}-(C_1+D)I_{12}-3(C_1+D)I_{13}+2(C_1+D)I_{14} \end{cases} \tag{B.1}$$

where $r = \sqrt{(x-x_1)^2 + (z-z_1)^2}$ is the distance between the dislocation line and the point (x, z), C_1, C_2 and D are written in (A.7), I is written in (refB:11).
For the (xz) component we have:

$$\begin{cases} s_{xz}^{(x)}(x, z > 0; x_1, z_1 > 0) = -\dfrac{\mu_1}{2\pi(1-\nu_1)} \cdot \dfrac{(x-x_1)[(z-z_1)^2 - (x-x_1)^2]}{r^4} - \displaystyle\sum_{j=1}^{4} G_{3j}^{I}\, I_{3j} \\ s_{xz}^{(x)}(x, z < 0; x_1, z_1 > 0) = -\dfrac{\mu_2}{2\pi(1-\nu_2)} \cdot \dfrac{(x-x_1)[(z-z_1)^2 - (x-x_1)^2]}{r^4} - \displaystyle\sum_{j=1}^{4} G_{4j}^{I}\, I_{4j} \\ s_{xz}^{(x)}(x, z > 0; x_1, z_1 < 0) = -\dfrac{\mu_1}{2\pi(1-\nu_1)} \cdot \dfrac{(x-x_1)[(z-z_1)^2 - (x-x_1)^2]}{r^4} - \displaystyle\sum_{j=1}^{4} G_{4j}^{II}\, I_{4j} \\ s_{xz}^{(x)}(x, z < 0; x_1, z_1 < 0) = -\dfrac{\mu_2}{2\pi(1-\nu_2)} \cdot \dfrac{(x-x_1)[(z-z_1)^2 - (x-x_1)^2]}{r^4} - \displaystyle\sum_{j=1}^{4} G_{3j}^{II}\, I_{3j} \end{cases} \tag{B.2}$$

where G^I and G^{II} are written in (B.7) and (B.8).
For the (zz) component we have:

$$\begin{cases} s_{zz}^{(x)}(x, z > 0; x_1, z_1 > 0) = -\dfrac{\mu_1}{2\pi(1-\nu_1)} \cdot \dfrac{(z-z_1)[(z-z_1)^2 - (x-x_1)^2]}{r^4} - \displaystyle\sum_{j=1}^{4} G_{1j}^{I}\, I_{1j} \\ s_{zz}^{(x)}(x, z < 0; x_1, z_1 > 0) = -\dfrac{\mu_1}{2\pi(1-\nu_1)} \cdot \dfrac{(z-z_1)[(z-z_1)^2 - (x-x_1)^2]}{r^4} - \displaystyle\sum_{j=1}^{4} G_{2j}^{I}\, I_{2j} \\ s_{zz}^{(x)}(x, z > 0; x_1, z_1 < 0) = -\dfrac{\mu_1}{2\pi(1-\nu_1)} \cdot \dfrac{(z-z_1)[(z-z_1)^2 - (x-x_1)^2]}{r^4} - \displaystyle\sum_{j=1}^{4} G_{2j}^{II}\, I_{2j} \\ s_{zz}^{(x)}(x, z < 0; x_1, z_1 < 0) = -\dfrac{\mu_1}{2\pi(1-\nu_1)} \cdot \dfrac{(z-z_1)[(z-z_1)^2 - (x-x_1)^2]}{r^4} - \displaystyle\sum_{j=1}^{4} G_{1j}^{II}\, I_{1j} \end{cases} \tag{B.3}$$

For a dip-slip dislocation (second equation in 2.15), the loading function relative to the (xx) component of the displacement is:

$$
\begin{cases}
s_{xx}^{(z)}(x, z > 0; x_1, z_1 > 0) = -\dfrac{\mu_1}{2\pi(1-\nu_1)} \cdot \dfrac{(x-x_1)[(z-z_1)^2 - (x-x_1)^2]}{r^4} + \\
\qquad -(C_2 - 2D)I_{31} + (C_2 - D)I_{32} - 3(C_2 - D)I_{33} + 2(C_2 - D)I_{34} \\
s_{xx}^{(z)}(x, z < 0; x_1, z_1 > 0) = -\dfrac{\mu_1}{2\pi(1-\nu_1)} \cdot \dfrac{(x-x_1)[(z-z_1)^2 - (x-x_1)^2]}{r^4} + \\
\qquad -(C_1 + 2D)I_{41} - (C_1 + D)I_{42} + (C_1 - D)I_{43} \\
s_{xx}^{(z)}(x, z > 0; x_1, z_1 < 0) = -\dfrac{\mu_1}{2\pi(1-\nu_1)} \cdot \dfrac{(x-x_1)[(z-z_1)^2 - (x-x_1)^2]}{r^4} + \\
\qquad -(C_2 - 2D)I_{41} - (C_2 - D)I_{42} + (C_2 + D)I_{43} \\
s_{xx}^{(z)}(x, z < 0; x_1, z_1 < 0) = -\dfrac{\mu_1}{2\pi(1-\nu_1)} \cdot \dfrac{(x-x_1)[(z-z_1)^2 - (x-x_1)^2]}{r^4} + \\
\qquad -(C_1 - 2D)I_{31} + (C_1 + D)I_{32} - 3(C_1 + D)I_{33} + 2(C_1 + D)I_{34}
\end{cases}
\tag{B.4}
$$

For the (xz) component we have:

$$\begin{cases} s_{xz}^{(z)}(x, z > 0; x_1, z_1 > 0) = -\dfrac{\mu_1}{2\pi(1-\nu_1)} \cdot \dfrac{(z-z_1)[(z-z_1)^2 - (x-x_1)^2]}{r^4} + \displaystyle\sum_{j=1}^{4} F_{1j}^{I}\, I_{1j} \\ s_{xz}^{(z)}(x, z < 0; x_1, z_1 > 0) = -\dfrac{\mu_1}{2\pi(1-\nu_1)} \cdot \dfrac{(z-z_1)[(z-z_1)^2 - (x-x_1)^2]}{r^4} + \displaystyle\sum_{j=1}^{4} F_{2j}^{I}\, I_{2j} \\ s_{xz}^{(z)}(x, z > 0; x_1, z_1 < 0) = -\dfrac{\mu_1}{2\pi(1-\nu_1)} \cdot \dfrac{(z-z_1)[(z-z_1)^2 - (x-x_1)^2]}{r^4} + \displaystyle\sum_{j=1}^{4} F_{2j}^{II}\, I_{2j} \\ s_{xz}^{(z)}(x, z < 0; x_1, z_1 < 0) = -\dfrac{\mu_1}{2\pi(1-\nu_1)} \cdot \dfrac{(z-z_1)[(z-z_1)^2 - (x-x_1)^2]}{r^4} + \displaystyle\sum_{j=1}^{4} F_{1j}^{II}\, I_{1j} \end{cases} \tag{B.5}$$

where F^I and F^{II} are written in B.9 and B.10.

For the zz component we have:

$$\begin{cases} s_{zz}^{(z)}(x, z > 0; x_1, z_1 > 0) = \dfrac{\mu_1}{2\pi(1-\nu_1)} \cdot \dfrac{(x-x_1)[(x-x_1)^2 + 3(z-z_1)^2]}{r^4} + \displaystyle\sum_{j=1}^{4} F_{3j}^{I}\, I_{3j} \\ s_{zz}^{(z)}(x, z < 0; x_1, z_1 > 0) = \dfrac{\mu_1}{2\pi(1-\nu_1)} \cdot \dfrac{(x-x_1)[(x-x_1)^2 + 3(z-z_1)^2]}{r^4} + \displaystyle\sum_{j=1}^{4} F_{4j}^{I}\, I_{4j} \\ s_{zz}^{(z)}(x, z > 0; x_1, z_1 < 0) = \dfrac{\mu_1}{2\pi(1-\nu_1)} \cdot \dfrac{(x-x_1)[(x-x_1)^2 + 3(z-z_1)^2]}{r^4} + \displaystyle\sum_{j=1}^{4} F_{4j}^{II}\, I_{4j} \\ s_{zz}^{(z)}(x, z < 0; x_1, z_1 < 0) = \dfrac{\mu_1}{2\pi(1-\nu_1)} \cdot \dfrac{(x-x_1)[(x-x_1)^2 + 3(z-z_1)^2]}{r^4} + \displaystyle\sum_{j=1}^{4} F_{3j}^{II}\, I_{3j} \end{cases} \tag{B.6}$$

The matrix G^I and G^{II} are:

$$G^I = \begin{pmatrix} D & -(C_2 - D) & C_2 - D & 2(C_2 - D) \\ D & -(C_1 + D) & C_1 - D & 0 \\ C_2 & -(C_2 - D) & -(C_2 - D) & 2(C_2 - D) \\ C_1 & C_1 + D & -(C_1 - D) & 0 \end{pmatrix} \tag{B.7}$$

$$G^{II} = \begin{pmatrix} -D & -(C_1 + D) & C_1 + D & 2(C_1 + D) \\ -D & -(C_2 - D) & C_2 + D & 0 \\ C_1 & -(C_1 + D) & -(C_1 + D) & 2(C_1 + D) \\ C_2 & C_2 - D & -(C_2 + D) & 0 \end{pmatrix} \tag{B.8}$$

The matrix F^I and F^{II} are:

$$F^I = \begin{pmatrix} D & C_2 - D & -(C_2 - D) & 2(C_2 - D) \\ D & C_1 + D & -(C_1 - D) & 0 \\ -C_2 & -(C_2 - D) & -(C_2 - D) & -2(C_2 - D) \\ -C_1 & C_1 + D & -(C_1 - D) & 0 \end{pmatrix} \tag{B.9}$$

$$F^{II} = \begin{pmatrix} -D & C_1 + D & -(C_1 + D) & 2(C_1 + D) \\ -D & C_2 - D & -(C_2 + D) & 0 \\ -C_1 & -(C_1 + D) & -(C_1 + D) & -2(C_1 + D) \\ -C_2 & C_2 - D & -(C_2 + D) & 0 \end{pmatrix} \tag{B.10}$$

The matrix I is:

$$\begin{cases} I_{11} = \dfrac{z + z_0}{(x - x_0)^2 + (z + z_0)^2} \\ I_{12} = z\dfrac{(z + z_0)^2 - (x - x_0)^2}{[(x - x_0)^2 + (z + z_0)^2]^2} \\ I_{13} = z_0\dfrac{(z + z_0)^2 - (x - x_0)^2}{[(x - x_0)^2 + (z + z_0)^2]^2} \\ I_{14} = 2zz_0\dfrac{(z + z_0)[(z + z_0)^2 - 3(x - x_0)^2]}{[(x - x_0)^2 + (z + z_0)^2]^3} \end{cases} \quad \begin{cases} I_{21} = \dfrac{z - z_0}{(x - x_0)^2 + (z - z_0)^2} \\ I_{22} = z\dfrac{(z - z_0)^2 - (x - x_0)^2}{[(x - x_0)^2 + (z - z_0)^2]^2} \\ I_{23} = z_0\dfrac{(z - z_0)^2 - (x - x_0)^2}{[(x - x_0)^2 + (z - z_0)^2]^2} \\ I_{24} = 2zz_0\dfrac{(z - z_0)[(z - z_0)^2 - 3(x - x_0)^2]}{[(x - x_0)^2 + (z - z_0)^2]^3} \end{cases}$$

$$\begin{cases} I_{31} = \dfrac{x - x_0}{(x - x_0)^2 + (z + z_0)^2} \\ I_{32} = 2z\dfrac{(z + z_0)(x - x_0)}{[(x - x_0)^2 + (z + z_0)^2]^2} \\ I_{33} = 2z_0\dfrac{(z + z_0)(x - x_0)}{[(x - x_0)^2 + (z + z_0)^2]^2} \\ I_{34} = 2zz_0\dfrac{(x - x_0)[3(z + z_0)^2 - (x - x_0)^2]}{[(x - x_0)^2 + (z + z_0)^2]^3} \end{cases} \quad \begin{cases} I_{41} = \dfrac{x - x_0}{(x - x_0)^2 + (z - z_0)^2} \\ I_{42} = 2z\dfrac{(z - z_0)(x - x_0)}{[(x - x_0)^2 + (z - z_0)^2]^2} \\ I_{43} = 2z_0\dfrac{(z - z_0)(x - x_0)}{[(x - x_0)^2 + (z - z_0)^2]^2} \\ I_{44} = 2zz_0\dfrac{(x - x_0)[3(z - z_0)^2 - (x - x_0)^2]}{[(x - x_0)^2 + (z - z_0)^2]^3} \end{cases} \tag{B.11}$$

Bibliography

Aki, K. & Richards, P., 1980. *Quantitative Seismology: Theory and Methods*, W. H. Freeman and Co., San Francisco.

Bonafede, M. & Rivalta, E., 1999. The tensile dislocation problem in a layered elastic medium, *Geophys. J. Int.*, **136**, 341–356.

Burchardt, S., 2008. New insights into the mechanics of sill emplacement provided by field observations of the Njardvik Sill, Northeast Iceland, *J. Volcanol. Geotherm. Res.*, **173**, 280–288.

Chouet, B., Dawson, P., Takao, O., Martini, M., Saccorotti, G., Giudicepietro, F., De Luca, G., Milana, G., & Scarpa, R., 2003. Source mechanisms of explosions at Stromboli Volcano, Italy, determined from moment-tensor inversions of very-long-period data, *J. Geophys. Res.*, **108**, (B1), 2019, doi:10.1029/2002JB001919.

Dahm, T., 2000a. On the shape and velocity of fluid-filled fractures in the earth, *Geophys. J. Int.*, **142**, 181–192.

Dahm, T., 2000b. Numerical simulations of the propagation path and the arrest of fluid-filled fractures in the earth, *Geophys. J. Int.*, **141**, 623–638.

Eissa, E. & Kazi, A., 1988. Relation between static and dinamic Yung's modulus, *Int. J. Rock Mech. Min. Sci.*, **25**, 479–482.

Froger, J.-L., Fukushima, Y., Briole, P., Staudacher, T., Souriot, T., & Villenueve, N., 2004. The deformation field of the August 2003 eruption at Piton de la

Fournaise, Reunion Island, mapped by ASAR interferometry, *Geophys. Res. Lett.*, **31**, L14601, doi:10.1029/2004GL020479.

Griffith, A., 1920. The phenomena of rupture and flow in solids, *Phil. Transaction of the Royal Soc.*, **A 221**, 163–198.

Gudmundsson, A., 2005. The effects of layering and local stresses in composite volcanoes on dyke emplacement and volcanic hazards, *C. R. Geoscience*, **3379**, 1216–1222.

Gudmundsson, A. & Brenner, S., 2005. On the conditions of sheet injections and eruptions in stratovolcanoes, *Bull Volcanol*, **67**, 768–782.

Heimpel, M. & Olson, P., 1994. Buoyancy-driven fracture and magma transport through the lithosphere: models and experiments, in *Magmatic Systems*, pp. 223–240, ed. Ryan, M., Academic Press, New York.

Ito, G. & Martel, S., 2002. Focusing of magma in the upper mantle through dike interaction, *J. Geophys. Res.*, **107 B10**.

Kavanagh, J., Menand, T., & Sparks, R., 2006. An experimental investigation of sill formation and propagation in layered elastic media, *Earth Planet. Sci. Lett.*, **245**, 799–813.

Kühn, D. & Dahm, T., 2004. Simulation of magma ascent by dykes in the mantle beneath mid-ocean ridges, *J. Geodynamics*, **38**, 147–159.

Kühn, D. & Dahm, T., 2008. Numerical modelling of dyke interaction and its influence on oceanic crust formation, *Tectonophys.*, **447**, 53–65.

Landau, L. & Lifschitz, E., 1967. *Théorie de l'élasticité*, Edition Mir, Moscow.

Lister, J., 1990. Buoyancy-driven fluid fracture: similarity solutions for the horizontal and vertical propagation of fluid-filled cracks, *J. Fluid. Mech.*, **217**, 213–239.

Lister, J. & Kerr, R., 1991. Fluid-mechanical models of crack propagation and their application to magma transport in dykes, *J. Geophys. Res.*, **94**, 10049–077.

Marinoni, L. & Gudmundsson, A., 2000. Dykes, faults and palaeostresses in the Teno and Anaga massifs of Tenerife (Canary Islands), *J. Volcanol. Geotherm. Res.*, **103**, 83–103.

Menand, T. & Tait, S., 2002. The propagation of a buoyant liquid-filled fissure from a source under constant pressure: An experimental approach, *J. Geophys. Res.*, **107, B11**, 2306,doi:10.1029/2001JB000589.

Meriaux, C. & Jaupart, C., 1998. Dike propagation through an elastic plate, *J. Geophys. Res.*, **103**, 18295–18314.

Pollard, D., 1976. On the form and stability of open hydraulic fractures in the Earth's crust, *Geophys. Res. Lett.*, **3**, 513–516.

Pollard, D. & Johnson, A., 1973. Mechanics of growth of some laccolithic intrusions in the Henry Mountains, Utah, II: Bending and failure of overburden layers and sill formation, *Tectonophys.*, **18**, 311–354.

Pollard, D. & Mueller, O., 1976. The effect of gradients in regional stress and magma pressure on the form of sheet intrusions in cross sections, *J. Geophys. Res.*, **81**, 975–984.

Rivalta, E. & Dahm, T., 2006. Acceleration of buoyancy driven fractures and magmatic dikes beneath the free surface, *Geophys. J. Int.*, **166**, 1424–1439.

Rivalta, E., Mangiavillano, W., & Bonafede, M., 2002. The edge dislocation problem in a layered elastic medium, *Geophys. J. Int.*, **149**, 508–523.

Rivalta, E., Böttinger, M., & Dahm, T., 2005. Gelatine experiments on dike ascent in layered media, *J. Volcanol. Geotherm. Res.*, **144**, 273–285.

Roper, S. & Lister, J., 2005. Buoyancy driven crack propagation from an overpressured source, *J. Fluid Mech.*, **536**, 79–98.

Roper, S. & Lister, J., 2007. Buoyancy driven crack propagation: the limit of large fracture toughness, *J. Fluid Mech.*, **580**, 359–380.

Rubin, A., 1995. Propagation of magma-filled cracks, *Ann. Rev. Earth Planet. Sci.*, **23**, 287–336.

Secor, D. & Pollard, D., 1975. On the stability of open hydraulic fractures in the Earth's crust, *Geophys. Res. Lett.*, **2**, 510–513.

Sigmundsson, F., Durand, P., & Massonet, D., 1999. Opening of an eruptive fissure and seaward displacement at Piton de la Fournaise volcano measured by RADARSAT satellite radar interferometry, *Geophys. Res. Lett.*, **26**, 533–536.

Smith, K. D., von Seggern, D., Blewitt, G., Preston, L., Anderson, J. G., Wernicke, B. P., & Davis, J. L., 2004. Evidence for Deep Magma Injection Beneath Lake Tahoe, Nevada-California, *Science*, **305**(5688), 1277–1280.

Spence, D., Sharp, P., & Turcotte, D., 1987. Buoyancy-driven crack propagation: a mechanism for magma migration, *J. Fluid Mech.*, **174**, 135–153.

Takada, A., 1990. Experimental study on propagation of liquid-filled crack in gelatin: shape and velocity in hydrostatic stress conditions, *J. Geophys. Res.*, **95**, 8471–8481.

Thybo, H. & Nielsen, C., 2009. Magma-compensated crustal thinning in continental rift zones, *Nature*, **457**, 873–876.

Turcotte, D. L. & Schubert, G., 1982. *Geodynamics*, Wiley, New York.

Watanabe, T., Masuyama, T., Nagaoka, K., & Tahara, T., 2002. Analog experiments on magma-filled cracks: Competition between external stresses and internal pressure, *Earth Planets Space*, **54**, 1247–1261.

Weertman, J., 1971. Theory of water-filled crevasses in glaciers applied to vertical magma transport beneath oceanic ridges, *J. Geophys. Res.*, **76**, 1171–1183.

Weertman, J., 1973. Oceanic ridges, magma filled cracks and mantle plumes, *Geofis. Int.*, **13**, 317–336.

White, R., Smith, L., Roberts, A., Christie, P., & Kusznir, N., 2008. Lower-crustal intrusion on the North Atlantic continental margin, *Nature*, **452**, 460–464.